MÉMOIRE D'HABILITATION À DIRIGER DES RECHERCHES DE l'UNIVERSITÉ PARIS DIDEROT
Sorbonne Paris Cité

Spécialité

Chimie

Présenté par

M. Cédric TARD

en vue d'obtenir l'habilitation à diriger des recherches de
l'Université Paris Diderot

Sujet du mémoire :

Transferts Couplés Électron Proton

Relais, Coupures et Catalyse

soutenue le 13 janvier 2015

devant le jury composé de :

Mme. Anne Bleuzen	PR UP11, Orsay	Examinateur
Mme. Deborah Jones	DR CNRS, Montpellier	Examinateur
M. Marc Robert	PR UP7, Paris	Rapporteur
Mme. Sylviane Sabo–Etienne	DR CNRS, Toulouse	Rapporteur
M. Jean–Michel Savéant	PR Émérite UP7, Paris	Président
M. Patrick R. Unwin	PR, University of Warwick	Rapporteur

Contents

Chapter 1

Curriculum Vitæ

Born in Chatenay–Malabry (France), the 18th of July 1979.

1.1 Career

Since Jan. 2013, Chargé de Recherche 1ère classe CNRS (section 13). Laboratoire d'Électrochimie Moléculaire, Université Paris–Diderot, France. Group of Profs. Marc Robert and Jean–Michel Savéant.

Jan. 2009 - Dec.2012, Chargé de Recherche 2nde classe CNRS (section 13). Laboratoire d'Électrochimie Moléculaire, Université Paris–Diderot, France. Group of Profs. Marc Robert and Jean–Michel Savéant.

Dec. 2007 - Dec. 2008, Post-doctoral position. Laboratoire d'Électrochimie Moléculaire, Université Paris–Diderot, France. Group of Profs Marc Robert and Jean–Michel Savéant.

Oct. 2007 - Dec. 2007, Post-doctoral position. School of Chemical Sciences, University of East Anglia, Norwich, UK. Group of Prof. Chris Pickett.

Oct. 2005 - Sept. 2007, Post-doctoral position. Laboratoire de Physique de la Matière Condensée, École Polytechnique, Palaiseau, France. Group of Prof. Jean–Pierre Boilot.

1.2 Education

Sept. 2005, PhD. Department of Biological Chemistry, John Innes Centre, University of East Anglia, Norwich, UK. Group of Prof. Chris Pickett.
Title of the thesis : Chemistry related to the [FeFe]–hydrogenases.
http://tel.archives-ouvertes.fr/tel-00011568/fr/

July 2002, D.E.A. des Systèmes Bioorganiques et Bioinorganiques. Université Paris–Sud, Orsay, France.

July 2001, Maîtrise de Chimie, Option Chimie Bioorganique et Bioinorganique. Université Paris–Descartes, Paris, France.

July 1999, D.U.T. de Chimie. Université Paris–Sud, Orsay, France.

1.3 Dissemination of research

1.3.1 Peered–review publications

*: *corresponding author*

Publications related to the PhD

P1 C. Tard, X. M. Liu, D. L. Hughes, and C. J. Pickett*
A novel $\{Fe^{I}–Fe^{II}–Fe^{II}–Fe^{I}\}$ iron thiolate carbonyl assembly which electrocatalyses hydrogen evolution.
Chem. Commun., **2005**, 133–135.
http://dx.doi.org/10.1039/b411559g

P2 C. Tard, X. M. Liu, S. K. Ibrahim, M. Bruschi, L. De Gioia, S. C. Davies, X. Yang, L. S. Wang, G. Sawers, and C. J. Pickett*
Synthesis of the H–cluster framework of iron–only hydrogenase.
Nature, **2005**, *433*, 610–613.
http://dx.doi.org/10.1038/nature03298

P3 X. M. Liu, S. K. Ibrahim, C. Tard, and C. J. Pickett*
Iron–only hydrogenase: Synthetic, structural and reactivity studies of model compounds.
Coord. Chem. Rev., **2005**, *249*, 1641–1652.
http://dx.doi.org/10.1016/j.ccr.2005.04.009

P4 D. E. Schwab, C. Tard, E. Brecht, J. W. Peters, C. J. Pickett, and R. K. Szilagyi*
On the electronic structure of the hydrogenase H–cluster.
Chem. Commun., **2006**, 3696–3698.
http://dx.doi.org/10.1039/b604994j

P5 S. K. Ibrahim, X. M. Liu, C. Tard, and C. J. Pickett*
Electropolymeric materials incorporating subsite structures related to iron–only hydrogenase: active ester functionalised poly(pyrroles) for covalent binding of {2Fe3S}–carbonyl/cyanide assemblies.

Chem. Commun., **2007**, 1535–1537.
http://dx.doi.org/10.1039/b617399c

P6 M. H. Cheah, C. Tard, S. J. Borg, X. M. Liu, S. K. Ibrahim, C. J. Pickett*, and S. P. Best*
Modeling [Fe–Fe] hydrogenase: evidence for bridging carbonyl and distal iron coordination vacancy in an electrocatalytically competent proton reduction by an iron thiolate assembly that operates through Fe(0)–Fe(II) levels.
J. Am. Chem. Soc., **2007**, *129*, 11085–11092.
http://dx.doi.org/10.1021/ja071331f

P7 F. F. Xu, C. Tard, X. F. Wang, S. K. Ibrahim, D. L. Hughes, W. Zhong, X. R. Zeng, Q. Y. Luo, X. M. Liu, and C. J. Pickett*
Controlling carbon monoxide binding at di–iron units related to the iron–only hydrogenase sub–site.
Chem. Commun., **2008**, 606–608.
http://dx.doi.org/10.1039/b712805c

P8 C. Tard and C. J. Pickett*
Structural and functional analogues of the active sites of the [Fe]–, [NiFe]–, and [FeFe]–hydrogenases.
Chem. Rev., **2009**, *109*, 2245–2274.
http://dx.doi.org/10.1021/cr800542q

Publications related to post–doctoral research

P9 L. L. Xuan, S. Brasselet, F. Treussart, J.–F. Roch,* F. Marquier, D. Chauvat, S. Perruchas, C. Tard, and T. Gacoin
Balanced homodyne detection of second–harmonic generation from isolated subwavelength emitters.
Appl. Phys. Lett., **2006**, *89*, 121118–121113.
http://dx.doi.org/10.1063/1.2356375

P10 L. L. Xuan, C. Y. Zhou, A. Slablab, D. Chauvat, C. Tard, S. Perruchas, T. Gacoin, P. Villeval, and J.–F. Roch*
Photostable second–harmonic generation from a single $KTiOPO_4$ nanocrystal for nonlinear microscopy.
Small, **2008**, *4*, 1332–1336.
http://dx.doi.org/10.1002/smll.200701093

P11 C. Tard, S. Perruchas,* S. Maron, X. F. Le Goff, F. Guillen, A. Garcia, J. Vigneron, A. Etcheberry, T. Gacoin, and J.–P. Boilot*
Thermochromic luminescence of sol–gel films based on copper iodide clusters.

Chem. Mater., **2008**, *20*, 7010–7016.
http://dx.doi.org/10.1021/cm801780g

P12 P. Wnuk,* L. Le Xuan, A. Slablab, C. Tard, S. Perruchas, T. Gacoin, J. F. Roch, D. Chauvat, and C. Radzewicz
Coherent nonlinear emission from a single KTP nanoparticle with broadband femtosecond pulses.
Opt. Express, **2009**, *17*, 4652–4658.
http://dx.doi.org/10.1364/oe.17.004652

P13 S. Perruchas,* C. Tard, X. F. Le Goff, A. Fargues, A. Garcia, S. Kahlal, J.–Y. Saillard, T. Gacoin, and J.–P. Boilot*
Thermochromic luminescence of copper iodide clusters: the case of phosphine ligands.
Inorg. Chem., **2011**, *50*, 10682–10692.
http://dx.doi.org/10.1021/ic201128a

Publications at the Laboratoire d'Électrochimie Moléculaire

P14 C. Costentin, M. Robert, J.–M. Savéant,* and C. Tard
Inserting a hydrogen–bond relay between proton exchanging sites in proton–coupled electron transfers.
Angew. Chem. Int. Ed., **2010**, *49*, 3803–3806.
http://dx.doi.org/10.1002/anie.200907192

P15 C. Costentin, V. Hajj, M. Robert, J.–M. Savéant,* and C. Tard
Effect of base pairing on the electrochemical oxidation of guanine.
J. Am. Chem. Soc., **2010**, *132*, 10142–10147.
http://dx.doi.org/10.1021/ja103421f

P16 C. Costentin, M. Robert, J.–M. Savéant,* and C. Tard
H–bond relays in proton–coupled electron transfers. Oxidation of a phenol concerted with proton transport to a distal base through an OH relay.
Phys. Chem. Chem. Phys., **2011**, *13*, 5353–5358.
http://dx.doi.org/10.1039/c0cp02275f

P17 C. Costentin, V. Hajj, M. Robert, J.–M. Savéant,* and C. Tard
Concerted heavy–atom bond cleavage and proton and electron transfers illustrated by proton–assisted reductive cleavage of an O–O bond.
Proc. Natl. Acad. Sci. U. S. A., **2011**, *108*, 8559–8564.
http://dx.doi.org/10.1073/pnas.1104952108

P18 J. Bonin, C. Costentin, M. Robert, J.–M. Savéant,* and C. Tard
Hydrogen–bond relays in concerted proton–electron transfers.

Acc. Chem. Res., **2012**, *45*, 372–381.
http://dx.doi.org/10.1021/ar200132f

P19 C. Costentin, M. Robert, J.–M. Savéant,* and C. Tard
Breaking bonds with electrons and protons. Models and examples.
Acc. Chem. Res., **2014**, *47*, 271–280.
http://dx.doi.org/10.1021/ar4001444

P20 C. Di Giovanni, W.–A. Wang, S. Nowak, J.–M. Grenèche, H. Lecoq, L. Mouton, M. Giraud,* and C. Tard*
Bioinspired iron sulfide nanoparticles for cheap and long–lived electrocatalytic molecular hydrogen evolution in neutral water.
ACS Catal., **2014**, *4*, 681–687.
http://dx.doi.org/10.1021/cs4011698

P21 J.–M. Savéant* and C. Tard*
Proton–coupled electron transfer in azobenzene–hydrazobenzene couples with pendant acid–base functions. Hydrogen–bonding and structural effects.
J. Am. Chem. Soc., **2014**, *136*, 8907–8910.
http://dx.doi.org/10.1021/ja504484a

1.3.2 Patent

Pat1 C. Tard and M. Giraud
Iron sulfide based catalyst for electrolytic water reduction into hydrogen gas.
Patent registration EP13305888, **2013**.

1.3.3 Peer reviewing

PR1 **2012**, *Inorg. Chim. Acta*, ed. Prof. Bernhard Lippert
Functionalised silica gel; iron complex; catechol degradation

PR2 **2013**, *Inorg. Chem.*, ed. Prof. James M. Mayer
Cobalt complex; electrochemical study; hydrogen evolution reaction

PR3 **2013**, *Inorg. Chem.*, ed. Prof. James M. Mayer
Palladium complex; electrochemical study; hydrogen evolution reaction

PR4 **2013**, *J. Am. Chem. Soc.*, ed. Prof. Joseph T. Hupp
Molybdenum complex; photocatalysis; electrochemical study; hydrogen evolution reaction

PR5 **2014**, *ACS Catal.*, ed. Prof. Susannah L. Scott
Molybdenum film; electrochemical study; hydrogen evolution reaction

PR6 **2014**, *Nat. Commun.*, ed. Dr. Luke Batchelor
Di–iron complex; electrochemical study; hydrogen evolution reaction; hydrogenase models

PR7 **2012** & **2014**, 2 ANR grant proposals

1.3.4 Bibliometry (2012 ISI Journal Citation Report, January 2015)

Journals	Impact factor	Publications	Citations
Chem. Rev.	45.66	P8	472
Nature	42.35	P2	313
Acc. Chem. Res.	24.35	P18/P19	15/3
Coord. Chem. Rev.	12.10	P3	181
J. Am. Chem. Soc.	11.44	P6/P15/P21	71/6/0
Angew. Chem. Int. Ed.	11.34	P14	22
Proc. Natl. Acad. Sci. U. S. A.	9.81	P17	12
Chem. Mater.	8.54	P11	33
ACS Catal.	7.58	P20	5
Small	7.51	P10	36
Chem. Commun.	6.72	P1/P4/P5/P7	40/28/26/44
Inorg. Chem.	4.79	P13	54
Phys. Chem. Chem. Phys.	4.20	P16	12
Opt. Express	3.53	P12	9
Appl. Phys. Lett.	3.52	P9	17
Total		21	1399
Average Citations per Article			66.62
Mean Edition Impact Factor	12.90		
h–index			14

1.3.5 Communications

Oral communications in conferences and symposiums

OC1 **June 2010**, 43rd Heyrovský Discussion, Castle Třešť, Czech Republic
Inserting a hydrogen bond relay between proton exchanging sites in proton–coupled electron transfers.
http://www.jh-inst.cas.cz/~hdisc/

OC2 **July 2011**, Journées d'Électrochimie 2011, Grenoble, France
Utilisation de relais dans les transferts couplés électron–proton longue distance.
http://www.je2011.fr/index.php

OC3 **March 2012**, Young Engineers + Scientists Symposium 2012, Berkeley, California, USA

Long range proton–coupled electron transfers: towards a biomimetic approach.
http://yess2012.org/

OC4 **Sept. 2012**, SNU – Paris–Diderot Chemistry Symposium 2012, Seoul, South Korea
Long range proton–coupled electron transfers in biomimetic systems.

OC5 **Nov. 2012**, Blaise Pascal International Chair, Vincent L. Pecoraro, Orsay, France
Long range proton–coupled electron transfers in biomimetic systems.

OC6 **June 2013**, 46th Heyrovský Discussion, Castle Třešť, Czech Republic
Transition metal chalcogenide nanoparticles for electrocatalytic hydrogen evolution.
http://www.jh-inst.cas.cz/~hdisc/2013

Laboratory seminars

LS1 **Sept. 2004**, School of Chemical Sciences, University of East Anglia, Norwich, UK
The active site of all–iron hydrogenase.

LS2 **Oct. 2005**, Laboratoire de Chimie et de Biochimie Pharmacologique et de Toxicologie, Université Paris Descartes, France
Modèles synthétiques du site actif de l'hydrogénase à fer.

LS3 **Nov. 2005**, Laboratoire de Chimie Inorganique, Université Paris–Sud, France
Modèles synthétiques du site actif de l'hydrogénase à fer.

LS4 **Feb. 2006**, Institut Lavoisier, Université de Versailles St–Quentin, France
Modèles synthétiques du site actif de l'hydrogénase à fer.

LS5 **Apr. 2007**, Département de Chimie Organique, Université de Genève, Switzerland
Synthetic models of the active site of the [FeFe]–hydrogenase.

Posters

Post1 **Apr. 2003**, Dalton Discussion 5, Leiden, The Netherlands
{2Fe3S}–assemblies related to the sub–site of all–iron hydrogenase.

Post2 **July 2003**, RSC Coordination Chemistry Discussion Group, Manchester, UK
{2Fe3S}–assemblies related to the sub–site of all–iron hydrogenase.

Post3 **Sept. 2003**, COST Meeting, Active Sites of Hydrogenases, Muelheim, Germany
Toward total synthesis of a free–standing H–cluster.

Post4 **July 2004**, Gordon Conference, Nitrogen Fixation, New London, NH, USA
Synthesis of {2Fe-3S}–cores related to the sub–site of [Fe]–hydrogenase: towards total synthesis of the H–cluster.

Post5 **Aug. 2004**, COST Meeting, 7th International Hydrogenases Conference, Reading, UK
Synthesis of {2Fe-3S}–cores related to the sub–site of [Fe]–hydrogenase: towards total synthesis of the H–cluster.

Post6 **Jan. 2007**, SFC Chimie de Coordination, Paris, France
Luminescent materials based on transition metal clusters.

Post7 **June 2007**, Summer School C'Nano IdF, Le Tremblay–sur–Mauldre, France
Contrôle optique du mouvement et de l'organisation de nanoparticules.

Post8 **Oct. 2011**, PCET 2011, Richelieu, France
Inserting a hydrogen bond relay between proton exchanging sites in proton–coupled electron transfers.

1.4 Research funding and scientific activities

1.4.1 Research funding

*: *Principal investigator*

RF1 **2010**, C. Tard*
Japan Society for the Promotion of Science
Fe/S nanoparticles for hydrogen evolution, rejected.

RF2 **2010**, M. Robert*, participation 20 %
Agence Nationale de la Recherche
Transfert et transport couplés d'électron et de proton dans des systèmes biomimétiques, accepted, 489 326 €.

RF3 **2011**, C. Tard*
ANR, Programme Jeunes Chercheuses Jeunes Chercheurs
Nanoparticules Fe/S pour la production réversible d'hydrogène, rejected.

RF4 **2011**, C. Tard and M. Robert*
Région Ile–de–France, DIM NanoSciences
Transfert couplé électron–proton sur longue distance relayé par des molécules d'eau, rejected.

RF5 **2012**, C. Tard*
ANR, Programme Jeunes Chercheuses Jeunes Chercheurs
Nanoparticules Fe/S pour la production réversible d'hydrogène, accepted, 179 263 €.

RF6 **2012**, C. Tard and M. Robert*
Région Ile–de–France, DIM Des atomes froids aux nanosciences

Water assisted long range proton–coupled electron transfer through biomimetic nano–channels, accepted, 42 800 €.

RF7 **2014**, C. Tard and M. Giraud*
LUCIA beam line at the SOLEIL synchrotron
Probing the role of sulfur in hydrogen–producing iron sulfide nanocatalysts, accepted.

1.4.2 Students

– Co–supervision of 2 post–doctoral fellows, Matteo Duca (2012–2013, funding RF6, publication P21) and Carlo Di Giovanni (2013–2015, funding RF5, publication P20). Matteo Duca has worked on the electrochemical studies of long–ranged proton–coupled electron transfer in synthetic bio–channels (see section 3.2). Carlo Di Giovanni is currently involved in the project of electrocatalytic reduction of protons using iron–sulfide nanoparticles (see section 2.3.5).
– Co–supervision of 1 PhD student, Viviane Hajj (2008–2011, publications P15 and P17). During her PhD, Viviane Hajj has developed the synthesis of guanidine and cycloperoxide derivatives in order to study bio–inspired proton–coupled electron transfer reaction by electrochemical techniques (see section 2.3.4). Supervision of 2 PhD students, Alison Tebo and Jefferson Plegaria, from the group of Vincent L. Pecoraro at the University of Michigan. During their visits in our laboratory (2 × 2 months each), we investigated the electrochemical behaviour of bioinorganic peptides models of iron and copper proteins.
– Supervision or co–supervision of 10 undergraduate students from École Normale Supérieure – Paris (2), INP Phelma (Grenoble), Université Paris–Diderot (2), Université Paris–Descartes (2), INSA Strasbourg, Lycée Notre–Dame (Verneuil, BTS) and King's College (Cambridge, UK).

1.4.3 Teaching

2003–2005 During my PhD thesis I was involved in the laboratory practical course for first year students at the School of Chemical Sciences and Pharmacy of the University of East Anglia (Norwich, U. K.). The experiments were related to bonding structure and periodicity, chemistry of carbon compounds, analytical chemistry and spectroscopy.

2007 During my post-doctoral contract at the École Polytechnique I was involved in the practical courses in organic chemistry for the competitive examination admission.

1.4.4 Scientific collaborations

SC1 **2005**, University of Melbourne, Department of Chemistry
Dr. Stephen P. Best, spectroelectrochemistry of [FeFe]–Hydrogenase models (publication P6).
2 months visit in May–June 2005.

SC2 **2005–2007**, ENS Cachan, Laboratoire de Photonique Quantique et Moléculaire, UMR 8537
Prof. Jean–François Roch, photophysic studies of $KTiOPO_4$ nanoparticles (publications P9, P10 and P12).

SC3 **2006–2007**, CEA Saclay, SPCSI, Laboratoire d'Électronique et Nanophotonique Organique
Dr. Céline Fiorini, functionalized nanoparticles STM studies.

SC4 **since 2010**, Université Paris–Diderot, Laboratoire ITODYS, UMR 7086
Dr. Marion Giraud, synthesis and characterization of Fe/S nanoparticles (publication P20 and patent Pat1).

SC5 **since 2011**, CEA Saclay, DMS, Institut Rayonnement Matière de Saclay
Dr. Thibault Cantat, organic molecules for the electrocatalysis of carbon dioxide reduction.

SC6 **since 2012**, University of Michigan, Department of Chemistry
Prof. Vincent L. Pecoraro, water channel and proton–coupled electron transfer (publication P21).
4 months visit in Feb.–June 2012.

1.4.5 Conferences and seminars organization

Since 2010, I am co–organizing the Lavoisier Lectures with 3 colleagues from the chemistry department. Once a year and during one week the chemistry department hosts a prestigious scientist. We already welcomed Profs. George M. Whitesides (2011, Harvard), John H. Seinfeld (Caltech, 2011), Naomi J. Halas (2012, Rice University) and Patrick R. Unwin (2013, Warwick University).

In 2011, our research group organized an international conference in the Loire Valley on Proton–Coupled Electron Transfer reactions, with the participation of Profs. Dennis Evans, Marc Fontecave, Leif Hammarström, Sharon Hammes–Schiffer, James M. Mayer, Thomas J. Meyer, Daniel Nocera and JoAnne Stubbe. During the organization process, I was in charge of the website, the registration and the communication with the attendees.

1.4.6 Administrative duties

I have been elected at the *Laboratoire d'Électrochimie Moléculaire* laboratory council (2013–2017) and at the chemistry department scientific council (2014–2018).

Chapter 2

Scientific assessment

2.1 Doctoral thesis assessment

My PhD thesis started in October 2002 at the Biological Chemistry Department of the John Innes Centre (Norwich, UK) under the supervision of Prof. Chris Pickett. Following the unraveling of the crystal structure of the [Fe–Fe]–hydrogenase enzyme, able to reversibly converts protons into molecular hydrogen,[1, 2] the group of Prof. Pickett started in 1999 to study the synthesis of organometallic models of the active site of this enzyme, the so–called 'H–cluster'.[3] This enzymatic active site is rather peculiar, and is composed of an $[Fe_4S_4]$–cluster linked by a cysteinyl residue to a $[Fe_2S_2]$–sub–site (Figure 2.1).[4] The binuclear metal centre, thought to be the catalytic part, is bridged by a dithiolate ligand, now depicted as a di(thiomethyl)amine. Biologically unusual carbonyl and cyanide ligands also coordinate the two irons. The synthesis of sub–site structural analogues has been extensively studies after the publication of the X–ray crystal structure of the enzyme, and is based on the reaction between a dithiol ligand and an iron carbonyl complex. Notably the complex $Fe_2(CO)_6(SEt)_2$ has been synthesized in 1929,[5] and since then hundreds of di–iron complexes have also been prepared.[6, 7]

The major challenge of modelling the active site of the [Fe–Fe]–hydrogenase is to find a molecular complex able to catalyse reversibly the reduction of protons into molecular hydrogen. One can envisage that such catalysts would give a chance to molecular hydrogen to become an alternative to fossil fuels, as exemplified by the number of models prepared so far. Indeed, production of molecular hydrogen currently uses either hydrocarbon sources (by reforming or pyrolysis) or noble metal catalysts for the electrocatalytical reduction of water, these two option being unrealistic on the mid– and long–term regarding sustainability and cost issues.[8] Molecular complexes could be envisaged as potential candidates for electrocatalysis of hydrogen evolution, but only if ease of preparation, stability, efficiency and cost of these molecules provide a net advantage over the existing materials. Concerning small–molecule activation in general, this is clearly not the case yet, and currently much of the attention is focused on the mechanistic understanding of the catalysis and the unravelling of biological machinery processes.

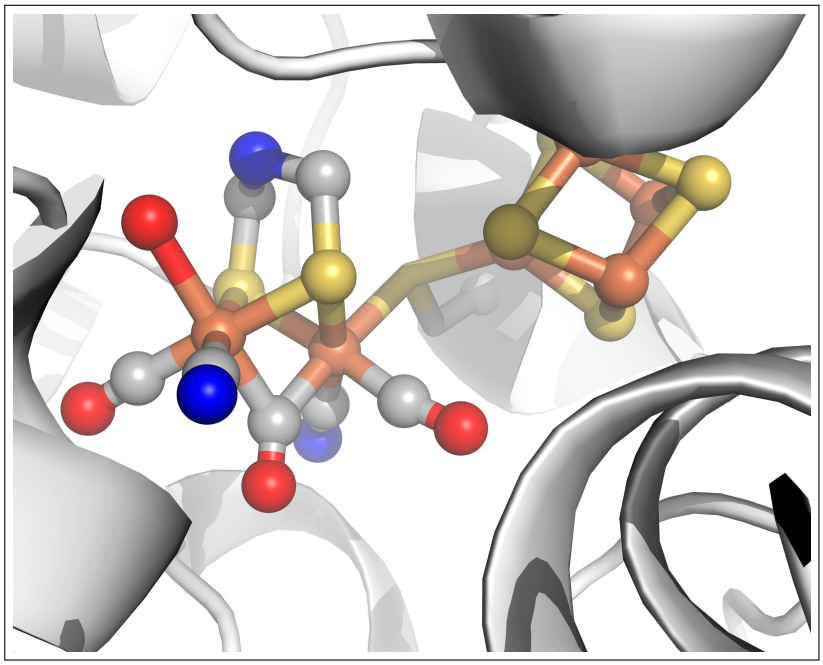

Figure 2.1: X–ray structure of the active site of the [FeFe]–hydrogenase (PDB ID, 3C8Y). Orange spheres: Fe; blue spheres: N; red spheres: O; yellow sphere: S; grey spheres: C.

The work of my PhD thesis was focused on the synthesis, and reactivity and electrochemical studies of chemical models of the active site of the [Fe–Fe]–hydrogenase enzyme. Without going into the details of the different molecules prepared during these three years, two model complexes have attracted much of our attention regarding their biological structural and activity relevance.

2.1.1 H–cluster framework

The recent unravelling of the [FeFe]–hydrogenase structure led us to investigate the synthesis of a free–standing structural model of the active site. The hardship of this project was the preparation of an asymmetrical $[Fe_4S_4]$–cluster where a $[Fe_2S_2]$–unit could be attached. Whereas the chemistry of FeS complexes related to iron–sulphur proteins has attracted much attention over the past 40 years or so, only very few examples of asymmetric cubane $[Fe_4S_4]$–clusters have been explored. We thus decided to follow the synthesis described by Holm and co–workers,[9] who designed a ligand able to coordinate three out of the four irons, leaving the fourth iron able to coordinate an extra ligand. Following this strategy, we designed and synthesised the first model of the entire H–cluster of the [Fe–Fe]–hydrogenase enzyme through linking of a di–iron sub–site to a $[Fe_4S_4]$–cluster (Figure 2.2).[10] The electron transfer process of this system has been studied by electrochemical and spectroelectrochemical methods, and electronic and mechanistic aspects of the interplay between the sub–site and iron–sulphur cluster explored.

The voltammograms obtained have been simulated and we proposed a mechanism that

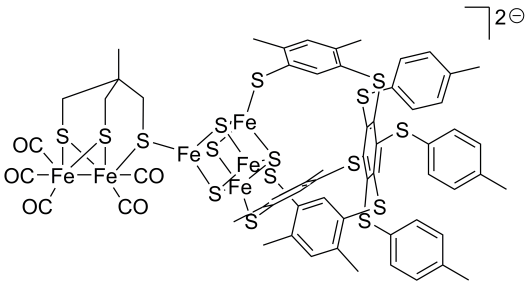

Figure 2.2: Synthetic H–cluster model.

involves an intramolecular electron transfer between the reduced $[Fe_4S_4]$–cluster and the $[Fe_2S_2]$–sub–site in concert with reversible opening of the μ–SCH_2 bridge. This study outlined the fundamental role of the functionality brought by the thioether ligand, whereas all the other synthetic systems studied so far are focused on the modification of ligands around the di–iron centre, the functionalisation the dithiolate bridging ligand or the modification of second coordination sphere.

X–ray absorption spectroscopic measurements and density functional theory (DFT) calculations also suggested that the synthetic hydrogenase H–cluster is best described as an electronically inseparable 6Fe–cluster due to extensive delocalization of frontier molecular orbitals of the iron centres, sulphide and the non–innocent dithiolate ligands.[10, 11]

Furthermore, this assembly electrocatalyses dihydrogen evolution in organic solvents at a relative low overpotential potential for such di–iron model, indicating that the model is relevant in terms of structure and activity. Nevertheless, it has to be stressed that the synthesis of this type of complex is long and difficult, rendering its potential application unrealistic for industrial purposes.

2.1.2 $\{Fe^{I}$–Fe^{II}–Fe^{II}–$Fe^{I}\}$ iron thiolate carbonyl assembly

A mixed–valent tetra–iron thiolate carbonyl assembly has been synthesized in which two dithiolate tetracarbonyl di–iron centres with a butterfly configuration of the $[Fe_2S_3]$–cores are fused by two bridging thiolates which form a central planar $[Fe_2S_2]$–unit.[12] This was the first example of a chain of four metal–metal bonded iron atoms supported by a bridging sulphur framework.

Just as for the di–iron–sulphur complexes family, this assembly electrocatalyses hydrogen evolution. Electrocatalytic proton reduction proceeds slowly at mild potentials by a one–electron reduction of the complex, a rate–limiting protonation followed by a further one–electron reduction, and finally dihydrogen elimination. Our study showed that a dramatic increase in the rate of electrocatalysis occurs if two–electron reduction precedes the protonation (Figure 2.3).

Spectroelectrochemical measurements coupled to DFT calculations showed that the striking increased rate of electrocatalysis obtained from $[Fe_4S_6]$–core over all previously

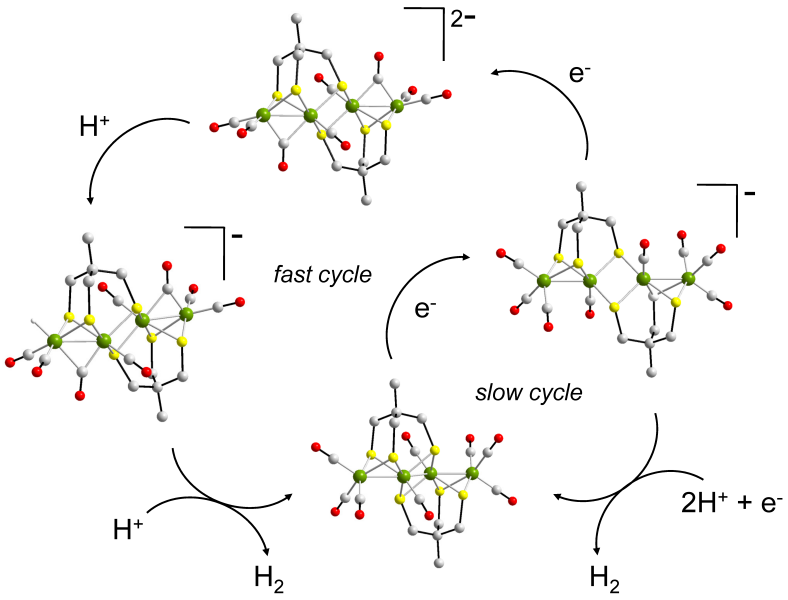

Figure 2.3: DFT calculated structures and mechanism of proton reduction by the mixed–valent $[Fe_4S_6]$–complex.

identified model compounds appears to be related to the features uniquely common between it and the H–cluster, namely, that turnover involves the same formal redox states of the di–iron unit ($Fe^{I}Fe^{II}$ and $Fe^{0}Fe^{II}$), the presence of an open site on the outer Fe atom of the $Fe^{0}Fe^{II}$ unit, and the thiolate–bridge to a second one–electron redox unit.[13] While lacking the CN^{-} ligands and including two, instead of one, bridging thiolate sulphur atoms to a second redox centre, this assembly provided an important insight into the reactivity of the H–cluster.

2.2 Post–doctoral assessment

After my PhD, I joined the group of Prof. Jean–Pierre Boilot at the Laboratoire de Physique de la Matière Condensée of the École Polytechnique (Palaiseau, France). The group is well recognized for its contributions in solid state chemistry, and notably in the study of optical properties of functional hybrid organic–inorganic materials. I have been involved in three projects related to luminescent properties, second–harmonic generation and optical control of nanoparticles motion, mainly performing luminescence studies and synthesis of complexes and nanoparticles.

2.2.1 Thermochromic luminescence of copper iodide clusters

The aim of this project was to study luminescent molecular inorganic clusters within a solid matrix, these clusters having photostability properties of inorganic nanoparticles together with monodispersity of organic molecules. Indeed, it is well known that the poor photostability of organic molecules is a major drawback in terms of applications, and the issue of controlling the size and the surface of nano–objects is also problematic. Incorporation of these molecular inorganic clusters within a sol–gel matrix would thus provide a way to prepare luminescent, homogeneous and photostable materials at room temperature and ambient pressure.

Sol–gel process

The sol–gel process is a soft method of producing solid–state materials by hydrolysis and condensation of molecular precursors. The precursor can be an alcoholate or a metallic salt. The 'sol' is prepared at ambient temperature by hydrolysis of the precursor, and the 'gel' is formed when the solvent molecules are trapped within the solid matrix forming a biphasic system. The drying step is crucial and has to be controlled in order to obtain a xerogel (slow drying) or an aerogel (supercritical drying).

The system chosen was the cubane $[Cu_4I_4]$–cluster (Figure 2.4, left), known for its thermochromic luminescent properties,[14, 15] and by combining these two properties, luminescence and thermochromism, we aimed at developing new materials with unusual properties. The tetracopper(I) clusters $[Cu_4X_4L_4]$ (X = Cl, Br, I; L = pyridine or amine–based derivatives) are known to be highly luminescent at room temperature. These compounds are easily synthesized from cheap precursors in solution at room temperature, and can be obtained with different types of ligands (L) allowing their functionalization. Furthermore, these copper clusters display emission spectra that are sensitive to their environment, the temperature, and the rigidity of the medium. For example, the thermochromic luminescence originates from two emission bands whose relative intensities vary in temperature. At room temperature, the luminescence is dominated by a low energy band (LE) which has been attributed to a combination of a halide–to–metal charge transfer (XMCT) and copper–centred d $\rightarrow$ s, p transitions. This emission is called cluster centred (CC) as it involves a $[Cu_4I_4]$–cluster centred triplet excited state, which is essentially independent of the nature of the ligand. At low temperature, this band is extremely weak, and the emission is dominated by a high energy band (HE) which has been attributed to a triplet halide–to–ligand charge transfer (XLCT) excited state (Figure 2.4, right). As the π^* orbitals of the ligands are involved in this XLCT band, the emission at low temperature is only observed for clusters incorporating π–unsaturated ligands. All these properties make these copper clusters particularly attractive for their incorporation in organic or inorganic polymeric matrices, to synthesize materials with original optical applications.

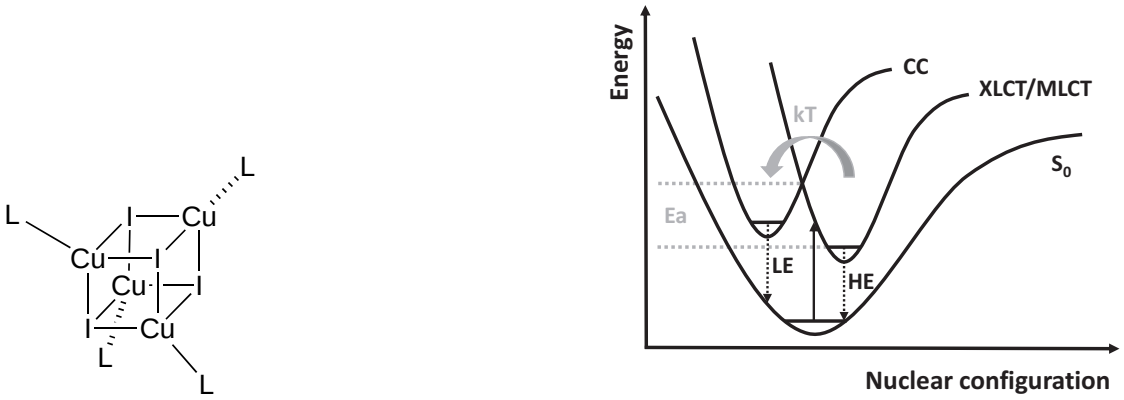

Figure 2.4: Left: General representation of $[Cu_4I_4L_4]$–clusters (X = Cl, Br, I; L = organic ligand). Right: Simplified energy level diagram of the copper iodide clusters studied.

Very few examples of phosphine derivative $[Cu_4I_4]$–clusters have been reported in the literature. Compared to pyridine or amine–based derivatives, they are more stable, and thus particularly interesting for the synthesis of original emissive materials. Thus, we performed photophysical studies on phosphine–based clusters, and we investigated the correlation between experimental (structural and optical) and theoretical data and compared the results with previous works on pyridine–based clusters to provide new insights into this complicated photophysical system.[16] Under UV excitation (330 nm), two intense emissions were observed for the clusters studied with a bright green–yellow luminescence at room temperature which becomes blue at low temperature (8 K) (Figure 2.5). The DFT calculations were in agreement with the following band assignment: the LE band originates from a $[Cu_4I_4]$–cluster centred excited state whereas the HE one involves a mixed charge–transfer (MLCT/XLCT) excited state, which differs from $[Cu_4I_4py_4]$–cluster type. As the π^* orbitals of the ligands are involved in this XLCT band, the emission at low temperature is only observed for clusters incorporating π–unsaturated ligands. The thermochromic luminescence exhibited by these clusters derives from the thermal equilibrium between two separate excited states (MLCT/XLCT and CC). In contrast with the pyridine derivatives, the same excitation states and low activation energies for these clusters reflect high coupling of the two emissive states. The effect of the Cu–Cu interactions on the emission properties of these clusters is not so obvious. Particularly, our results disagree with previous studies suggesting that only compounds with Cu–Cu distances shorter than 2.8–2.9 Å exhibit emissive CC states.[17] On the contrary, for the LE band emission the Cu–Cu distances do not seem to be an essential parameter.

This photophysical study led us to investigate the incorporation of copper iodide clusters in sol–gel silica matrices.[18] These photoactive entities were functionalized with phosphine ligands bearing alcoxysilane groups able to copolymerize with the methyltriethoxysilane (MTEOS) sol–gel precursor. By this way, the optical properties of these clusters were successfully preserved in the matrix, as evidenced by solid–state NMR and X–ray

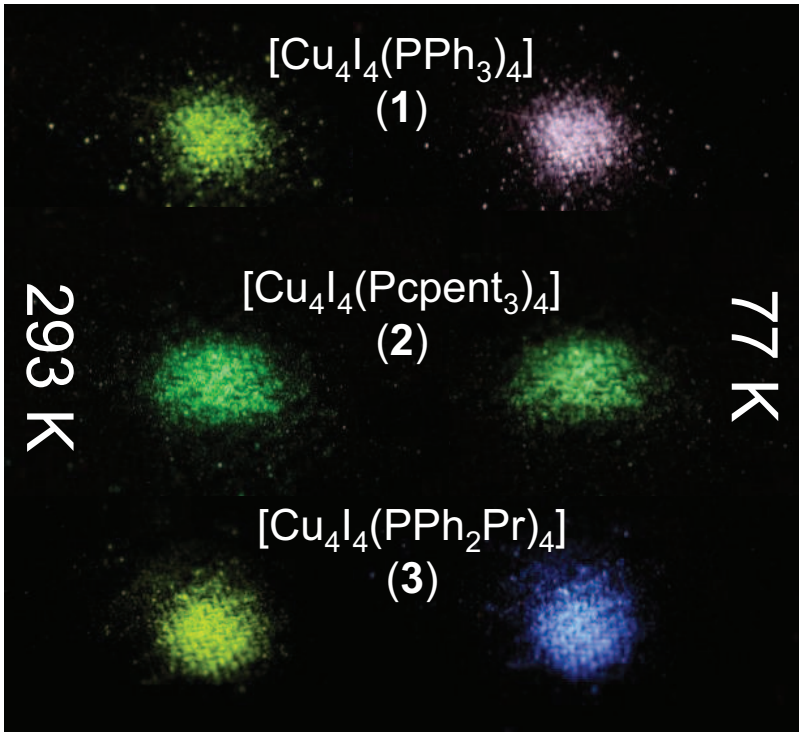

Figure 2.5: Phosphine $[Cu_4I_4L_4]$–cluster powders under UV irradiation at 312 nm at room temperature (left) and in liquid nitrogen (right).[16]

photoelectron spectroscopy (XPS) analyses showing that a great majority of the clusters remained intact within the film. A few oxidized phosphine ligands were detected in the film by NMR, whose presence was inherent to the acidic sol–gel conditions. The luminescence properties of the sol–gel films displayed striking change in the colour emission in temperature from 292 K to 8 K, which was consistent with the previous photophysical analysis performed on the free-standing copper iodide phosphine cluster (Figure 2.6). These films were the first exhibiting thermochromic luminescence, and one can envisage to be useful for temperature sensing applications.

2.2.2 Second–harmonic generation from $KTiOPO_4$ nanocrystals

This project was realized in collaboration with the Laboratoire de Photonique Quantique et Moléculaire of the ENS Cachan for the optical characterization part (**SC2**).

Nonlinear second–harmonic generation (SHG) microscopy has become a commonly used technique for investigating interfacial phenomena and imaging biological samples. For organic nanocrystals, resonant optical interaction leads to an enhancement of the nonlinear response but also to a parasitic effect that is detrimental for practical applications, namely photobleaching due to two–photon residual absorption. This issue could be circumvent using SHG microscopy, but it usually leads to weak photon flux, and extremely faint signals are therefore expected from nano–objects with second–harmonic nonlinear re-

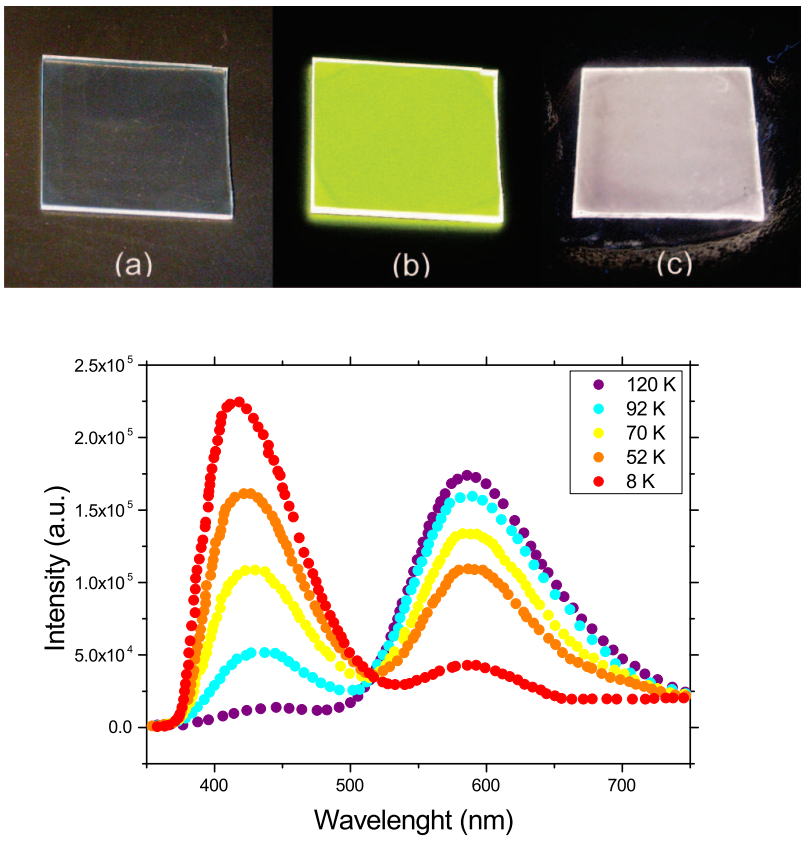

Figure 2.6: Top: $[Cu_4I_4L_4]$–clusters film deposited on glass substrates (a) under ambient light and (b) under UV irradiation at 312 nm at room temperature and (c) under UV irradiation at 312 nm in liquid nitrogen. Bottom: Temperature dependence emission spectra for $[Cu_4I_4L_4]$–clusters film on a glass substrate from 120 K to 8 K with λ_{ex} = 300 nm.

sponse. Direct detection with avalanche photodiode in photon counting regime is a practical solution and coherent detection of the SHG signal can be performed using a balanced homodyne detection scheme allowing a sensitivity to extremely low photon flux rates. We therefore decided to consider a well–known SHG–active bulk material and investigate its properties in nanoparticle form.

Second–harmonic generation

The second–harmonic generation is a non-linear optical phenomenon. Photons interacting with non-linear materials are 'associated' to generate new photons with twice the energy — i.e. a doubled frequency or half the wavelenght — of the initial photons. In microscopy, the contrast will be obtained by a variation of the SHG capability of a material (or a biological tissue) from the incident light.

Potassium titanyl phosphate $KTiOPO_4$ (KTP) is a widely used nonlinear crystal. The KTP nanoparticles were extracted from the raw powder that remains in the trough at the end of the flux–growth process, which leads to the synthesis of large–sized KTP single crystals. We then applied a size–selection procedure by selective centrifugation to obtain a colloidal solution of non–aggregated particles.[19] Under femtosecond excitation and in ambient conditions, a single nano–KTP particle with a size of around 60 nm, independently determined with atomic force microscopy (AFM), generates a perfectly stable blinking–free second–harmonic signal that can be easily detected in the photon–counting regime.[20] Furthermore, we showed that the use of broadband ultrashort laser pulses improved the second–harmonic emission from a single nanoparticle of size about 120 nm (Figure 2.7).[21] It resulted in a contrast enhancement of the SHG image obtained by raster scanning the sample.* In this process, smaller nanoparticles were revealed for a given background. This work is currently extended to the optical nonlinear response of other nanoparticles and specific single nanostructures, and to other nonlinear coherent processes.

2.2.3 Optical control of nanoparticles organization and movement

This project was developed in collaboration with the Laboratoire d'Électronique et Nanophotonique Organique at the CEA Saclay (**SC3**).

Molecular motors are gaining increased interest for their integration within nanoscaled devices with the perspective of low cost, low power consumption and new functionalities with improved performances. The ability to direct the spatial distribution of nanoparticles with a controlled defined arrangement of variable sized nanoparticles leads to the promise of the future design and realization of complex and functional systems. The approach proposed in this project was based on a non–contact optical manipulation of a molecular photoactive entity attached to a nanoparticle.

*The *raster scanning* gives a dot matrix data structure with rectangular pixels

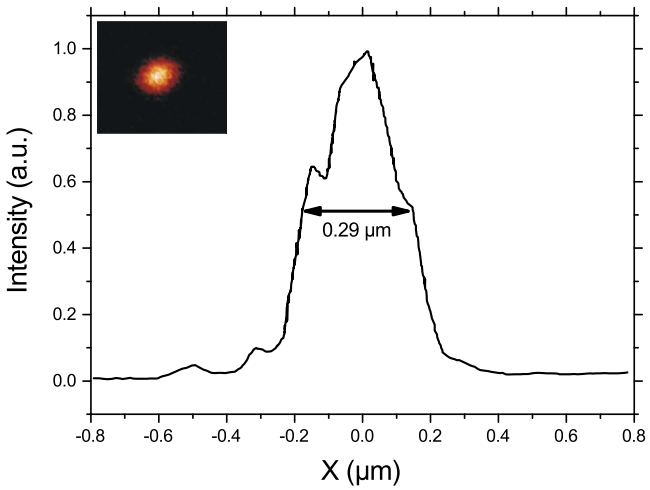

Figure 2.7: KTP nanoparticle associated second harmonic emission with a diffraction–limited spot. Inset: AFM raster scan of a 120 nm KTP nanoparticle.

Azobenzene molecules are considered as unique photomechanic systems giving rise to light–induced switching properties *cis* ↔ *trans* at the single molecular level. Another key aspect strengthening the interest of azobenzene molecules is their ability to produce average photo–induced mass–transport effects when embedded into an organic host. We started the investigation and optimization of photoactive molecules based on azobenzene–units in contact with gold nanoparticles with the idea in mind that reversible structural changes, inherent to azo–photoisomerisation upon resonant illumination, enables the conversion of photon energy into mechanical energy. Two strategies have been tested: a) the 'moving walkway', where nanoparticles would move on a surface modified by azobenzene molecules upon irradiation; b) the 'moving nanoparticles', where direct functionalization of nanoparticles with azobenzene units would permit the light–induced movement of the nanoparticle (Figure 2.8). The synthesis of several molecules and stable nanoparticles has been performed, and some preliminary tests have been conducted using local probe microscopy techniques with an aperture near–field optical microscope coupled to an atomic force microscope and a scanning tunnelling microscope. No relevant results from these experiments have come out so far.

2.3 Research at the Laboratoire d'Électrochimie Moléculaire

2.3.1 Context

The Laboratoire d'Électrochimie Moléculaire, led by Dr. Benoit Limoges, is part of the chemistry department at the Université Paris–Diderot, and is composed of 17 researchers.

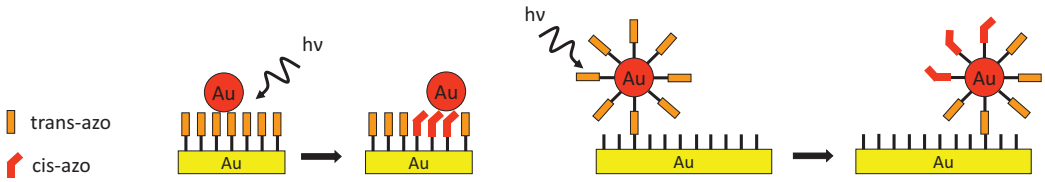

Figure 2.8: Schematic view of the photo–induced movement of gold nanoparticles. Left: the 'moving walkway'; right: the 'moving nanoparticles'.

The research activities are focused on both fundamental and applied aspects of molecular and biomolecular electrochemistry.

I have been hired in 2007 as a post–doctoral fellow and in 2008 as a CNRS researcher in the team *Electron transfer and molecular changes. Fundamental aspects, reactivity of organic and biomimetic molecules* led by Prof. Marc Robert. Our group is composed of 6 researchers, and is interested in the general understanding of electron transfer chemistry coupled to molecular changes, such as in proton–coupled electron transfer (PCET) or bond cleavage / formation. Mechanistic studies are supported by electrochemical and photochemical studies, together with theoretical descriptions of the mechanistic models. Following these fundamental studies, the group is now moving towards the investigation of detailed mechanistic studies of catalytic activation of small molecules.

The team work is a fundamental aspect of the working process in our group. In the projects presented in this manuscript, the different tasks are conducted in agreement with the different partners all along the research process. Following my PhD and post–doctoral experience concerning the synthesis of elaborate molecular and nanometric systems, I brought to the team the possibility to investigate new strategies to tackle some of the synthetic challenges encountered. Thus, I am involved in the design, the synthesis and the electrochemical studies of the system of interest. The interpretations and theoretical descriptions are devoted to my colleagues, Profs. Cyrille Costentin, Marc Robert and Jean–Michel Savéant.

2.3.2 Proton–coupled electron transfer

The group has a long and solid experience in the investigation of electronic transfer mechanisms that started in the 1970s. Over the past decade, the group has made important contributions to PCET reactions, in term of experimental studies as well as theoretical investigations.[22, 23, 24] This topic is directly connected to the fossil fuel energy crisis that the world is now facing, and of which the consequences are going to be more and more problematic. PCET reactions are found to be ubiquitous in nature, and are involved in numerous natural and artificial processes. The understanding of such transfer mechanism is crucial to get a more comprehensive glimpse of complex biological processes, as well as a better view of the potential implication of PCET reactions in the catalytic activation of small molecules (e.g. H_2O, O_2 or CO_2). This would conceivably end up in the depic-

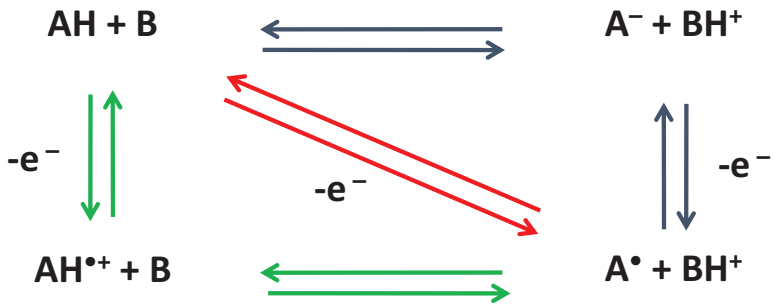

Figure 2.9: Square–scheme for PCET reactions.

tion of crucial parameters to obtain economically viable molecules / materials towards the development of cheap, sustainable and robust catalysts.

Water oxidation in photosystem II is one of the most studies example for the coupling between PCET and catalysis. This enzyme can be found in plants and algae, and is involved in the photosynthesis process as the catalyst for the oxidation of water into molecular oxygen. The abundant literature on this topic is coming from the fact that in this enzyme the solar energy is converted into chemical energy by the formation of an O–O bond at room temperature, atmospheric pressure and without the use of noble metals. To design catalysts able to reproduce such process, the understanding of the intimate mechanism of PCET reactions within the enzyme and how it may affect the catalysis at the active site is of primary importance. In the following discussion, we will investigate PCET reactions in the view of their biological relevance, and notably the correlation between the electron transfer and the long–range transfer of protons as well as PCET reaction and bond breaking. But first, it is necessary to replace this discussion in the context of more fundamental aspects with a brief and simplified description of the theoretical models considered.

Theoretical model of PCET and CPET reaction

The acronym PCET is the generic term that describes reactions where proton and electron are transferred, either stepwise or in the same step. Unlike simple electron transfer or proton transfer reactions, PCET reactions are more complicated as the coupling between the two particles directly influences the process, thermodynamically and kinetically. The square–scheme in figure 2.9 is typically used to represent this reaction, with either proton transfer followed by electron transfer (PT–ET, green), or electron transfer followed by proton transfer (ET–PT, blue). The concerted proton–electron transfer (CPET) pathway can also be involved (red), and has the advantage to circumvent high energy intermediates.

Until recently, only the sequential pathways were considered. When the rate–determining step is the electron transfer, with proton transfer reaction at equilibrium, the Marcus–Hush model can be applied using the Born–Oppenheimer approximation. The movement of electrons and nucleus is decoupled, because of the mass difference between the particles,

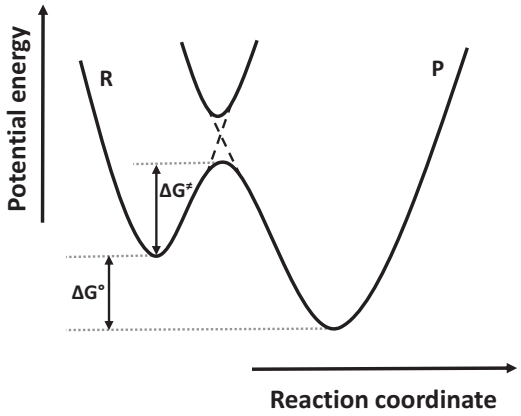

Figure 2.10: Potential energy profiles of reactants (R) and products (P) in the case of an outer–sphere electron transfer according to the Marcus–Hush model).

and the electron transfer dynamic is solely governed by intramolecular reorganisation and solvent reorganisation. We can represent reactant and product energies using parabolas in function of the reaction coordinate (Figure 2.10). The difference between the two parabola minima is the driving force $-\Delta G^\circ$, and in electrochemistry, for an oxidation, it corresponds to the difference between the potential applied at the electrode E and the standard potential of the redox couple E° such as:

$$-\Delta G^\circ = F(E - E^\circ) \tag{2.1}$$

A nuclear pre–organisation is necessary to allow the electron transfer, which happens at the intercept of the two parabolas, where the energies of the reactant and the product are equals, with an activation energy given by:

$$\Delta G^{\neq} = \frac{\lambda}{4}\left(1 + \frac{\Delta G^\circ}{\lambda}\right)^2 \tag{2.2}$$

where

$$\lambda = \lambda_i + \lambda_0 \tag{2.3}$$

with λ_i as the internal reorganisation (i.e. angle and bond deformation) and λ_0 as the solvent reorganisation (i.e. for the most part polarisation).

In the case of the transition state theory, the kinetic rate constant k of the electron transfer has the following expression:

$$k = Z \exp\left(-\frac{\Delta G^{\neq}}{RT}\right) \tag{2.4}$$

where the pre–exponential factor Z is given by:

$$Z = Z^{el} \times \chi \tag{2.5}$$

where Z^{el} is the collision frequency defined as:

$$Z^{el} = \sqrt{\frac{RT}{2\pi M}} \tag{2.6}$$

and χ the transmission coefficient:

$$\chi = \frac{2p}{1+p} \tag{2.7}$$

where M is the molar mass of the reactant and p is the probability of electron transfer.

Several experimental features observed in PCET reactions do not fit with stepwise mechanisms. Therefore the Marcus–Hush model is not sufficient any more to described the electron transfer. The theoretical framework for homogeneous CPET has been mainly developed over the past 20 years.[25] Nevertheless, this theory was not suitable for electrochemical studies, and a model developed in the laboratory intends to describe the concerted mechanism, in which the proton *and* the electron are transferred in the same elementary step.[23]

The main feature of CPET theories is the double Born–Oppenheimer approximation, which considers the electron as a light particle compared to the proton, and treats the proton as a light particle compared to the rest of the system, so the dynamic of the electron and the proton is controlled by heavy atoms and solvent reorganisation. As in Marcus–Hush theory, the CPET mechanism can be described by two diabatic electronic states, and the electron and the proton transfer occurs at the intercept of the two parabola. At this stage a second Born–Oppenheimer approximation can be made, due to the difference in mass between the proton and the electron. Thus, the two electronic states can be described as a function of the proton coordinate, and the electron transfer occurs at the intercept of the two states, the proton being transferred by tunnel effect in his fundamental state (Figure 2.11).

The activation energy and the rate constant have the same form as in equations (2.2) and (2.4) for an outer sphere electron transfer, but with different reorganisation energy and pre–exponential factor expressions. As for a CPET reaction, the reorganisation energy λ is given by:

$$\lambda = \lambda_i + \lambda_0^{ET} + \lambda_0^{PT} \tag{2.8}$$

where λ_i is the internal reorganisation energy, λ_0^{ET} is the reorganisation energy for the electron transfer and λ_0^{PT} is the reorganisation energy for the proton transfer. The pre–exponential factor includes the probability of the electron transfer *and* the proton transfer.

As compared to the sequential pathway, in the case of a concerted mechanism we expect a smaller rate constant for the electron transfer because of the increase in the reorganisation energy of the system. Furthermore, if the experiment is conducted in a deuterated media, a kinetic isotope effect (KIE) is expected because the proton transfer occurs in the rate–determining step. Experimentally, the presence of a KIE would therefore be a strong indicator whether the mechanism is sequential or concerted.

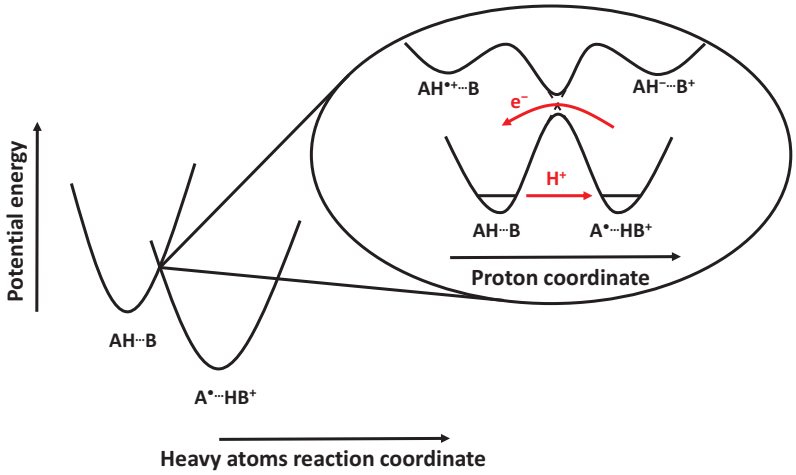

Figure 2.11: CPET potential energy profiles for the reorganisation of heavy atoms in the system (parabolas) and for the proton transfer concerted with the electron transfer at the transition state (inset).

Experimental studies of CPET reaction

The model described above for CPET reactions was developed in regards with experimental electrochemical data.[22] Experimental examples of CPET reaction studied in the laboratory prior to my venue consisted in (i) the oxidation of phenol derivatives as a model for the oxidation of a tyrosine residue nearby the active site of the oxygen–evolving complex (OEC) in photosystem II (Figure 2.12, left);[26] (ii) the oxidation of an osmium complex coordinating a water molecule as an illustration of PCET reaction involving a metal centre;[27] (iii) the reduction of superoxide ion in an aprotic solvent, where water molecules played the role of proton donor during the reductive process;[28] and (iv) the oxidation of benzoquinones bearing carboxylic acid groups as an example of a proximal proton accepting group can influence the mechanistic pathway.[29]

Among these studies, a seminal paper from the group on the electrochemical oxidation of phenols with an attached proton acceptor has attracted much of my attention.[30] The model system, an aminophenol (Figure 2.12, right), showed that oxidation of phenols in aprotic solvents was facilitated by the presence of an H–bonded amine group, with a small but definite H/D KIE. The different mechanistic pathways depicted in figure 2.9 have been envisaged and confronted to the theoretical model presented above, and it has been evidenced that the CPET route prevails in this system. From the conclusions of this study, we will now discuss the strategies developed to extend the concept of a pending donating / accepting group nearby a redox event implying long range proton transfer or proton transfer and bond breaking.

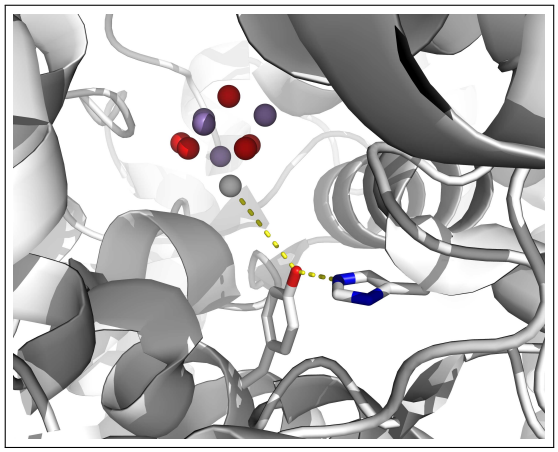

Figure 2.12: Left: X–ray structure of the OEC proximal Tyr161–His190 couple in photosystem II (PDB ID, 3ARC);[31] purple spheres: Mn; white sphere: Ca; red spheres: O. Right: Schematic representation of the aminophenol oxidation, model of the tyrosine–histidine couple.

Cyclic voltammetry setup

In a typical cyclic voltammetric experiment, we use a three–electrode setting containing the electroactive species at a millimolar concentration and a supporting electrolyte. Glassy carbon is used as the working electrode (WE) where the electron transfer occurs, platinum as the counting electrode (CE) to collect the current and aqueous saturated calomel electrode (SCE) as the reference electrode (RE). The double–wall jacketed glassy cell can be thermostated by circulation of water and to neglect any convection phenomenon the solution is not stirred. A potentiostat is connected to these electrodes and allow to set a known potential at the working electrode relative to the reference electrode.

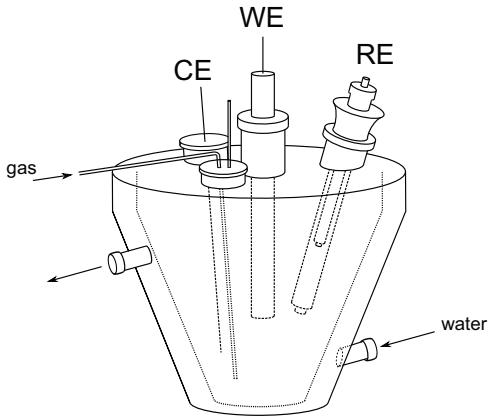

2.3.3 Proton–coupled electron transfer and relays

Long–distance electron and proton transfer are key processes in a considerable number of both biological and synthetic systems. The Grotthuss mechanism is the paradigm that defines proton transfer through a water molecules wire.[32, 33] A seminal example is photosystem II, the enzyme responsible for water oxidation, where the protons generated after the oxygen evolution are driven from the buried active site towards the surface of the enzyme by an array of water molecules and amino acids (Figure 2.13). The possibility that these transfers might be concerted has been at the centre of my research for the past 7 years, and we aim at developing new biomimetic systems to study such reaction by the mean of electrochemical techniques.

Grotthuss mechanism

Scheme of the Grotthuss mechanism concept of structural diffusion of excess protons in a hydrogen–bonded water molecule network. Only water molecules that contribute to the transient Grotthuss wire of hydrogen–bonded molecules are depicted.

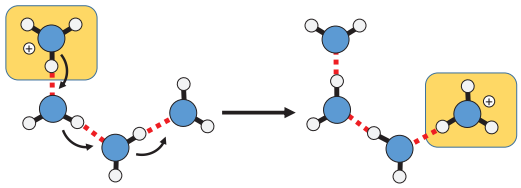

Due to the fact that efficient proton tunnelling is required, the occurrence of concerted processes presupposes the presence of short distances between the group generating the proton upon oxidation and the proton acceptor, i.e. that the two groups are connected via a hydrogen bond. Indeed, the distances over which the proton may travel are limited to the rather small distances, in contrast with the electron in outer sphere electron transfer reactions with no coupled proton transfer. To start with, we had to develop a synthetic system with an oxidable proton donor, a relay and a proton acceptor, and where the proton transfer distances would be respected.

We prepared a series of molecules containing an oxidizable phenol (as proton donor), a pyridine group (as proton acceptor) and an alcohol group between them, in order to test the concept of H–bond relay (Figure 2.14).[34, 35] Electrochemical oxidation was investigated by means of cyclic voltammetry and compared with the response obtained with a previously investigated amino phenol, in which the proton generated by phenol oxidation travels directly to the amine in the absence of H–bond relay.[30] The voltammograms displayed a partial chemical reversibility, the cathodic reverse trace corresponding to the re–reduction of the phenoxyl radical generated during the oxidation (Figure 2.15). The kinetics of this electrochemical electron transfer reaction can be derived from the distance between the anodic and cathodic peak, based on the Butler–Volmer equation:

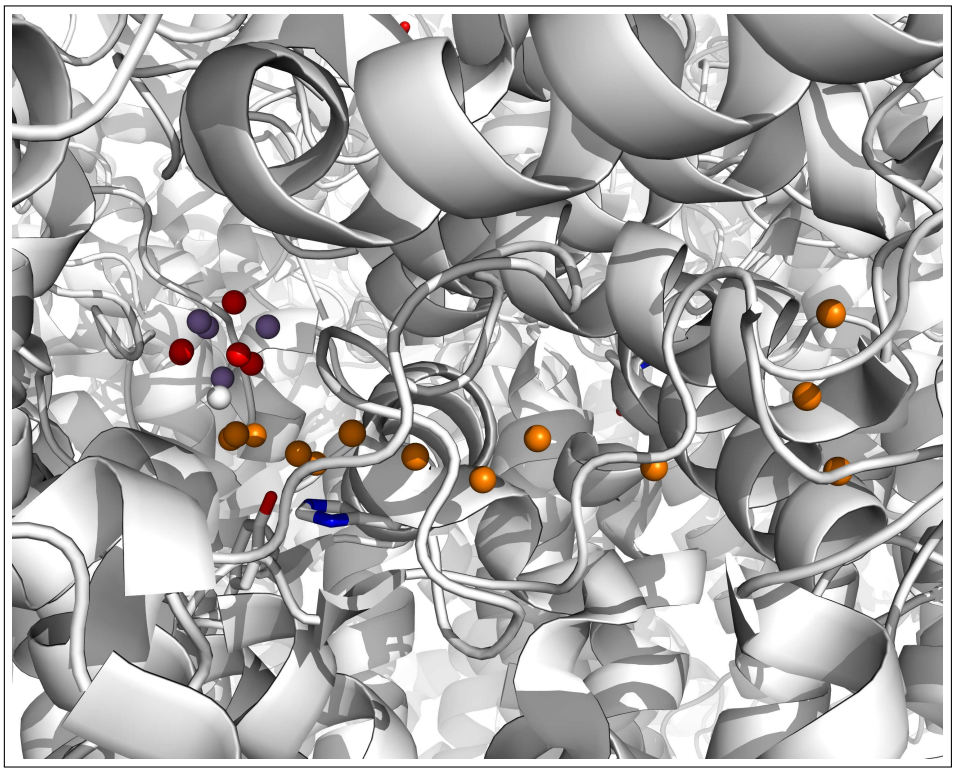

Figure 2.13: Structure around Tyr161 in photosystem II emphasizing the hydrogen bond pattern from the OEC to the luminal bulk phase, according to the 1.9 Å structure (PDB ID, 3ARC).[31] OEC: purple spheres: Mn; white sphere: Ca; red spheres: O. Water molecules participating in the hydrogen–bond network are depicted in orange.

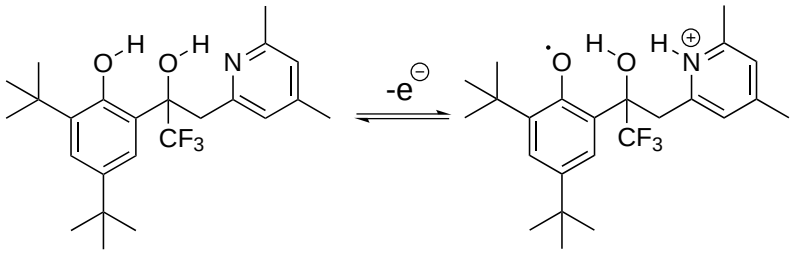

Figure 2.14: Schematic representation of the H–bond relay molecule oxidation.

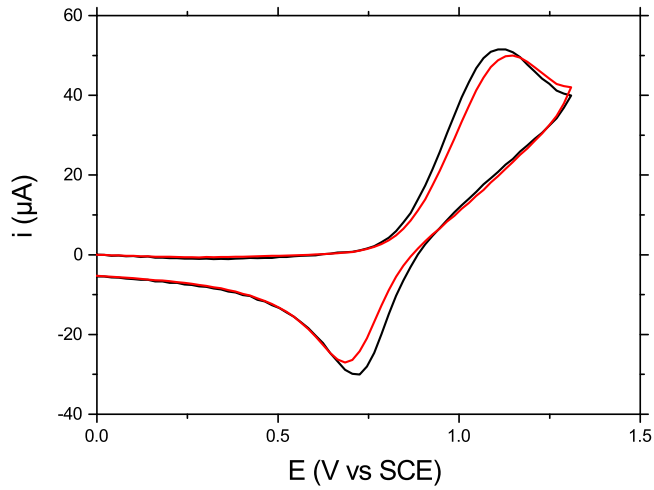

Figure 2.15: Cyclic voltammetry of 1 mmol/l H–bond relay compound in acetonitrile with 0.1 mol/l of n–Bu_4NBF_4 at 0.2 V/s (working electrode: glassy carbon disk electrode). Black: + 1 % MeOH; red: + 1 % MeOD.

$$\frac{i}{FS} = k_s \exp\left[\frac{F}{2RT}(E - E^\circ)\right]\left\{[Red] - \exp\left[-\frac{F}{RT}(E - E^\circ)\right]\right\}[Ox] \tag{2.9}$$

where [Red] and [Ox] are the concentrations of reduced and oxidized forms at the electrode surface. Variations with temperature led to an Arrhenius plot that may be described by:

$$\ln k_s = \ln Z^{het} - \frac{1}{4RT}(\lambda + 2F_{\phi_S} + 4\Delta ZPE^{\neq} - 2\Delta ZPE) \tag{2.10}$$

where ϕ_S is the potential difference between the solution and the reaction site and $\Delta ZPE^{\neq}$ and ΔZPE are the zero–point energies in the transition state and in the initial state, respectively.

An H/D KIE of 2.9 is observed (Figure 2.15), and is pointing to the occurrence of a concerted pathway. It is interesting to note that for the relay molecule, the term $\lambda + 2F_{\phi_S} + 4\Delta ZPE^{\neq} - 2\Delta ZPE = 1.55$ eV, which is almost the same as for the aminophenol, and quantum chemical estimates of λ_i showed that it is practically constant. Furthermore, solvent reorganization and other parameters are also expected to be similar among these compounds. It thus appears that reorganization parameters are not the main factors that make the CPET oxidation of H–bond relay molecules intrinsically slower than the oxidation of the aminophenol, in which a single proton is moved concertedly with electron transfer. The reason is essentially related to the magnitude of the pre–exponential factor Z, which is a measure of the efficiency of proton tunnelling concerted with electron transfer.[34] We could therefore conclude that the efficiency of tunnelling is less in the case of the relay molecules, where two protons are moved concertedly with electron transfer, than in the case where a single proton is transferred. An independent theoretical study on this

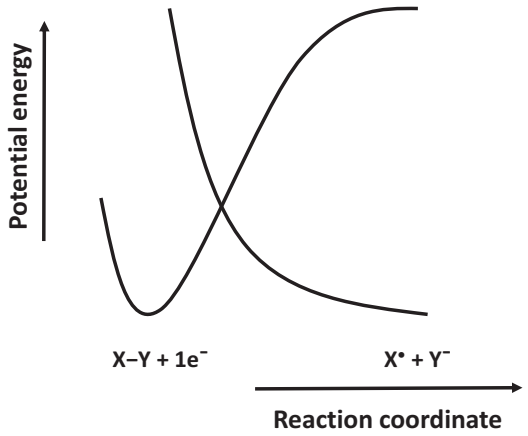

Figure 2.16: DET model potential energy profiles.

system by the group of Prof. Hammes–Schiffer came to the same conclusion, i.e. that the rate constant for the CPET reaction is lower when two protons are transferred because of the smaller overlap integral between the reduced ground state and the oxidized proton vibrational wave functions.[36]

This 'Grotthuss–like' proton transfer over (formally) 2.5 Å avoids going through a high–energy intermediate where the relay would be protonated. This simple model led us to pave the way towards more complicated systems, where the nature and the number of relays could be modified. The aim is now to design a more biological relevant model, where water itself could play the role of the relay. This prospect will be detailed in the perspectives chapter (see section 3.2).

2.3.4 Proton–coupled electron transfer and bond breaking

O–O bond

Electron transfer to a molecule is often associated to molecular modifications that can lead sometime to bond breaking in a dissociative electron transfer (DET). Unlike the Marcus–Hush model, which only considers outer sphere electron transfers, the elaboration of a model for DET reactions is based on Morse curve potential energy profile for the bond cleavage and repulsive Morse curve for the broken bond (Figure 2.16).[37] This model has been validated by numerous experimental examples involving electrochemical electron transfers as well as thermal or photochemical homogeneous electron transfers. We can further note that DET mechanism is involved in numerous natural and artificial reactions, such as in reductive dehalogenase enzymes which are responsible for carbon–halogen bond breaking. The reductive bond cleavage associated with a proton transfer can also be found in nature and in catalytic processes. For instance, oxygen activation in cytochrome C oxidase involves electrons, protons and the cleavage of an O–O bond to release two molecules of water:

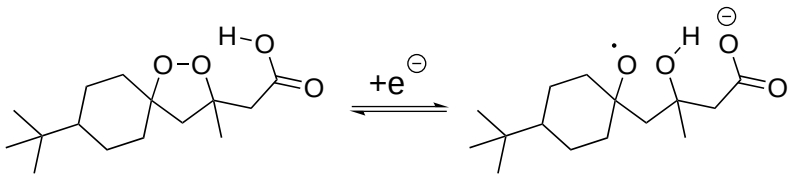

Figure 2.17: Schematic representation of the cycloperoxide reduction.

$$O_2 + 4\,H^+ + 4\,e^- \longrightarrow 2\,H_2O \tag{2.11}$$

In this study, we intended to shed light on the coupling between DET and PCET reactions in a model compound to understand the degree of concertedness between all three events, i.e. electron transfer, proton transfer and bond cleavage. The 'all in concert' pathway would be susceptible to give a huge thermodynamic gain, but these three events may not occur in a concerted way, and sequential routes have to be considered. The competition between the different pathways had therefore to be addressed by experimental and theoretical studies.

To illustrate this type of reaction, we choose to look at the reductive cleavage of an O–O peroxo bond in the presence of a pending proton donor (Figure 2.17).[38, 39] It is now well described that the electrochemical reduction of aliphatic peroxides studied in an aprotic solvent consists in a DET, in which the O–O bond is cleaved concertedly with electron transfer thus generating a broken anion radical.[40] The total gain in driving force expected should approximately correspond to the difference of pKa between the alcohol formed upon reduction and the proximal acid (i.e. 19 pH units from the pKa of tert–butanol and the pKa of acetic acid in DMF, equivalent to −1.11 eV in terms of free energy).

Looking at the general scheme where the different mechanistic possibilities are summarized (Figure 2.19), it appears that the two outer–sphere electron transfer routes (in black and in green) can be ruled out by the general DET to aliphatic peroxides, as already mentioned above. Among the two remaining possibilities, the stepwise pathway where the electron transfer is concerted with the bond–breaking followed by the protonation step (in blue) is not in line with the increase of driving force, but is simply driven by the thermodynamics of the first step (i.e. the peak potential of the cycloperoxide–carboxylic acid compound should in this case be similar to that of the cycloperoxide–methyl ester compound where protonation is not involved). Comparison between the cyclic voltammetric response of the cycloperoxide bearing the carboxylic acid and the corresponding methyl ester, where the proton transfer is not allowed, shows a dramatic peak potential shift of +0.7 V (Figure 2.18). This observation therefore rules out the occurrence of this stepwise DET/proton transfer pathway.

The all–concerted pathway (in red) is thus the only route remaining that could satisfy the experimental observations. A theoretical model has been developed for this concerted

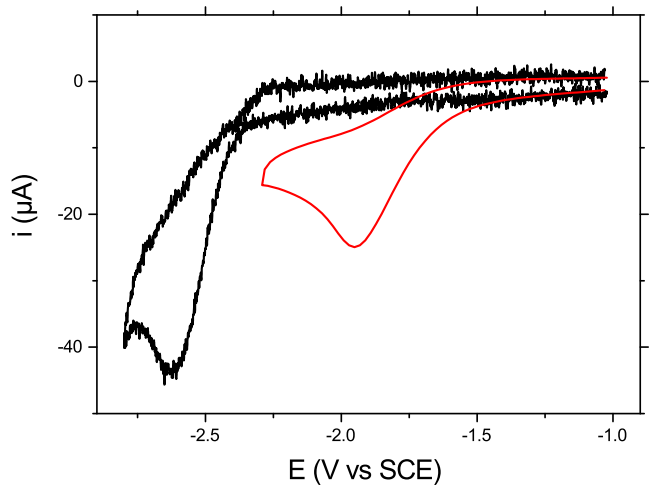

Figure 2.18: Cyclic voltammetry of 2 mmol/l cycloperoxide–carboxylic acid compound (red) and cycloperoxide–methyl ester (black) in DMF with 0.1 mol/l of n–Bu_4NBF_4 at 0.2 V/s (working electrode: glassy carbon disk electrode).

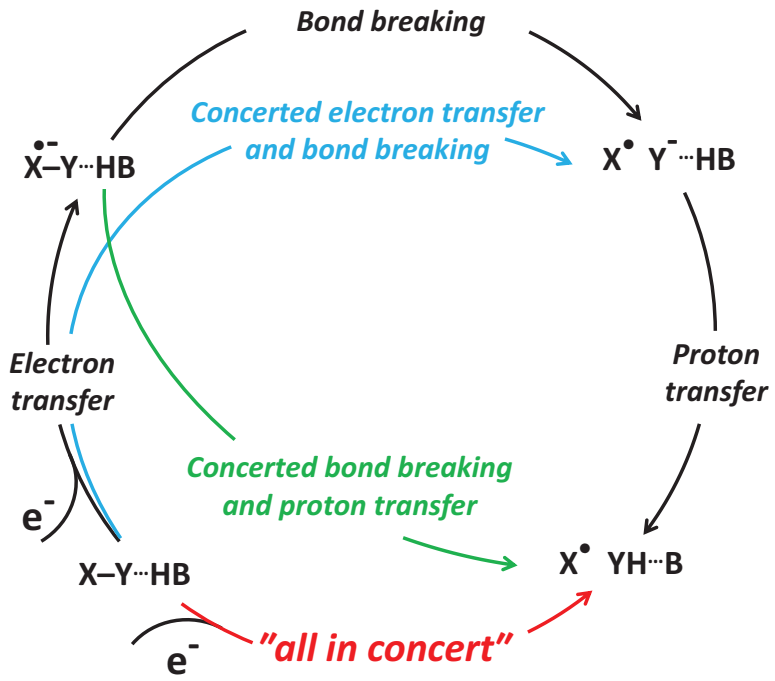

Figure 2.19: Stepwise and concerted pathways in reactions where electron transfer is coupled with heavy–atom bond cleavage (Y–X) and proton transfer.

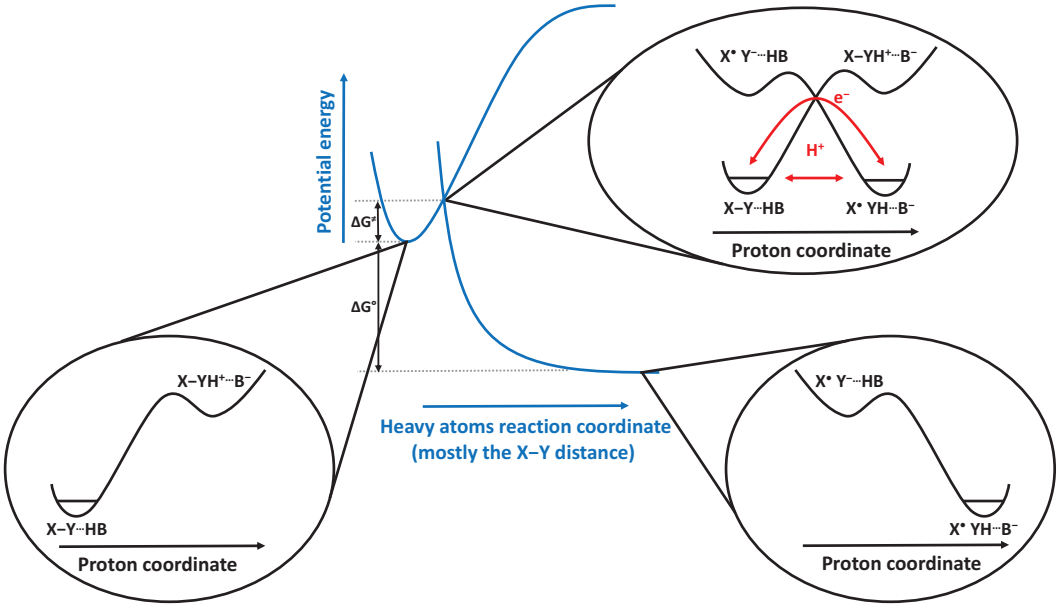

Figure 2.20: Concerted electron transfer, proton transfer and bond breaking potential model energy profiles.

proton–electron–bond breaking reaction.[38] A combination between the CPET and the DET models has been established to express a relation between the rate constant and the driving force. As in the case of the CPET model, two successive Born–Oppenheimer approximations have been applied (Figure 2.20). The first one defines the transition state in terms of heavy atoms coordinates, which takes into account the solvent reorganisation, the vibrations of reactant bonds not being cleaved during the reaction, and the contribution of bond cleavage. Such as in the case of DET reactions, the bond breaking contribution is describe by a Morse curve for the reactants and a repulsive Morse curve for the products. The second Born–Oppenheimer approximation at the transition state distinguishes the proton and the electron transfer. Following this model, cyclic voltammogram simulations allowed us to correctly reproduce the experimental voltammograms. Finally, we observed that the peak potential difference is 0.7 V rather than the expected 1.1 V value, which could be explained by a charge dipole interaction between the radical and the anion.

To conclude, a theoretical model supported by an experimental system evidenced the relevance of the proposed 'all in concert' mechanism, where electron and proton are transferred while the bond is broken. Since then, this model has also been applied by the group to catalytic systems, such as the reduction of carbon dioxide by iron(0) porphyrins.[41]

N–N multiple bonds

N–N multiple bonds activation has focused a long–standing interest, notably due to the dinitrogen reduction to ammonia reaction:

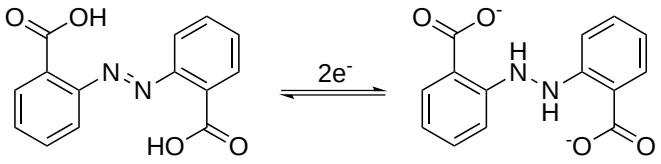

Figure 2.21: Schematic representation of the azobenzene reduction.

$$N_2 + 6\,H^+ + 6\,e^- \longrightarrow 2\,NH_3 \tag{2.12}$$

This reaction has attracted much attention over the past decades, particularly due to the fact that biological N_2 fixation can be performed at ambient pressure and temperature by nitrogenase enzymes, with a heterometallic iron/molybdenum/sulfur/carbon cluster active.[42] The need for mechanistic studies for the strong N–N multiple bonds activation is thus imperative to unravel general trends towards the design of new types of electrocatalysts.

A similar strategy as for the O–O bond reduction has been undertaken (see section 2.3.4), with the design of an organic molecule bearing a N=N bond with pendant H–bonded acid groups. The role of proximal acid/base couples on the reduction/oxidation of the N=N/HN–NH couple has been investigated on azobenzene derivatives with carboxylic acids (Figure 2.21).[43]

The cyclic voltammetric responses confirmed that the azo and hydrazo compounds are redox partners: the reverse trace of the azo compound is similar to the forward trace of the hydrazo compound, and *vice versa* (Figure 2.22). Methylation of the carboxylic acid showed a considerable shift in potential towards negative values (ca. -0.8 V), rendering the reduction of the azo bond more difficult, similar to what was observed in the case of the cycloperoxide reduction (see section 2.3.4). We thus have demonstrated that the presence of proximal proton sources could give a huge thermodynamic raise that helps the N=N/HN–NH bond breaking/formation.

To understand the reasons for such dramatic effect on the reduction potential, we performed cyclic voltammogram simulations and DFT calculations, and demonstrated that: (i) intramolecular electron and proton transfers occur in a stepwise manner, rather than concertedly (no H/D KIE observed); (ii) intramolecular PCET in these molecules is accompanied by considerable structural changes, affecting the kinetic of the electron transfer. In terms of catalysis, these conclusions are of crucial importance to develop effective molecular catalysts bearing pendant acidic moieties for N–N bond(s) activation.

Following these conclusions, we are currently focusing on the second 2–electron reductive step for the hydrazobenzene-carboxylic acid derivative which should end up to the N–N bond breaking to release aniline–carboxylate. In a near future we also envisage to link the two aromatic rings in order to render the N–N bond breaking chemically reversible.

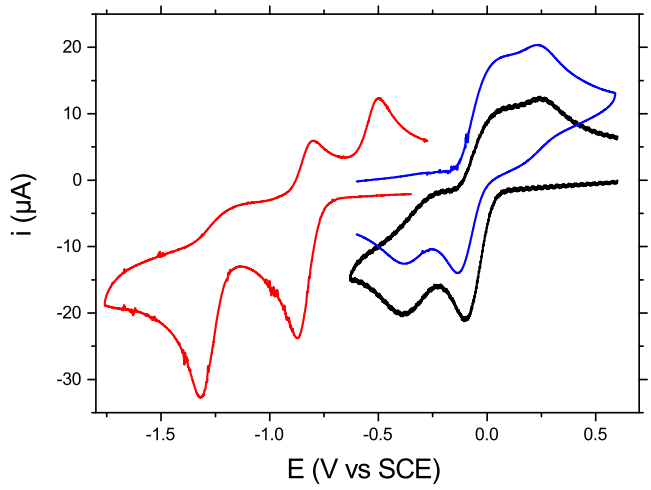

Figure 2.22: Cyclic voltammetry of 1 mmol/l azobenzene–carboxylic acid compound (black), hydrazobenzene-carboxylate (blue) and azobenzene–methyl ester (red) in DMF with 0.1 mol/l of n–Bu_4NBF_4 at 0.2 V/s (working electrode: glassy carbon disk electrode).

2.3.5 Proton reduction electrocatalysis by Fe/S nanoparticles

Molecular catalysis[†] can be somehow limited in terms of applications, mainly due to the stability of the catalysts and the difficulty to separate the products from the catalyst. If we consider stability, robustness or ease of preparation, electrocatalysis [†] can often be of primary interest. Inspired by my previous experiences with nanoparticles and iron–sulphide systems, I started this project to bring a different view into the group for the study of catalysis of small molecules activation by electrochemical techniques. I began this new work in collaboration with Dr. Marion Giraud for the synthesis of the nanocatalysts (ITODYS, Université Paris–Diderot), and the project is currently funded with an ANR JCJC grant that I am leading (funding RF5). We had one post-doctoral fellow and four undergrad students involved in this project over the past 4 years.

Molecular hydrogen is currently at the forefront for the prospect of new energy vectors as a way to store energy in chemical bonds. Its clean, cold combustion in fuel cells or its production in water electrolyzers will require the replacement of noble–metal catalysts such as platinum and its alloys by earth–abundant catalysts for proton reduction into dihydrogen if worldwide use of hydrogen is considered. As introduced in section 2.1, hydrogenase metalloenzymes are capable of reversibly converting protons into molecular hydrogen. Biomimetic synthetic molecular electrocatalysts, in solution or grafted onto an electrode, are currently presenting poor to moderate activity toward molecular hydrogen evolution or uptake reactions.[7] Furthermore, examples of functional molecular

[†] *Molecular catalysis* is coined here to define catalyst molecules homogeneously dispersed in solution or immobilized in a mono– or multi–layer coating on the electrode surface, as opposed to *electrocatalysis* which involves the electrode material as the catalyst.[44]

non–precious–metal catalysts operating at low overpotentials and high current densities under mild conditions (ca. pH 7, 1 atm, room temperature) that would compete with natural enzymes or platinum itself are scarce. Recently heterogeneous electrocatalysts, in the form of electrodeposited bulk material or nanoparticles, based on molybdenum sulphide,[45, 46, 47, 48] cobalt sulphide,[49] cobalt phosphate,[50] iron [51] or nickel [52] phosphides, and alloys of nickel–molybdenum [53, 54] have been reported for their high activity toward molecular hydrogen evolution in acidic or neutral water at relatively low overpotentials. Given the ubiquity of iron sulphide minerals in nature, such as pyrite FeS_2 which is the most abundant mineral on the Earth's surface,[55] we decided to investigate iron sulphide nanomaterials as a bio–inspired catalyst that would combine features from the natural enzyme (the Fe/S core) and high stability and robustness given by the nanostructuration of the material.

We prepared pyrrhotite FeS nanoparticles, using the solvothermal approach, by decomposition of $Fe_2S_2(CO)_6$ complex in octylamine at 280 °C.[56] Characterisation by energy-dispersive X–ray (EDX), thermogravimetric analysis (TGA), transmission electron microscopy (TEM), scanning electron microscopy (SEM), X–ray diffraction (XRD) and Mössbauer spectroscopy allowed us to probe the nature of the particles, their morphology and the local chemical environment around the iron, thus describing the system as a $Fe_{1-x}S$ structure ($0 \leq x \leq 0.125$) (Figure 2.23).

Solvothermal synthesis

In nanoscience, the solvothermal synthesis is used to prepare nanometric size crystals that cannot be formed from other synthetic routes. This soft chemistry process involves the use of a solvent under moderate pressure and temperature conditions, and dissolved precursors. By manipulating the experimental conditions (concentration of the precursors, nature of the solvent, temperature, pressure, etc...) one can control the size, shape, nature and crystallisation of the nano–objects.

Long–duration controlled–potential electrolysis (CPE) was performed to assess the durability and robustness of a FeS nanoparticle–coated glassy carbon electrode (Figure 2.24, dashed line). Quantitative (≥ 0.99) Faradaic yield for molecular hydrogen evolution was confirmed by gas chromatography analysis as well as by volumetric measurements of the gas evolved. The decrease in the slope of the Q versus time curve is due to the pH increase of 0.3 unit caused by proton consumption. To further investigate this point, the crucible coated with the FeS nanoparticles was refilled with a fresh solution of 1 mol/l phosphate buffer at pH 7.0, and an identical Q versus time profile was obtained over a 1 day electrolysis under the same experimental conditions (Figure 2.24, solid line). Again, an almost quantitative Faradaic yield (≥ 0.98) was obtained for H_2 generation, outlining the remarkable stability of such nanoparticles over the course of catalysis. No particular care

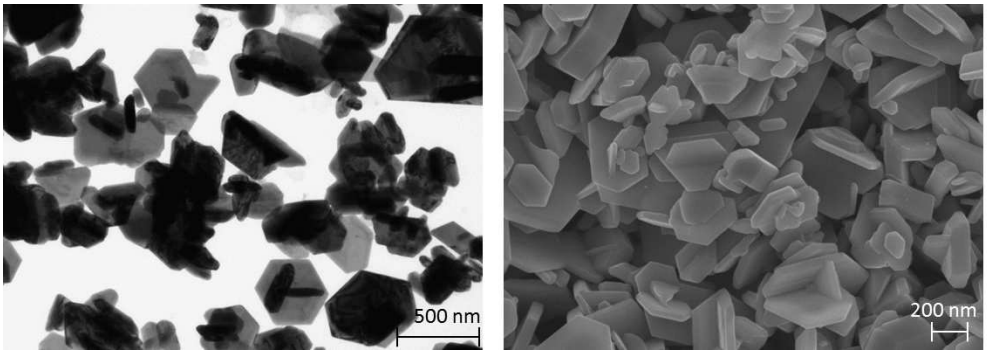

Figure 2.23: TEM and SEM images of FeS–nanoparticles.

in storage of the catalyst or pre–degassing of the phosphate buffer solution was required, demonstrating the long–term stability of this material. After these 6 days of electrolysis, no major structural changes in the electrolysed catalyst were observed by XRD, and the morphology of the FeS nanoparticles was also found to be unchanged. Following these conclusions, a patent has be deposited,[57] opening the way towards the development of a new class of cheap and robust electrocatalysts based on iron sulphide nanoparticles. This prospect will be detailed in the perspectives chapter (see section 3.3.1).

Despite the fact that these FeS–nanoparticles seem at first to compare less favourably, with materials such as cobalt phosphate [50] or molybdenum sulphide [47] (Table 2.1), the remarkable stability and the ease of preparation are clearly showing that iron sulphide materials are very promising. If we now compare the abundance and cheapness of the different materials, iron sulphide nanoparticles could be favoured compared to cobalt phosphate or molybdenum sulfide materials. A rough comparison between the different metal prices shows that in 2013, iron ore (96 $/t) was much cheaper than nickel (17,530 $/t), molybdenum (28,100 $/t) or cobalt (30,400 $/t), the platinum–group metal being itself much more expensive (19,500,000 $/t).[58] We can therefore envisage that iron sulfide nanoparticles may offer a great advantage in term of cost and availability compared to other transition metal electrocatalysts for molecular hydrogen evolution and further investigations on related materials are currently in progress.

We also have to bear in mind that this comparison with existing materials has not been optimised in the sense that they have not been carried on a rational comparison including the parameters controlling the catalytic current (catalyst loading of the electrode, thickness of the film,...). These aspects will be developed in the perspective chapter (see section 3.3.2).

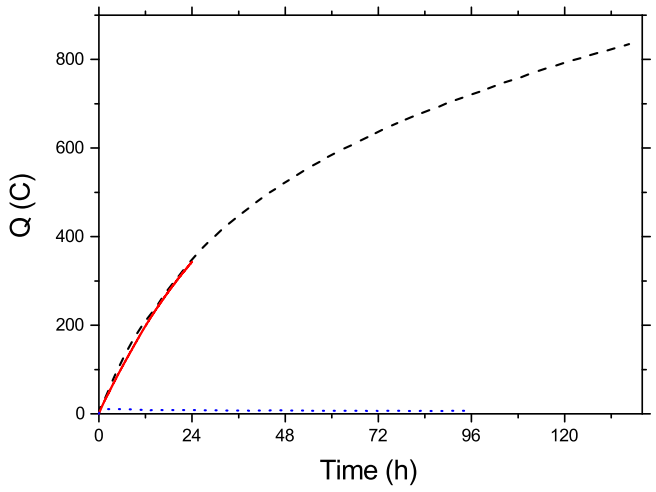

Figure 2.24: First (dashed black line) and second (solid red line) CPE of a FeS nanoparticle–coated glassy carbon electrode at an overpotential of 350 mV (−0.763 V *vs.* NHE) in 1 mol/l potassium phosphate buffer at pH 7.0, showing charge build–up versus time ($Q = f(t)$) for the cell with (dashed black line) and without (dotted blue line) FeS–nanoparticles.

Table 2.1: Exchange current densities (J_0) of different electrocatalysts, in water at pH 7.0 (data extracted from polarization curves)

Material	J_0 (mA/cm^2)	Slope (mV/ dec)	Range of η (mV)	References
Co–MoS_3	1.1×10^{-2}	87	87 – 122	[47]
Ni–MoS_3	1.0×10^{-2}	96	110 – 144	[47]
Fe–MoS_3	4.8×10^{-3}	95	137 – 176	[47]
Co/P/O	1.9×10^{-3}	134	200 – 300	[50]
MoS_3	8.9×10^{-4}	86	171 – 203	[47]
FeS	6.6×10^{-4}	150	350 – 450	[56]

Chapter 3

Perspectives

3.1 Preamble

The main line of the different scientific projects I have been involved in so far is driven by the interplay between protons and electrons in 'bio–inspired' or 'biomimetic' systems. Following this track, I intend to pursue two main directions for the next ten years. To begin with, I will focus on the development of the cheap, robust and sustainable iron sulphide–based electrocatalysts described previously, extending their applications towards other reactions and implement them into functional devices. Considering the promising results obtained so far and the amount of manpower engaged, this project is expected to go on for the next 5–7 years. The second orientation of my research will concern a more fundamental topic, the mechanistic study of long–range proton transfer following an electron transfer within a protein–like environment. This project is much more precarious due to the fact that a biomimetic model has still yet to be constructed, but some preliminary systems have already been investigated and gave us some ideas about the difficulties that could be encountered. Regarding the hardship of this proposal, I expect that the design and synthesis of a decent model combined with solid electrochemical mechanistic studies would take some 5–7 years to be completed.

3.2 Long–range proton–coupled electron transfer in biomolecules

The approach proposed in this project aims at preparing nano–channels in order to trap water molecules within a biomimetic controlled environment to study the mechanism of proton transfer upon a redox event from a proton donating group to a proton accepting group. As underlined above (see section 2.3.3), long–distance proton transfer coupled with electron transfer are ubiquitous in Nature, and are notably used to control the electro–neutrality around catalytic active sites upon oxidation or reduction (i.e. water oxidation in photosystem II or hydrogen evolution in hydrogenases). Electrochemical mechanistic investigations of such systems should elucidate the role of the water molecules or the

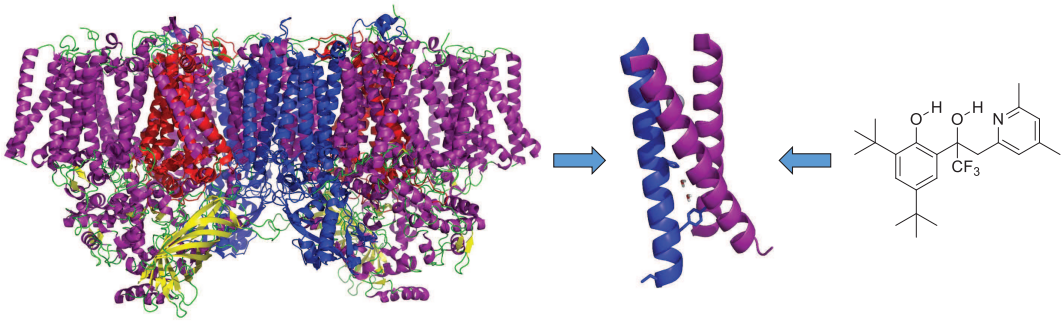

Figure 3.1: Representation of the 3SCC approach, with the crystal structure of the photosystem II enzyme (PDB ID, 3ARC (left), the 3SCC model peptide (middle) and the H–bond relay molecule (right).

influence of the distance between the proton donor and the proton acceptor regarding the long–range PCET reaction.

Following the study of the simple model system where an alcohol moiety played the role of relay, we intend to extend the complexity by investigating more biologically relevant biomimetic systems. Biological water channels such as aquaporins [59] or proton transfer proteins such as gramicidin [60] have been envisaged as potential candidates for our study, but the main drawback of these systems was that their functionalisation with proton donating and accepting groups is not straightforward.

We then considered hydrophobic channels, as it has been shown that water molecules placed in a hydrophobic pore may be able to drive protons extremely rapidly by a Grotthuss mechanism.[60] Do do so, I started a collaboration with the group of Prof. Vincent L. Pecoraro in 2012 (collaboration SC6) to synthesise asymmetric self–assembling peptides. Three–stranded coiled coil (3SCC) peptides provide a veritable bottom–up approach to the *de novo* design of model peptides.[61] *De novo* design differentiates from other types of protein design strategies as it is based on 'first principles'; this paradigm refers to the postulation that the primary amino acid sequence controls the three–dimensional structure of a protein. These self–assembling structures can be engineered so as to contain catalytic metal centres or chosen amino acids for specific applications.

Interestingly, most of the functional metalloenzyme mimics are associated with α–helical coiled coils. This structural organisation would allow us to benefit from the inner channel of the α–helix, which contains water molecules, to study proton transfer between a proton donor and a proton acceptor within a protein environment. Thus, the protein design allow us to step our study on a well defined biologically relevant system, in between a purely synthetic model, such as the 'H–bond relay molecule' (see section 2.3.3), and an entire enzyme system, such as the photosystem II (Figure 3.1).

Our strategy is based on an asymmetric 3SCC structure, in which only one of the three strands features a tyrosine residue and an histidine residue to investigate a potential long–range PCET reaction (Figure 3.1, blue helix). The tyrosine residue is thus buried in the

core of the 3SCC so as to impair coupling reactions. Unfortunately, the electrochemical study showed so far that the phenoxyl radical generated upon oxidation is not stable within the time scale of the experiment, and probably reacts with neighbouring amino acids within the channel. We then have to envisage other strategies to release that proton upon oxidation, and a new system has yet to be designed and synthesised.

3.3 Chalcogenide transition metal nanoparticles for small molecules activation

3.3.1 FeS nanoparticles

The results obtained so far on the electrochemical studies of pyrrhotite–like FeS nanoparticles showed that this type of material exhibit a good catalytic activity towards molecular hydrogen evolution in neutral water with significant robustness and stability (see section 2.3.5).[56, 57] This study inspired us to pursue the development of new catalysts based on this iron sulphide composition, bearing in mind that we want to formulate *cheap*, *sustainable*, *robust* and *easily prepared* materials from *abundant natural resources*. We thus intend to prepare new stoichiometric compositions (i.e. greigite Fe_3S_4 or pyrite FeS_2) to investigate whether other type of FeS materials could give better activities for proton reduction than pyrrhotite nanomaterials.

Still inspired by biological metalloenzymes, we also envisage to prepare transition metal–doped FeS nanoparticles. Indeed, several FeS–metalloenzymes are known to catalyse small molecule activation in the presence of an extra transition metal (Figure 3.2), such as molybdenum in the case of the nitrogenase (reduction of N_2 into NH_3) [42] or nickel in the case of the carbon monoxide dehydrogenase (reduction of CO_2 into CO) [62] and [NiFe]–hydrogenase (reduction of H^+ into H_2).[4] By incorporating some controlled amount of cheap and abundant transition metals into the composition of FeS nanoparticles, we intend to modify the catalytic activity of the nanocatalysts. We also aim at open up their reactivity towards other small molecule activation reactions, such as those depicted for the biological systems. These synthesis of such nanoparticles will be carried out in collaboration with Dr. Marion Giraud (ITODYS, Paris–Diderot), with the correlated electrochemical studies done at the LEM.

3.3.2 Proton–electron transport and transfer in electrocatalytic films

The benchmarking of different catalysts is a laborious task, difficult in the sense that each experimentalist do not study a given material in the same experimental conditions. Therefore, there is a need to identify intrinsic parameters that would allow to get a fair comparison between different materials. The work presented so far on this thematic did not include any mechanistic study on the interplay between protons and electrons within the catalytic film. To identify the factors that are driving the catalytic performances, we need to address a methodology to understand such issues.

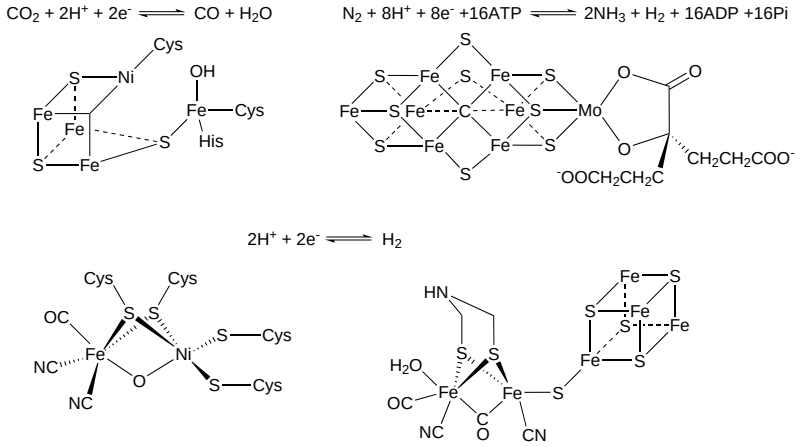

Figure 3.2: Schematic representation of FeS–enzyme active sites of CO–dehydrogenase (top left),[62] nitrogenase (top right),[42] [NiFe]–hydrogenase (bottom left) and [FeFe]–hydrogenase (bottom right).[4]

A seminal study on this problematic has recently been published in the group on a cobalt–based catalyst for oxygen evolution, where thermodynamic and kinetic characteristic have been derived to benchmark this catalyst vis–à–vis other competing materials.[63] In this particular case the material was electrodeposited, and the catalyst and the conducting material are the porous cobalt material, where the substrate and the product can be transported trough the film. We would like to extend this methodology to our type of systems where the catalytic nanoparticles are conducting but not in contact with each other. The dispersion of the FeS nanoparticles within a Nafion film allows the rapid diffusion of protons through the film and can control a certain homogeneity between the catalytic centres (Figure 3.3). We thus intend to extract from the analysis of electrochemical measurements the optimum parameters (film thickness, catalyst concentration, buffer concentration, etc...) to get a global benchmarking index able to present a reasonable comparison between catalysts studied in the same conditions. This part will be carried out with Prof. Cyrille Costentin and Jean–Michel Savéant.

3.3.3 Photoelectrocatalysis

Solar energy is considered as the most interesting renewable source of energy through its worldwide uniform accessibility, as opposed to wind power, hydroelectricity or geothermal energy. However, the day / night alternation, the latitude, and the meteorological and seasonal variabilities induce a sporadic availability of the electricity generated. Furthermore, our energy consumption is itself intermittent, and can be in opposed phase with the solar–induced power generation. These considerations call for the development of energetic vectors to allow the solar energy gathered to be stored, redistributed and possibly transported.[‡] To do so, a solution would be to convert the solar energy into chemical

[‡]These statements and conclusions are also applicable to wind power electricity generation.

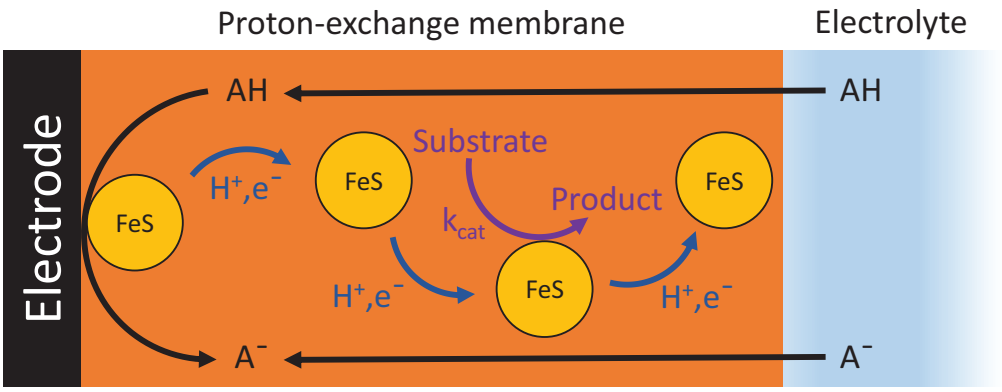

Figure 3.3: Schematic representation of a reductive electrocatayltic process within a proton–exchange membrane involving FeS nanoparticles.

energy, in the form of chemical bonds within molecules, similar to what Nature is doing with photosynthesis.[64, 8]

Thus we would like to investigate the ability for iron sulphide materials, and notably pyrite FeS_2, to harvest visible light in photovoltaic devices. Pyrite possesses semiconducting properties, with a weak band gap (0.95 eV) and a strong optical absorption,[65, 66] and is the most abundant mineral on Earth.[67] Combination of this photovoltaic device, in the form of a bulk material or as a nanoparticle, and the FeS nanoparticles within a solar cell is envisaged to photogenerate molecular hydrogen from water using visible light (Figure 3.4). At first, we do not intend to investigate the water oxidation at the (photo)anode, and we will just focus on the reductive part at the photocathode. The idea is to deposit the FeS nanoparticles on the semiconducting surface (i.e. pyrite) and by illuminating the device to observe evolution of hydrogen.

The proof of concept has yet to be performed. A possibility is that the photogenerated electrons may not be energetic enough to perform the catalysis, and then we may have to connect our system to a potentiostat to provide the extra energy required. Another issue that we may be facing at some point is the charge recombination after the irradiation, and understanding of charge–transfer processes is important in the perspective of designing light–harvesting assemblies.[68] On a long term view, the coupling of the reductive part with the oxidation of water on a (photo)anode is also planed to provide a functional device. This project will be undertaken within our group using the expertise in photochemistry of Dr. Julien Bonin.

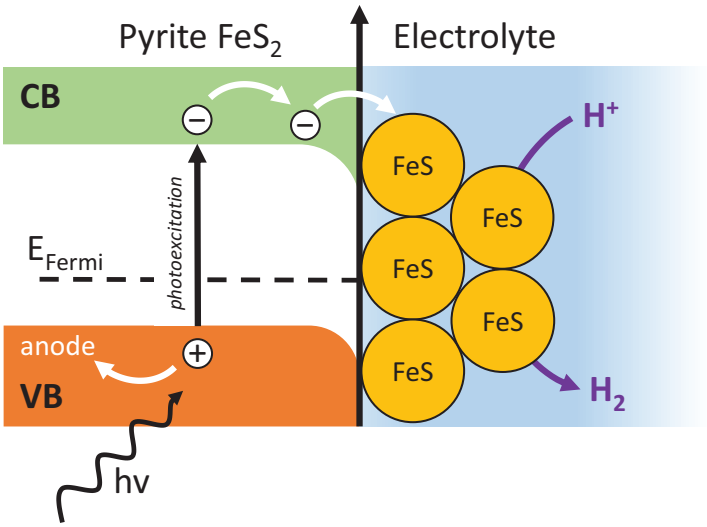

Figure 3.4: Schematic representation of the pyrite/FeS nanoparticle photovoltaic cell for hydrogen evolution.

Bibliography

[1] J. W. Peters, W. N. Lanzilotta, B. J. Lemon, and L. C. Seefeldt. X–ray crystal structure of the Fe–only hydrogenase (Cpl) from *Clostridium pasteurianum* to 1.8 angstrom resolution. *Science*, 282(5395):1853–1858, 1998. http://dx.doi.org/10.1126/science.282.5395.1853. 11

[2] Y. Nicolet, C. Piras, P. Legrand, C. E. Hatchikian, and J. C. Fontecilla-Camps. *Desulfovibrio desulfuricans* iron hydrogenase: The structure shows unusual coordination to an active site Fe binuclear center. *Structure*, 7(1):13–23, 1999. http://dx.doi.org/10.1016/S0969-2126(99)80005-7. 11

[3] A. Le Cloirec, S. P. Best, S. Borg, S. C. Davies, D. J. Evans, D. L. Hughes, and C. J. Pickett. A di–iron dithiolate possessing structural elements of the carbonyl/cyanide sub–site of the H–centre of Fe-only hydrogenase. *Chem. Commun.*, (22):2285–2286, 1999. http://dx.doi.org/10.1039/a906391i. 11

[4] W. Lubitz, H. Ogata, O. Rüdiger, and E. Reijerse. Hydrogenases. *Chem. Rev.*, 114(8):4081–4148, 2014. http://dx.doi.org/10.1021/cr4005814. 11, 41, 42

[5] H. Reihlen, A. Gruhl, and G. von Hessling. The photochemical and oxidative decomposition of carbonylene. *Liebigs Ann. Chem.*, 472:268–287, 1929. http://dx.doi.org/10.1002/jlac.19294720113. 11

[6] X. M. Liu, S. K. Ibrahim, C. Tard, and C. J. Pickett. Iron–only hydrogenase: Synthetic, structural and reactivity studies of model compounds. *Coord. Chem. Rev.*, 249(15-16):1641–1652, 2005. http://dx.doi.org/10.1016/j.ccr.2005.04.009. 11

[7] C. Tard and C. J. Pickett. Structural and functional analogues of the active sites of the [Fe]–, [NiFe]–, and [FeFe]–hydrogenases. *Chem. Rev.*, 109(6):2245–2274, 2009. http://dx.doi.org/10.1021/cr800542q. 11, 35

[8] B. A. Pinaud, J. D. Benck, L. C. Seitz, A. J. Forman, Z. Chen, T. G. Deutsch, B. D. James, K. N. Baum, G. N. Baum, S. Ardo, H. Wang, E. Miller, and T. F. Jaramillo. Technical and economic feasibility of centralized facilities for solar hydrogen production via photocatalysis and photoelectrochemistry. *Energ. Environ. Sci.*, 6(7):1983–2002, 2013. http://dx.doi.org/10.1039/C3EE40831K. 11, 43

[9] T. D. P. Stack and R. H. Holm. Subsite–specific functionalization of the $[4Fe–4S]^{2+}$ analog of iron–sulfur protein clusters. *J. Am. Chem. Soc.*, 109(8):2546–2547, 1987. http://dx.doi.org/10.1021/ja00242a067. 12

[10] C. Tard, X. M. Liu, S. K. Ibrahim, M. Bruschi, L. De Gioia, S. C. Davies, X. Yang, L. S. Wang, G. Sawers, and C. J. Pickett. Synthesis of the H–cluster framework of iron–only hydrogenase. *Nature*, 433(7026):610–613, 2005. http://dx.doi.org/10.1038/nature03298. 12, 13

[11] D. E. Schwab, C. Tard, E. Brecht, J. W. Peters, C. J. Pickett, and R. K. Szilagyi. On the electronic structure of the hydrogenase H–cluster. *Chem. Commun.*, pages 3696–3698, 2006. http://dx.doi.org/10.1039/b604994j. 13

[12] C. Tard, X. M. Liu, D. L. Hughes, and C. J. Pickett. A novel $\{Fe^{I}–Fe^{II}–Fe^{II}–Fe^{I}\}$ iron thiolate carbonyl assembly which electrocatalyses hydrogen evolution. *Chem. Commun.*, pages 133–135, 2005. http://dx.doi.org/10.1039/b411559g. 13

[13] M. H. Cheah, C. Tard, S. J. Borg, X. M. Liu, S. K. Ibrahim, C. J. Pickett, and S. P. Best. Modeling [Fe–Fe] hydrogenase: Evidence for bridging carbonyl and distal iron coordination vacancy in an electrocatalytically competent proton reduction by an iron thiolate assembly that operates through Fe(0)–Fe(II) levels. *J. Am. Chem. Soc.*, 129(36):11085–11092, 2007. http://dx.doi.org/10.1021/ja071331f. 14

[14] P. C. Ford. Photochemical and photophysical studies of tetranuclear copper(I) halide clusters: An overview. *Coord. Chem. Rev.*, 132:129–140, 1994. http://dx.doi.org/10.1016/0010-8545(94)80032-4. 15

[15] P. C. Ford, E. Cariati, and J. Bourassa. Photoluminescence properties of multinuclear copper(I) compounds. *Chem. Rev.*, 99(12):3625–3648, 1999. http://dx.doi.org/10.1021/cr960109i. 15

[16] S. Perruchas, C. Tard, X. F. Le Goff, A. Fargues, A. Garcia, S. Kahlal, J.-Y. Saillard, T. Gacoin, and J.-P. Boilot. Thermochromic luminescence of copper iodide clusters: The case of phosphine ligands. *Inorg. Chem.*, 50(21):10682–10692, 2011. http://dx.doi.org/10.1021/ic201128a. 16, 17

[17] M. Vitale, C. K. Ryu, W. E. Palke, and P. C. Ford. *Ab initio* studies of the copper(I) tetramers $Cu_4X_4L_4$ (X = I, Br, Cl). effects of cluster structure and of halide on photophysical properties. *Inorg. Chem.*, 33(3):561–566, 1994. http://dx.doi.org/10.1021/ic00081a026. 16

[18] C. Tard, S. Perruchas, S. Maron, X. F. Le Goff, F. Guillen, A. Garcia, J. Vigneron, A. Etcheberry, T. Gacoin, and J.-P. Boilot. Thermochromic luminescence of sol–gel films based on copper iodide clusters. *Chem. Mater.*, 20(22):7010–7016, 2008. http://dx.doi.org/10.1021/cm801780g. 16

[19] L. L. Xuan, S. Brasselet, F. Treussart, J.-F. Roch, F. Marquier, D. Chauvat, S. Perruchas, C. Tard, and T. Gacoin. Balanced homodyne detection of second–harmonic generation from isolated subwavelength emitters. *Appl. Phys. Lett.*, 89(12):121118–121113, 2006. http://dx.doi.org/10.1063/1.2356375. 19

[20] L. L. Xuan, C. Y. Zhou, A. Slablab, D. Chauvat, C. Tard, S. Perruchas, T. Gacoin, P. Villeval, and J.-F. Roch. Photostable second–harmonic generation from a single $KTiOPO_4$ nanocrystal for nonlinear microscopy. *Small*, 4(9):1332–1336, 2008. http://dx.doi.org/10.1002/smll.200701093. 19

[21] P. Wnuk, L. L. Xuan, A. Slablab, C. Tard, S. Perruchas, T. Gacoin, J.-F. Roch, D. Chauvat, and C. Radzewicz. Coherent nonlinear emission from a single KTP nanoparticle with broadband femtosecond pulses. *Opt. Express*, 17(6):4652–4658, 2009. http://dx.doi.org/10.1364/OE.17.004652. 19

[22] C. Costentin, M. Robert, and J.-M. Savéant. Concerted proton–electron transfers: Electrochemical and related approaches. *Acc. Chem. Res.*, 43(7):1019–1029, 2010. http://dx.doi.org/10.1021/ar9002812. 21, 25

[23] C. Costentin, M. Robert, and J.-M. Savéant. Update 1 of: Electrochemical approach to the mechanistic study of proton–coupled electron transfer. *Chem. Rev.*, 110(12):PR1–PR40, 2010. http://dx.doi.org/10.1021/cr100038y. 21, 24

[24] J.-M. Savéant. Electrochemical approach to proton–coupled electron transfers: Recent advances. *Energy Environ. Sci.*, 5:7718–7731, 2012. http://dx.doi.org/10.1039/C2EE03241D. 21

[25] S. Hammes-Schiffer and A. A. Stuchebrukhov. Theory of coupled electron and proton transfer reactions. *Chem. Rev.*, 2010(12):6939–6960, 2010. http://dx.doi.org/10.1021/cr1001436. 24

[26] C. Costentin, C. Louault, M. Robert, and J.-M. Savéant. The electrochemical approach to concerted proton–electron transfers in the oxidation of phenols in water. *Proc. Natl. Acad. Sci. U. S. A.*, 106(43):18143–18148, 2009. http://dx.doi.org/10.1073/pnas.0910065106. 25

[27] C. Costentin, M. Robert, J.-M. Savéant, and A.-L. Teillout. Concerted proton–coupled electron transfers in aquo/hydroxo/oxo metal complexes: Electrochemistry of $[Os^{II+}(bpy)_2py(OH_2)]^{2+}$ in water. *Proc. Natl. Acad. Sci. U. S. A.*, 106(29):11829–11836, 2009. http://dx.doi.org/10.1073/pnas.0905020106. 25

[28] C. Costentin, D. H. Evans, M. Robert, J.-M. Savéant, and P. S. Singh. Electrochemical approach to concerted proton and electron transfers. Reduction of the water–superoxide ion complex. *J. Am. Chem. Soc.*, 127(36):12490–12491, 2005. http://dx.doi.org/10.1021/ja053911n. 25

[29] C. Costentin, M. Robert, and J.-M. Savéant. Carboxylates as proton-accepting groups in concerted proton–electron transfers. Electrochemistry of the 2,5–dicarboxylate 1,4–hydrobenzoquinone/2,5–dicarboxy 1,4–benzoquinone couple. *J. Am. Chem. Soc.*, 128(27):8726–8727, 2006. http://dx.doi.org/10.1021/ja0621750. 25

[30] C. Costentin, M. Robert, and J.-M. Savéant. Electrochemical and homogeneous proton–coupled electron transfers: Concerted pathways in the one–electron oxidation of a phenol coupled with an intramolecular amine–driven proton transfer. *J. Am. Chem. Soc.*, 128(14):4552–4553, 2006. http://dx.doi.org/10.1021/ja060527x. 25, 27

[31] Y. Umena, K. Kawakami, J.-R. Shen, and N. Kamiya. Crystal structure of oxygen–evolving photosystem II at a resolution of 1.9 Å. *Nature*, 473(7345):55–60, 2011. http://dx.doi.org/10.1038/nature09913. 26, 28

[32] C. J. T. de Grotthuss. Sur la décomposition de l'eau et des corps qu'elle tient en dissolution à l'aide de l'électricité galvanique. *Ann. Chim. (Paris)*, LVIII:54–74, 1806. 27

[33] S. Cukierman. Et tu, Grotthuss! And other unfinished stories. *BBA-Bioenergetics*, 1757(8):876–885, 2006. http://dx.doi.org/10.1016/j.bbabio.2005.12.001. 27

[34] C. Costentin, M. Robert, J.-M. Savéant, and C. Tard. Inserting a hydrogen–bond relay between proton exchanging sites in proton–coupled electron transfers. *Angew. Chem. Int. Ed.*, 49(22):3803–3806, 2010. http://dx.doi.org/10.1002/anie.200907192. 27, 29

[35] C. Costentin, M. Robert, J.-M. Savéant, and C. Tard. H–bond relays in proton–coupled electron transfers. oxidation of a phenol concerted with proton transport to a distal base through an OH relay. *Phys. Chem. Chem. Phys.*, 13(12):5353–5358, 2011. http://dx.doi.org/10.1039/C0CP02275F. 27

[36] B. Auer, L. E. Fernandez, and S. Hammes-Schiffer. Theoretical analysis of proton relays in electrochemical proton–coupled electron transfer. *J. Am. Chem. Soc.*, 133(21):8282–8292, 2011. http://dx.doi.org/10.1021/ja201560v. 30

[37] J.-M. Savéant. Electron transfer, bond breaking and bond formation. *Adv. Phys. Org. Chem.*, 35:117–192, 2000. http://dx.doi.org/10.1016/s0065-3160(00)35013-4. 30

[38] C. Costentin, V. Hajj, M. Robert, J.-M. Savéant, and C. Tard. Concerted heavy–atom bond cleavage and proton and electron transfers illustrated by proton–assisted reductive cleavage of an O–O bond. *Proc. Natl. Acad. Sci. U. S. A.*, 108(21):8559–8564, 2011. http://dx.doi.org/10.1073/pnas.1104952108. 31, 33

[39] C. Costentin, M. Robert, J.-M. Savéant, and C. Tard. Breaking bonds with electrons and protons. Models and examples. *Acc. Chem. Res.*, 47(1):271–280, 2014. http://dx.doi.org/10.1021/ar4001444. 31

[40] S. Antonello and F. Maran. Intramolecular dissociative electron transfer. *Chem. Soc. Rev.*, 34(5):418–428, 2005. http://dx.doi.org/10.1039/b300085k. 31

[41] C. Costentin, S. Drouet, G. Passard, M. Robert, and J.-M. Savánt. Proton–coupled electron transfer cleavage of heavy–atom bonds in electrocatalytic processes. Cleavage of a C–O bond in the catalyzed electrochemical reduction of CO_2. *J. Am. Chem. Soc.*, 135(24):9023–9031, 2013. http://dx.doi.org/10.1021/ja4030148. 33

[42] B. M. Hoffman, D. Lukoyanov, Z.-Y. Yang, D. R. Dean, and L. C. Seefeldt. Mechanism of nitrogen fixation by nitrogenase: The next stage. *Chem. Rev.*, 114(8):4041–4062, 2014. http://dx.doi.org/10.1021/cr400641x. 34, 41, 42

[43] J.-M. Savéant and C. Tard. Proton–coupled electron transfer in azobenzene–hydrazobenzene couples with pending acid–base functions. Hydrogen–bonding and structural effects. *J. Am. Chem. Soc.*, in press. 34

[44] J.-M. Savéant. Molecular catalysis of electrochemical reactions. Mechanistic aspects. *Chem. Rev.*, 108(7):2348–2378, 2008. http://dx.doi.org/10.1021/cr068079z. 35

[45] T. F. Jaramillo, K. P. Jørgensen, J. Bonde, J. H. Nielsen, S. Horch, and I. Chorkendorff. Identification of active edge sites for electrochemical H_2 evolution from MoS_2 nanocatalysts. *Science*, 317(5834):100–102, 2007. http://dx.doi.org/10.1126/science.1141483. 36

[46] D. Merki, S. Fierro, H. Vrubel, and X. Hu. Amorphous molybdenum sulfide films as catalysts for electrochemical hydrogen production in water. *Chem. Sci.*, 2(7):1262–1267, 2011. http://dx.doi.org/10.1039/C1SC00117E. 36

[47] D. Merki, H. Vrubel, L. Rovelli, S. Fierro, and X. Hu. Fe, Co, and Ni ions promote the catalytic activity of amorphous molybdenum sulfide films for hydrogen evolution. *Chem. Sci.*, 3(8):2515–2525, 2012. http://dx.doi.org/10.1039/C2SC20539D. 36, 37, 38

[48] H. I. Karunadasa, E. Montalvo, Y. Sun, M. Majda, J. R. Long, and C. J. Chang. A molecular MoS_2 edge site mimic for catalytic hydrogen generation. *Science*, 335(6069):698–702, 2012. http://dx.doi.org/10.1126/science.1215868. 36

[49] Y. Sun, C. Liu, D. C. Grauer, J. Yano, J. R. Long, P. Yang, and C. J. Chang. Electrodeposited cobalt–sulfide catalyst for electrochemical and photoelectrochemical hydrogen generation from water. *J. Am. Chem. Soc.*, 135(47):17699–17702, 2013. http://pubs.acs.org/doi/abs/10.1021/ja4094764. 36

[50] S. Cobo, J. Heidkamp, P.-A. Jacques, J. Fize, V. Fourmond, L. Guetaz, B. Jousselme, V. Ivanova, H. Dau, S. Palacin, M. Fontecave, and V. Artero. A Janus cobalt–based catalytic material for electro–splitting of water. *Nat. Mater.*, 11(9):802–807, 2012. http://dx.doi.org/10.1038/nmat3385. 36, 37, 38

[51] Y. Xu, R. Wu, J. Zhang, Y. Shi, and B. Zhang. Anion–exchange synthesis of nanoporous fep nanosheets as electrocatalysts for hydrogen evolution reaction. *Chem. Commun.*, 49(59):6656–6658, 2013. http://dx.doi.org/10.1039/C3CC43107J. 36

[52] E. J. Popczun, J. R. McKone, C. G. Read, A. J. Biacchi, A. M. Wiltrout, N. S. Lewis, and R. E. Schaak. Nanostructured nickel phosphide as an electrocatalyst for the hydrogen evolution reaction. *J. Am. Chem. Soc.*, 135(25):9267–9270, 2013. http://dx.doi.org/10.1021/ja403440e. 36

[53] W.-F. Chen, K. Sasaki, C. Ma, A. I. Frenkel, N. Marinkovic, J. T. Muckerman, Y. Zhu, and R. R. Adzic. Hydrogen–evolution catalysts based on non-noble metal nickel–molybdenum nitride nanosheets. *Angew. Chem. Int. Ed.*, 51(25):6131–6135, 2012. http://dx.doi.org/10.1002/anie.201200699. 36

[54] J. R. McKone, B. F. Sadtler, C. A. Werlang, N. S. Lewis, and H. B. Gray. Ni–Mo nanopowders for efficient electrochemical hydrogen evolution. *ACS Catal.*, 3(2):166–169, 2012. http://dx.doi.org/10.1021/cs300691m. 36

[55] D. Rickard and G. W. Luther. Chemistry of iron sulfides. *Chem. Rev.*, 107(2):514–562, 2007. http://dx.doi.org/10.1021/cr0503658. 36

[56] C. Di Giovanni, W.-A. Wang, S. Nowak, J.-M. Grenèche, H. Lecoq, L. Mouton, M. Giraud, and C. Tard. Bioinspired iron sulfide nanoparticles for cheap and long–lived electrocatalytic molecular hydrogen evolution in neutral water. *ACS Catal.*, 4(2):681–687, 2014. http://dx.doi.org/10.1021/cs4011698. 36, 38, 41

[57] C. Tard and M. Giraud. Iron sulfide based catalyst for electrolytic water reduction into hydrogen gas. Patent EP 13305888, 2013. 37, 41

[58] T. D. Kelly and G. R. Matos. Historical statistics for mineral and material commodities in the United States (2013 version). U.S. Geological Survey Data Series 140, accessed April 16, 2013, at http://minerals.usgs.gov/minerals/pubs/historical-statistics/. 37

[59] P. Agre and D. Kozono. Aquaporin water channels: Molecular mechanisms for human diseases. *FEBS Lett.*, 555(1):72–78, 2003. http://dx.doi.org/10.1016/S0014-5793(03)01083-4. 40

[60] C. A. Wraight. Chance and design–proton transfer in water, channels and bioenergetic proteins. *Biochim. Biophys. Acta, Bioenerg.*, 1757(8):886–912, 2006. http://dx.doi.org/10.1016/j.bbabio.2006.06.017. 40

[61] F. Yu, V. M. Cangelosi, M. L. Zastrow, M. Tegoni, J. S. Plegaria, A. G. Tebo, C. S. Mocny, L. Ruckthong, H. Qayyum, and V. L. Pecoraro. Protein design: Toward functional metalloenzymes. *Chem. Rev.*, 114(7):3495–3578, 2014. http://dx.doi.org/10.1021/cr400458x. 40

[62] M. Can, F. A. Armstrong, and S. W. Ragsdale. Structure, function, and mechanism of the nickel metalloenzymes, CO dehydrogenase, and acetyl-CoA synthase. *Chem. Rev.*, 114(8):4149–4174, 2014. http://dx.doi.org/10.1021/cr400461p. 41, 42

[63] D. K. Bediako, C. Costentin, E. C. Jones, D. G. Nocera, and J.-M. Savéant. Proton–electron transport and transfer in electrocatalytic films. Application to a cobalt–based O_2–evolution catalyst. *J. Am. Chem. Soc.*, 135(28):10492–10502, 2013. http://dx.doi.org/10.1021/ja403656w. 42

[64] D. G. Nocera. The artificial leaf. *Acc. Chem. Res.*, 45(5):767–776, 2012. http://dx.doi.org/10.1021/ar2003013. 43

[65] H. A. Macpherson and C. R. Stoldt. Iron pyrite nanocubes: Size and shape considerations for photovoltaic application. *ACS Nano*, 6(10):8940–8949, 2012. http://dx.doi.org/10.1021/nn3029502. 43

[66] Y.-C. Wang, D.-Y. Wang, Y.-T. Jiang, H.-A. Chen, C.-C. Chen, K.-C. Ho, H.-L. Chou, and C.-W. Chen. FeS_2 nanocrystal ink as a catalytic electrode for dye–sensitized solar cells. *Angew. Chem. Int. Ed.*, 52(26):6694–6698, 2013. http://dx.doi.org/10.1002/anie.201300401. 43

[67] D. Rickard and G. W. Luther. Chemistry of iron sulfides. *Chem. Rev.*, 107(2):514–562, 2007. http://dx.doi.org/10.1021/cr0503658. 43

[68] P. V. Kamat. Manipulation of charge transfer across semiconductor interface. A criterion that cannot be ignored in photocatalyst design. *J. Phys. Chem. Lett.*, 3(5):663–672, 2012. http://dx.doi.org/10.1021/jz201629p. 43

List of Figures

List of Acronyms

3SCC Three–stranded coiled coil

AFM atomic force microscopy

CC cluster centred

CPE controlled–potential electrolysis

CPET concerted proton–electron transfer

DET dissociative electron transfer

DFT density functional theory

EDX energy-dispersive X–ray

HE high energy band

KIE kinetic isotope effect

KTP Potassium titanyl phosphate $KTiOPO_4$

LE low energy band

MLCT metal–to–ligand charge transfer

MTEOS methyltriethoxysilane

OEC oxygen–evolving complex

PCET proton–coupled electron transfer

SCE saturated calomel electrode

SHG second–harmonic generation

SEM scanning electron microscopy

TEM transmission electron microscopy

TGA thermogravimetric analysis

XLCT halide–to–ligand charge transfer

XMCT halide–to–metal charge transfer

XPS X–ray photoelectron spectroscopy

XRD X–ray diffraction

Pcpent3 tricyclopentylphosphine

PPh2Pr diphenyl–propyl–phosphine

PPh3 triphenylphosphine

List of Symbols

ΔG°	standard free energy of reaction
$\Delta G^{\neq}$	standard activation free energy (intrinsic barrier)
E°	standard potential
F	Faraday constant
k	electron transfer rate constant
k_s	electron transfer rate constant at the electrode
λ	reorganisation energy
λ_0	solvent reorganisation energy
λ_0^{ET}	electron transfer reorganisation energy
λ_0^{PT}	proton transfer reorganisation energy
λ_i	internal reorganisation energy
M	molar mass
p	electron transfer probability
Q	charge passed in electrolysis
R	molar gas constant
S	electrode surface area
T	absolute temperature
χ	transmission coefficient
Z^{el}	electrochemical collision frequency

Selected Publications

1. C. Tard, X. M. Liu, S. K. Ibrahim, M. Bruschi, L. De Gioia, S. C. Davies, X. Yang, L. S. Wang, G. Sawers, and C. J. Pickett. Synthesis of the H–cluster framework of iron–only hydrogenase
Nature, **2005**, *433*, 610–613.
http://dx.doi.org/10.1038/nature03298

   In this paper, we intended to show that the synthesis of the free–standing active site of the [FeFe]–hydrogenase was feasible, and that we retained its catalytic properties towards proton reduction. This has been achieved by the preparation of an $[Fe_2S_2]$–unit that can be reacted with an asymmetrical $[Fe_4S_4]$–cluster to give a structurally relevant catalyst. Electrochemical studies, Mössbauer spectroscopy and X–ray absorption spectroscopic measurements as well as DFT calculations allowed us to characterise this assembly and extract a mechanism for hydrogen evolution.

2. M. H. Cheah, C. Tard, S. J. Borg, X. M. Liu, S. K. Ibrahim, C. J. Pickett, and S. P. Best. Modeling [Fe–Fe] hydrogenase: evidence for bridging carbonyl and distal iron coordination vacancy in an electrocatalytically competent proton reduction by an iron thiolate assembly that operates through Fe(0)–Fe(II) levels
J. Am. Chem. Soc., **2007**, *129*, 11085–11092.
http://dx.doi.org/10.1021/ja071331f

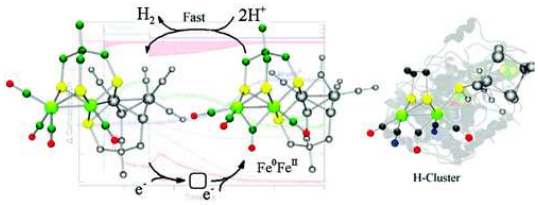

   This article underlines the role of the bridging / terminal carbonyl ligands in a structurally and electronically model complex of the [FeFe]–hydrogenase. Supported by DFT calculations, the electrochemical study presents the different mechanistic paths for hydrogen evolution, and stresses the difference in the rate of reaction between

Fe(I) and Fe(II) states.

3. C. Tard, S. Perruchas, S. Maron, X. F. Le Goff, F. Guillen, A. Garcia, J. Vigneron, A. Etcheberry, T. Gacoin, and J.–P. Boilot. Thermochromic luminescence of sol–gel films based on copper iodide clusters
Chem. Mater., **2008**, *20*, 7010–7016.
http://dx.doi.org/10.1021/cm801780g

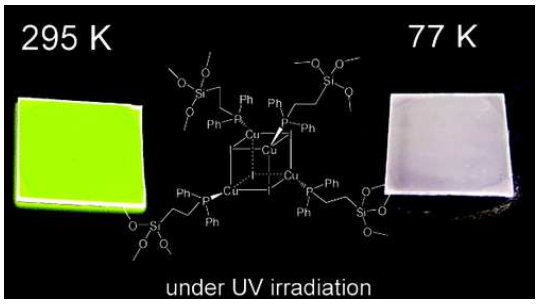

This study presents the preparation of a copper iodide cluster and its incorporation within a sol–gel matrix. The solid–state NMR and fluorescent measurements confirmed the stability of such material and that the thermochromic luminescent properties were preserved from 8 K to ambient temperature.

4. C. Costentin, M. Robert, J.–M. Savéant, and C. Tard. Inserting a hydrogen–bond relay between proton exchanging sites in proton–coupled electron transfers
Angew. Chem. Int. Ed., **2010**, *49*, 3803–3806.
http://dx.doi.org/10.1002/anie.200907192

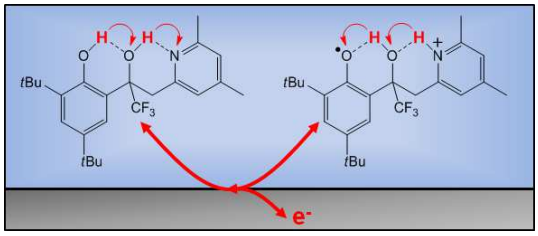

This publication shows that the introduction of a hydrogen bonding group between two electron and proton exchanging sites offers an efficient route for proton movement over distances as large as 4.3 Å by means of the translocation of two protons in a concerted manner with electron transfer.

5. C. Di Giovanni, W.–A. Wang, S. Nowak, J.–M. Grenèche, H. Lecoq, L. Mouton, M. Giraud, and C. Tard. Bioinspired iron sulfide nanoparticles for cheap and long–lived electrocatalytic molecular hydrogen evolution in neutral water
ACS Catal., **2014**, *4*, 681–687.
http://dx.doi.org/10.1021/cs4011698

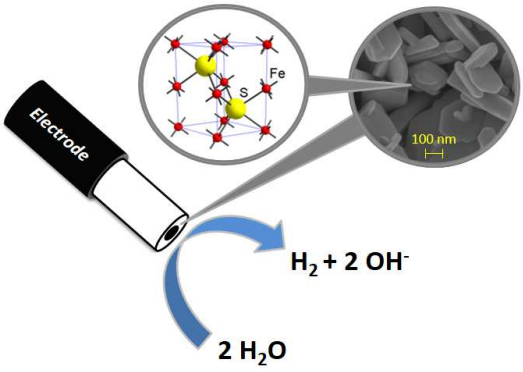

This investigation demonstrates the ability of iron sulphide nanoparticles to catalyse the evolution of hydrogen from water. Robustness and cheapness of the material was asserted, as the catalysis showed no sign of weakening after six day of electrolysis.

like the incommensurate phase of $Pr_{1/2}Ca_{1/2}MnO_3$, where strong ferromagnetic fluctuations have been measured[14,26], rather than the long-range magnetic order we would predict. Second, in order to keep the calculations tractable, the phase transitions at T_C and T_{CO} have been forced to be continuous. This explains why the re-entrant magnetism above T_L shown in Fig. 2 appears only when $T_C > T_{CO}$. If this theory were generalized to include discontinuous phase transitions, this condition would relax. Another consequence of assuming continuous-phase transitions is that phase separation cannot be predicted. In real systems, phase separation is possible because strain[3,9], or disorder[8], can make more-or-less localized phases dominate within a given region. Orbital ordering is described by a vector order parameter, and thus our simple model cannot address the complexity of different orbitally ordered phases that have been proposed[12].

The Ginzburg–Landau phenomenology we propose is capable of systematizing some puzzling data for manganites near $x = 1/2$, but of course the propensity for mixed and homogeneous phases is driven by the underlying physical parameters that make the energetic cost of spatial fluctuations low. This 'electronic softness' means that as well as spatially disordered 'phase separation', we find new ordered phases which are long-period arrangements of the two competing orders. Indeed, it may be that this potential for textured electronic phases is a hallmark of electronic oxides near the Mott transition[29], seen perhaps in the coexistence of density waves and superconductivity in the copper oxides[30]. □

Received 29 July; accepted 17 December 2004; doi:10.1038/nature03300.

1. Tokura, Y. (ed.) *Colossal Magnetoresistance Oxides* (Gordon and Breach, New York, 2000).
2. Mathur, N. D. & Littlewood, P. B. Mesoscopic textures in manganites. *Phys. Today* **56,** 25–30 (2003).
3. Mathur, N. D. & Littlewood, P. B. The self-organised phases of manganites. *Sol. Stat. Commun.* **119,** 271–280 (2001).
4. Dagotto, E. *Nanoscale Phase Separation and Colossal Magnetoresistance* (Springer Series in Solid State Sciences Vol. 136, Springer, 2002).
5. Uehara, M., Mori, S., Chen, C. H. & Cheong, S.-W. Percolative phase separation underlies colossal magnetoresistance in mixed-valence manganites. *Nature* **399,** 560–563 (1999).
6. Loudon, J. C., Mathur, N. D. & Midgley, P. A. Charge-ordered ferromagnetic phase in $La_{0.5}Ca_{0.5}MnO_3$. *Nature* **420,** 797–800 (2002).
7. Chen, C. H. & Cheong, S.-W. Commensurate to incommensurate charge ordering and its real-space images in $La_{0.5}Ca_{0.5}MnO_3$. *Phys. Rev. Lett.* **76,** 4042–4045 (1996).
8. Burgy, J., Moreo, A. & Dagotto, E. Relevance of cooperative lattice effects and correlated disorder in phase separation theories for CMR manganites. *Phys. Rev. Lett.* **92,** 097202 (2004).
9. Ahn, K. H., Lookman, T. & Bishop, A. R. Strain-induced metal–insulator phase coexistence in perovskite manganites. *Nature* **428,** 401–404 (2004).
10. Goodenough, J. Theory of the role of covalence in the perovskite-type manganites [La, M(II)]MnO_3. *Phys. Rev* **100,** 564–573 (1955).
11. Herrero-Martín, J., García, J., Subías, G., Blasco, J. & Sánchez, M. C. Structural origin of dipole x-ray resonant scattering in the low-temperature phase of $Nd_{0.5}Sr_{0.5}MnO_3$. *Phys. Rev. B* **70,** 024408 (2004).
12. Brey, L. Continuous charge modulated diagonal phase in manganites. *Phys. Rev. Lett.* **92,** 127202 (2004).
13. Coey, M. Charge ordering in oxides. *Nature* **430,** 155–156 (2004).
14. Kajimoto, R., Yoshizawa, H., Tomioka, Y. & Tokura, Y. Commensurate-incommensurate transition in the melting process of orbital ordering in $Pr_{0.5}Ca_{0.5}MnO_3$: A neutron diffraction study. *Phys. Rev. B* **63,** 212407 (2001).
15. Zimmermann, M. v. *et al.* X-ray resonant scattering studies of orbital and charge ordering in $Pr_{1-x}Ca_xMnO_3$. *Phys. Rev. B* **64,** 195133 (2001).
16. Larochelle, S. *et al.* Nature of e_g electron order in $La_{1-x}Sr_{1+x}MnO_4$. *Phys. Rev. Lett.* **87,** 095502 (2001).
17. Jirak, Z., Krupicka, S., Simsa, Z., Dlouham, M. & Vratislav, S. Neutron diffraction study of $Pr_{1-x}Ca_xMnO_3$ perovskites. *J. Magn. Magn. Mater.* **53,** 153–166 (1985).
18. Chen, C. H., Cheong, S.-W. & Hwang, H. Y. Charge ordered stripes in $La_{1-x}Ca_xMnO_3$. *J. Appl. Phys.* **81,** 4326–4330 (1997).
19. Chen, C. H., Mori, S. & Cheong, S.-W. Anomalous melting transition of the charge ordered state in manganites. *Phys. Rev. Lett.* **83,** 4792–4795 (1999).
20. Loudon, J. C. *et al.* Weak charge-lattice coupling requires reinterpretation of stripes of charge order in (La, Ca)MnO_3. Preprint at ⟨http://www.arXiv.org/cond-mat/0308581⟩ (2003).
21. Schiffer, P., Ramirez, A. P., Bao, W. & Cheong, S.-W. Low temperature magnetoresistance and the magnetic phase diagram of $La_{1-x}Ca_xMnO_3$. *Phys. Rev. Lett.* **75,** 3336–3339 (1995).
22. Yoshizawa, H., Kawano, H., Tomioka, Y. & Tokura, Y. Neutron diffraction study of the magnetic-field-induced metal-insulator transition in $Pr_{0.7}Ca_{0.3}MnO_3$. *Phys. Rev. B* **52,** R13145–R13148 (1995).
23. Tolèdano, J. C. & Tolèdano, P. *The Landau Theory of Phase Transitions* Ch. 5 (World Scientific, Singapore, 1987).
24. Murakami, S. & Nagaosa, N. Colossal magnetoresistance in manganites as multicritical phenomena. *Phys. Rev. Lett.* **90,** 197201 (2003).
25. Yamada, Y. & Takakura, T. Incommensurate orbital order and two-phase coexistence in doped manganites at metal-insulator phase boundary. *J. Phys. Soc. Jpn* **71,** 2480–2484 (2002).
26. Kajimoto, R. *et al.* Anomalous ferromagnetic spin fluctuations in an antiferromagnetic insulator $Pr_{1-x}Ca_xMnO_3$. *Phys. Rev. B* **58,** R11837–R11840 (1998).
27. Mathur, N. D. *et al.* Resistance of a domain wall in $La_{0.7}Ca_{0.3}MnO_3$. *J. Appl. Phys.* **86,** 6287–6290 (1999).
28. Rzchowski, M. S. & Joynt, R. Electronic inhomogeneity at magnetic domain walls in strongly-correlated systems. *Europhys. Lett.* **67,** 287–293 (2004).
29. Kivelson, S. A., Fradkin, E. & Emery, V. J. Electronic liquid-crystal phases of a doped Mott insulator. *Nature* **393,** 550–553 (1998).
30. McElroy, K. *et al.* Homogenous nodal superconductivity coexisting with inhomogeneous charge order in strongly underdoped Bi-2212. Preprint at ⟨http://www.arXiv.org/cond-mat/0404005⟩ (2004).

Supplementary Information accompanies the paper on **www.nature.com/nature**.

Acknowledgements We thank L. Brey and N. Mathur for discussions. P.B.L. thanks the National High Magnetic Field Laboratory of the Los Alamos National Laboratory for hospitality. M.J.C. acknowledges Churchill College, University of Cambridge, for the award of a JRF. This work was supported by the EPSRC and through the EPSRC Magnetic Oxide Network.

Competing interests statement The authors declare that they have no competing financial interests.

Correspondence and requests for materials should be addressed to G.C.M. (gcm24@cam.ac.uk).

Synthesis of the H-cluster framework of iron-only hydrogenase

Cédric Tard[1], Xiaoming Liu[1], Saad K. Ibrahim[1], Maurizio Bruschi[3], Luca De Gioia[3], Siân C. Davies[1], Xin Yang[4], Lai-Sheng Wang[4], Gary Sawers[2] & Christopher J. Pickett[1]

[1]*Department of Biological Chemistry,* [2]*Department of Molecular Microbiology, John Innes Centre, Norwich NR4 7UH, UK*
[3]*Department of Biotechnology and Biosciences, University of Milano-Bicocca, Piazza della Scienza 2, 20126-Milan, Italy*
[4]*Department of Physics, Washington State University, 2710 University Drive, Richland, and WR Wiley Environmental Science Laboratory and Chemical Sciences Division, Pacific Northwest National Laboratory, PO Box 999, MS K8-88, Richland, Washington 99352, USA*

The metal-sulphur active sites of hydrogenases catalyse hydrogen evolution or uptake at rapid rates. Understanding the structure and function of these active sites—through mechanistic studies of hydrogenases[1–4], synthetic assemblies[5–12] and *in silico* models[13–15]—will help guide the design of new materials for hydrogen production or uptake[16]. Here we report the assembly of the iron-sulphur framework of the active site of iron-only hydrogenase (the H-cluster), and show that it functions as an electrocatalyst for proton reduction. Through linking of a di-iron subsite to a {4Fe4S} cluster, we achieve the first synthesis of a metallosulphur cluster core involved in small-molecule catalysis. In addition to advancing our understanding of the natural biological system, the availability of an active, free-standing analogue of the H-cluster may enable us to develop useful electrocatalytic materials for application in, for example, reversible hydrogen fuel cells. (Platinum is currently the preferred electrocatalyst for such applications, but is expensive, limited in availability and, in the long term, unsustainable[17].)

The crystallographic characterization of Fe-only hydrogenases[1,2] has revealed a striking resemblance of the di-iron subsite of the H-cluster to known $[Fe_2(\mu\text{-}SR)_2(CO)_6]$ (R = organic group) complexes. This type of assembly, first discovered[18] more than 70 years ago, opened the way for the synthesis of {2Fe2S}- and {2Fe3S}-complexes with key structural and/or spectroscopic features of this biologically unprecedented—low-valent, carbon monoxide- and cyanide-coordinated—di-iron unit (Fig. 1). A major challenge is now to build a free-standing analogue of the entire H-cluster, as this offers the prospects of understanding the interplay of the conjoined di-iron and cubane units that form the enzymic catalytic machinery

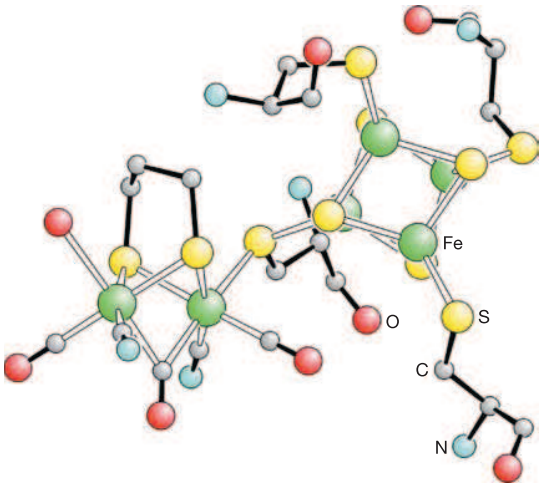

Figure 1 Composite structure of the H-cluster. This was constructed from the crystal structures of Fe-only hydrogenase isolated from *Desulfovibrio desulfuricans* (Protein Data Bank Code 1HFE)[2] and *Clostridium pasteurianum* (Protein Data Bank Code 1FEH)[1], and FTIR data from *Desulfovibrio vulgaris*. The apical group on the sub-site ligand may possibly be an NH, but this remains crystallographically and analytically unresolved.

and of the development of new catalytic materials.

The dithiolate ligand **A**, which possesses an appended thioester group, was synthesized as outlined in Fig. 2. **A** reacts with $Fe_3(CO)_{12}$ to give the thioester activated di-iron subsite analogue, **B**. Unlike dithiolate thioether ligands with the same tripodal carbon backbone[19], the thioester sulphur does not displace CO and coordinate to an Fe atom of the di-iron unit, as shown in the X-ray crystallographic structure (Supplementary Fig. 1). Undoubtedly this is because the electron-withdrawing acyl group lowers the nucleophilicity of the S atom to which it is attached.

The cubane cluster $[Fe_4S_4(L)(SEt)]^{2-}$ (L = 1,3,5-tris (4,6-dimethyl-3-mercaptophenylthio)-2,4,6-tris (*p*-tolyl-thio)benzene), denoted **C**, which has three of the cubane iron atoms blocked by the chelating ligand, was synthesized by an established procedure[20]. **C** reacts cleanly with one equivalent of **B** over a 12 h period at room temperature to give, after work-up, analytically pure $[Fe_4S_4(L)_3\{Fe_2(CH_3C(CH_2S)_3)(CO)_5\}][NBu_4]_2$, **D** (Fig. 2). Negative ion electrospray mass spectrometry (ESMS; MeCN) on **D** showed peaks centred at mass/charge (m/z) = 856.9 (100%) for the dianion and at m/z = 1,957.1 (10%) for $\{[Fe_4S_4(L)_3\{Fe_2(CH_3C(CH_2S)_3)(CO)_5\}]^{2-}[NBu_4]^+\}$, with respective isotopic distribution patterns consistent with doubly and singly charged species. Fourier transform infrared (FTIR) ν(CO) bands for **D** at 2,035(medium, m), 1,970(strong, s) and 1,912(weak, w) cm^{-1} are very similar to those of $[Fe_2(CH_3C(CH_2S)_2(CH_2SCH_3))(CO)_5]$ (2,049(m), 1,983(s) and 1,927(w) cm^{-1}) in which the thioether ligand is known to be coordinated to one Fe atom[19]. Thus the reaction between **B** and **C** proceeds beyond elimination of MeCOSEt—carbon monoxide is lost from the proximal Fe atom of the di-iron unit, and results in the formation of a $\{Fe_{cubane}(\mu\text{-}SR)Fe_{subsite}\}$ linkage as found in the H-cluster (Fig. 3). This is supported by the solid state Mössbauer spectrum of **D** at 80 K, which exhibits four overlapping quadrupole split doublets with isomer shift (i.s.) and quadrupole splitting (q.s.) parameters (in $mm\,s^{-1}$) consistent with four differentiated iron sites; two associated with the site-differentiated cubane (i.s. = 0.47, q.s. = 1.14; i.s. = 0.45, q.s. = 0.87) and two with the di-iron subsite (i.s. = 0.04, q.s. = 1.00 (Fe distal to cubane); i.s. = 0.04, q.s. = 0.50 (Fe proximal to cubane))[19].

Full geometry optimization of an *in silico* model of **D**, $[Fe_4S_4(SCH_3)_3\{Fe_2(CH_3C(CH_2S)_3)(CO)_5\}]^{2-}$, was carried out in the density functional theory (DFT) framework using the BP86 pure functional[21,22] and an all-electron valence triple-ζ basis set with polarization functions on all atoms (TZVP)[23]. This resulted in a structure fully consistent with that proposed on the basis of experimental data for **D** (Fig. 3). In particular, one of the thiolate groups bridges almost symmetrically the {4Fe4S} and the {2Fe2S} units, with an Fe–Fe distance (2.6 Å) in the binuclear cluster that is indicative of a metal–metal bond. Analysis of the electronic properties of the *in silico* structure reveals that the redox state of the binuclear moiety can be described as Fe(I)Fe(I).

The $\{Fe_{cubane}(\mu\text{-}SR)Fe_{subsite}\}$ linkage provides substantial electronic communication between the di-iron centre and the {4Fe4S} cubane centre, as is evident from the following spectroscopic and electrochemical measurements. Formally replacing the Me of the thioether ligand in $[Fe_2(CH_3C(CH_2S)_2(CH_2SCH_3))(CO)_5]$ by the cubane dianion shifts all the ν(CO) frequencies of the appended subsite by ~15 cm^{-1} to lower values: the $\{Fe_4S_4(L)\}^{2-}$-core is a 'better' donor group than is methyl. The inductive influence of the cubane in lowering ν(CO) is reciprocated in the shift of the redox

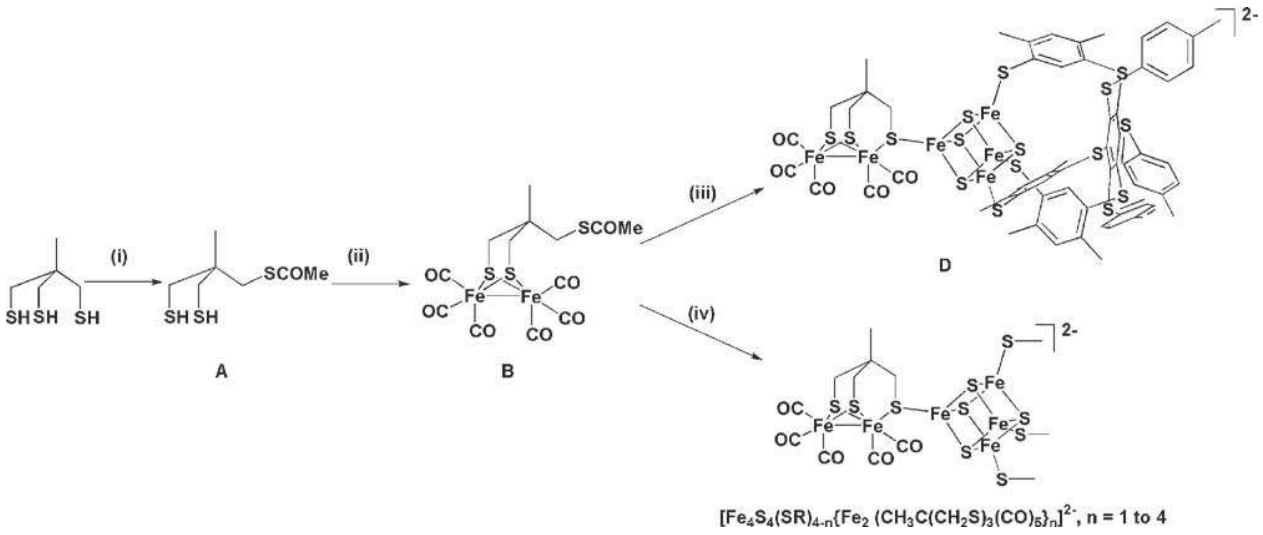

Figure 2 Synthetic pathways for assembly of the H-cluster model and related subsite-cluster materials. Reaction steps are as follows: (i) acetic anhydride, $NaHCO_3$, diethyl ether, (ii) $Fe_3(CO)_{12}$, toluene, (iii) **C**, MeCN, (iv) $[Fe_4S_4(SEt)_4][NBu_4]_2$, MeCN.

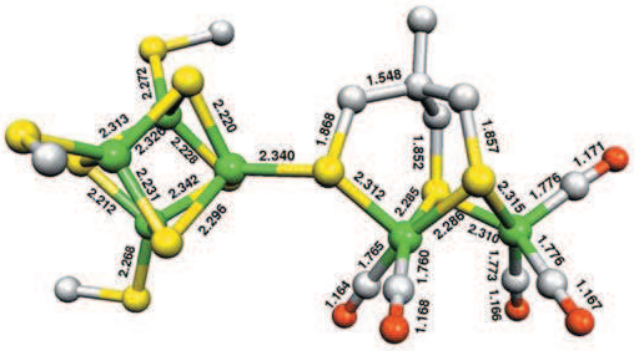

Figure 3 Structure of $[Fe_4S_4(SCH_3)_3\{Fe_2(CH_3C(CH_2S)_3)(CO)_5\}]^{2-}$, derived from DFT calculations. Numbers show bond lengths in Å.

potential for the reduction of the cubane core to more positive potentials. The primary reversible one-electron reduction of **D** (0.1 M $[NBu_4][BF_4]$-MeCN, cyclic voltammetry, sweep rate 100 mV s^{-1}) occurs at $E_{1/2} = -0.86$ V versus (Ag/AgCl, CH_2Cl_2, 0.45 M $[NBu_4][BF_4]$, 0.05 M $[NBu_4]Cl$); that for the parent cluster $[Fe_4S_4(L)(SEt)]^{2-}$ is at $E_{1/2} = -0.98$ V under identical conditions. The $\Delta E_{1/2}$ for the formal replacement of EtS by $\{Fe_2(CH_3C(CH_2S)_3)(CO)_5\}$ of +120 mV shows that the energy of the cubane lowest unoccupied molecular orbital (LUMO) is substantially lowered.

Gas-phase photoelectron spectroscopy (PES)[24,25] of isolated $[Fe_4S_4(SEt)_3\{Fe_2(CH_3C(CH_2S)_3)(CO)_5\}]^{2-}$ is concordant with this. The PES of this anion at an excitation wavelength of 355 nm revealed two low-binding-energy spectral features that are very similar to the first two bands of $[Fe_4S_4(SEt)_4]^{2-}$ but shifted by about 0.6 eV to higher energy (adiabatic electron detachment energy increases from 0.29 to 0.89 eV (ref. 26); Supplementary Fig. 2). Thus on replacing EtS by the subsite unit the highest-energy orbitals remain localized on the cubane core but are substantially stabilized. At 266 and 193 nm, higher-energy spectral features associated with the attached subsite are also observed that are absent in the parent dianion, $[Fe_4S_4(SEt)_4]^{2-}$.

Complete substitution of the {4Fe4S}-core by di-iron units is possible (Fig. 2, step (iv)). The reaction of $[Fe_4S_4(SEt)_4][NBu_4]_2$ (MeCN, room temperature, 12 h) with an excess of **B** followed by work-up and ESMS shows formation of a dianion with *m/z* centred at 1,009.6 (100%) and an isotopic pattern corresponding to the dianion $[Fe_4S_4\{Fe_2(CH_3C(CH_2S)_3)(CO)_5\}_4]^{2-}$, **E**. Cyclic voltammetry of **E** (vitreous carbon electrode, 100 mV s^{-1}, room temperature, 0.1 M $[NBu_4][BF_4]$-CH_2Cl_2) shows a primary reversible one-electron reduction couple at −0.65 V versus (Ag/AgCl, CH_2Cl_2, 0.45 M $[NBu_4][BF_4]$, 0.05 M $[NBu_4]Cl$) corresponding to the reduction of the $\{4Fe4S\}^{2+}$ core, and a multi-electron reduction at −1.58 V which encompasses the irreversible reduction of the subsite units. The primary reversible reduction of $[Fe_4S_4(SEt)_4]^{2-}$ occurs at −1.15 V under the same conditions, attesting to the strong electron-withdrawing properties of the μ-S ligated di-iron subsites. The ΔE of +500 mV for replacement of the four EtS ligands by four subsite ligands (that is, an average of 125 mV per substitution) fits very well with the 120 mV shift observed on replacing the single EtS with the di-iron subsite to give **D**.

Beyond inductive effects transmitted through the $\{2Fe2S\}(\mu\text{-}SCH_2R)\{4Fe4S\}$ framework, there is evidence for an interplay of redox states that transcends the behaviour of the isolated component di-iron and the cubane centre. Repetitive cyclic voltammetry of **D** over 10 cycles shows the build-up of a reversible system at −0.96 V versus (Ag/AgCl, CH_2Cl_2, 0.45 M $[NBu_4][BF_4]$, 0.05 M $[NBu_4]Cl$) (Fig. 4a and Supplementary Fig. 3 (process II)). The voltammogram can be reasonably simulated by a mechanism that involves intramolecular electron transfer between the reduced cluster and subsite in concert with reversible opening of the μ-SCH_2 bridge. This leaves the cubane linked to the subsite by an alkylthiolate in a $\{4Fe4S\}^{2+}$ state and therefore susceptible to further reduction. This would be expected to take place at a potential close to that observed for the alkylthiolate ligated $[Fe_4S_4(L)(SEt)]^{2-}$, as is observed (Supplementary Fig. 4 and Supplementary Text).

Studies[11,27] have shown that simple subsite models are capable of electrocatalysing proton reduction and H/D exchange reactions, albeit at low reduction potentials[12,28]. Figure 4b shows that the H-cluster analogue **D** electrocatalyses proton reduction at a diffusion-controlled rate. The current–potential curve for the reduction of protons in the presence of the catalyst (E_p=−1.13 V) is displaced by ~200 mV positive from that measured in the absence of the catalyst ($E_p = -1.33$ V versus (Ag/AgCl, CH_2Cl_2, 0.45 M $[NBu_4][BF_4]$, 0.05 M $[NBu_4]Cl$)).

The μ-S cysteinyl bridge identified in the enzyme structures[1,2] must provide substantial electronic communication between the subsite and the {4Fe4S}-cubane, because we have shown for **D** that these units do not behave as insulated redox entities. The Mössbauer parameters for **D** corrected for the second order Doppler effect to 4.2 K (site differentiated cubane: i.s. = 0.50, 0.48, q.s. = 0.87, 1.14; di-iron subsite: i.s. = 0.07,0.07 q.s. = 0.50, 1.00 mm s^{-1}) are similar to those attributed to these components in the reduced state of *Clostridium pasteurianum* hydrogenase II (site differentiated

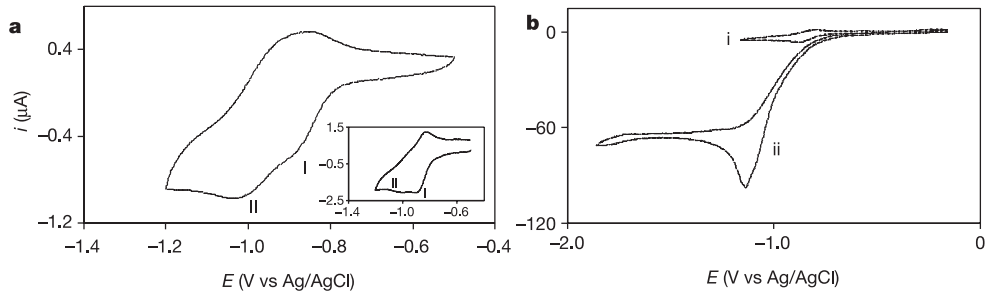

Figure 4 The electrochemical behaviour of the synthetic H-cluster model. **a**, Cyclic voltammogram of **D** (0.1 M $[NBu_4][BF_4]$-MeCN, 30 mV s^{-1}, vitreous carbon), showing interconverting redox processes I and II. $E_{1/2}$ for II occurs at a potential close to that for **C**, indicative of the rearrangement of the μ-S bonded subsite to the terminal alkylthiolate. Inset, first-scan response at the faster scan rate of 0.1 V s^{-1} but otherwise under the same conditions; note suppression of the interconversion. **b**, Cyclic voltammogram of **D** (1.5 mM), showing the electrocatalytic response in the absence (trace i) and in the presence (trace ii) of 4,6-dimethyl pyridinium cation as a source of protons (15 mM) at a normalized scan rate of 0.1 V s^{-1}. The peak current for proton reduction in the absence of the catalyst is within 5% of that in its presence, but is shifted about 200 mV to a more negative potential.

cubane: i.s. = 0.47, 0.47, q.s. = 0.85, 1.35; di-iron subsite: i.s. = 0.08, q.s. = 0.87 mm s^{-1}) measured at 4.2 K. This is concordant with the generally accepted re-assignment of the electronic structure of the six-iron core of the reduced biological cluster as $[\{Fe(I).Fe(I)\}_{subsite}\text{-}\{4Fe4S\}^{2+}_{cubane}]$[29], the established redox configuration of our synthetic cluster. In the synthetic system, we have seen that the reduction of the cubane unit by one electron to the $\{4Fe4S\}^{+}$ level is easier than is reduction of the $\{Fe(I).Fe(I)\}_{subsite}$, which is coordinatively saturated with a closed-shell (36-electron) configuration. A corresponding state of the H-cluster, in which the cubane unit is reduced to the $\{4Fe4S\}^{+}$ level, has yet to be detected, although neighbouring {4Fe4S} relay centres in *C. pasteurianum* hydrogenase II can be reduced to this level[29]. This raises the question as to whether the $\{4Fe4S\}^{+}$ level of the H-cluster is physiologically accessed during turnover. A vacant or (weakly) water-coordinated site has been identified crystallographically in the enzyme at the distal iron atom in the resting state of the enzyme. It is possible that protonation at this site lowers the energy of the Fe(I)·Fe(I) subsite unit sufficiently to enable its reduction by the anchored cubane operating at the $\{4Fe4S\}^{2+}$ level. That **D** is capable of electrocatalysing proton reduction may be similarly linked to the formation of a vacant site, in this case by the opening of the μ-S bridge on reduction.

The artificial H-clusters reported here should enhance our understanding of the intimate chemistry of the natural process, and lead to systems with low overpotentials for hydrogen uptake/evolution[11,28]. Given that redox-active $\{4Fe4S\}^{2+}$-centres can be incorporated at high concentration into cysteine functionalized electropolymers[30], we can envisage their modification, using the chemistry we have described, thereby providing a route to advanced electrode materials. □

Received 14 October; accepted 14 December 2004; doi:10.1038/nature03298.

1. Peters, J. W., Lanzilotta, W. N., Lemon, B. J. & Seefeldt, L. C. X-ray crystal structure of the Fe-only hydrogenase (Cpl) from *Clostridium pasteurianum* to 1.8 angstrom resolution. *Science* **282,** 1853–1858 (1998).
2. Nicolet, Y., Piras, C., Legrand, P., Hatchikian, C. E. & Fontecilla-Camps, J. C. *Desulfovibrio desulfuricans* iron hydrogenase: the structure shows unusual coordination to an active site Fe binuclear center. *Struct. Fold. Des.* **7,** 13–23 (1999).
3. Nicolet, Y., Lemon, B. J., Fontecilla-Camps, J. C. & Peters, J. W. A novel FeS cluster in Fe-only hydrogenases. *Trends Biochem. Sci.* **25,** 138–143 (2000).
4. Armstrong, F. A. Hydrogenases: active site puzzles and progress. *Curr. Opin. Chem. Biol.* **8,** 133–140 (2004).
5. Evans, D. J. & Pickett, C. J. Chemistry and the hydrogenases. *Chem. Soc. Rev.* **32,** 268–275 (2003).
6. Lyon, E. J., Georgakaki, I. P., Reibenspies, J. H. & Darensbourg, M. Y. Carbon monoxide and cyanide ligands in a classical organometallic complex model for Fe-only hydrogenase. *Angew. Chem. Int. Edn* **38,** 3178–3180 (1999).
7. Schmidt, M., Contakes, S. M. & Rauchfuss, T. B. First generation analogues of the binuclear site in the Fe-only hydrogenases: $Fe_2(\mu\text{-}SR)_2(CO)_4(CN)_2^{2-}$. *J. Am. Chem. Soc.* **121,** 9736–9737 (1999).
8. Le Cloirec, A. *et al.* A di-iron dithiolate possessing structural elements of the carbonyl/cyanide sub-site of the H-centre of Fe-only hydrogenase. *Chem. Commun.* 2285–2286 (1999).
9. Razavet, M. *et al.* Transient FTIR spectroelectrochemical and stopped-flow detection of a mixed valence {Fe(I)-Fe(II)} bridging carbonyl intermediate with structural elements and spectroscopic characteristics of the di-iron sub-site of all-iron hydrogenase. *Chem. Commun.* 700–701 (2002).
10. George, S. J., Cui, Z., Razavet, M. & Pickett, C. J. The di-iron subsite of all-iron hydrogenase: Mechanism of cyanation of a synthetic {2Fe3S} – carbonyl assembly. *Chem. Eur. J.* **8,** 4037–4046 (2002).
11. Gloaguen, F., Lawrence, J. D., Rauchfuss, T. B., Benard, M. & Rohmer, M. M. Bimetallic carbonyl thiolates as functional models for Fe-only hydrogenases. *Inorg. Chem.* **41,** 6573–6582 (2002).
12. Ott, S., Kritikos, M., Akermark, B., Sun, L. C. & Lomoth, R. A biomimetic pathway for hydrogen evolution from a model of the iron hydrogenase active site. *Angew. Chem. Int. Edn* **43,** 1006–1009 (2004).
13. Cao, Z. X. & Hall, M. B. Modeling the active sites in metalloenzymes. 3. Density functional calculations on models for Fe-hydrogenase: Structures and vibrational frequencies of the observed redox forms and the reaction mechanism at the diiron active center. *J. Am. Chem. Soc.* **123,** 3734–3742 (2001).
14. Liu, Z. P. & Hu, P. A density functional theory study on the active center of Fe-only hydrogenase: Characterization and electronic structure of the redox states. *J. Am. Chem. Soc.* **124,** 5175–5182 (2002).
15. Bruschi, M., Fantucci, P. & De Gioia, L. Density functional theory investigation of the active site of Fe-hydrogenases. Systematic study of the effects of redox state and ligands hardness on structural and electronic properties of complexes related to the $[2Fe]_H$ subcluster. *Inorg. Chem.* **43,** 3733–3741 (2004).
16. *Basic Research Needs for the Hydrogen Economy* (Report of the Basic Energy Sciences Workshop on Hydrogen Production, Storage, and Use, 13–15 May 2003, Office of Science, US Department of Energy); available at ⟨http://www.eere.energy.gov/hydrogenandfuelcells/pdfs/bes_project.pdf⟩.
17. *Platinum and Hydrogen for Fuel Cell Vehicles* (UK Department for Transport, September 2003); available at ⟨http://www.dft.gov.uk/stellent/groups/dft_roads/documents/page/dft_roads_024056.hcsp⟩.
18. Reihlen, H., Gruhl, A. & Hessling, G. Über den photochemischen und oxydativen Abbau von Carbonylen. *Liebigs Ann. Chem.* **472,** 268–287 (1929).
19. Razavet, M. *et al.* All-iron hydrogenase: synthesis, structure and properties of {2Fe3S}-assemblies related to the di-iron sub-site of the H-cluster. *Dalton Trans.* 586–595 (2003).
20. Stack, T. D. P. & Holm, R. H. Subsite-specific functionalization of the $[4Fe\text{-}4S]^{2+}$ analog of iron sulfur protein clusters. *J. Am. Chem. Soc.* **109,** 2546–2547 (1987).
21. Perdew, J. P. Density-functional approximation for the correlation-energy of the inhomogeneous electron-gas. *Phys. Rev. B* **33,** 8822–8824 (1986).
22. Becke, A. D. Density-functional exchange-energy approximation with correct asymptotic-behavior. *Phys. Rev. A.* **38,** 3098–3100 (1988).
23. Schafer, A., Huber, C. & Ahlrichs, R. Fully optimized contracted Gaussian-basis sets of triple zeta valence quality for atoms Li to Kr. *J. Chem. Phys.* **100,** 5829–5835 (1994).
24. Wang, L. S., Ding, C. F., Wang, X. B. & Barlow, S. E. Photodetachment photoelectron spectroscopy of multiply charged anions using electrospray ionization. *Rev. Sci. Instrum.* **70,** 1957–1966 (1999).
25. Yang, X., Razavet, M., Wang, X. B., Pickett, C. J. & Wang, L. S. Probing the electronic structure of the di-iron subsite of Fe-hydrogenase: A photoelectron spectroscopic study of Fe(I)-Fe(I) model complexes. *J. Phys. Chem. A* **107,** 4612–4618 (2003).
26. Wang, X. B. *et al.* Probing the intrinsic electronic structure of the cubane [4Fe4S] cluster: Nature's favorite cluster for electron transfer and storage. *J. Am. Chem. Soc.* **125,** 14072–14081 (2003).
27. Zhao, X. *et al.* Catalysis of H_2/D_2 scrambling and other H/D exchange processes by [Fe]-hydrogenase model complexes. *Inorg. Chem.* **41,** 3917–3928 (2002).
28. Tard, C., Liu, X., Hughes, D. L. & Pickett, C. J. A novel $\{Fe^{I}\text{-}Fe^{II}\text{-}Fe^{II}\text{-}Fe^{I}\}$ iron thiolate carbonyl assembly which electrocatalyses hydrogen evolution. *Chem. Commun.* 133–135 (2005).
29. Popescu, C. V. & Munck, E. Electronic structure of the H cluster in Fe-hydrogenases. *J. Am. Chem. Soc.* **121,** 7877–7884 (1999).
30. Pickett, C. J. & Ryder, K. S. Bioinorganic reaction centers on electrodes — Modified electrodes possessing amino-acid, peptide and ferredoxin-type groups on a poly(pyrrole) backbone. *J. Chem. Soc. Dalton Trans.* 2181–2189 (1994).

Supplementary Information accompanies the paper on **www.nature.com/nature**.

Acknowledgements This work was supported by the BBSRC and the John Innes Foundation. We thank D. J. Evans and J. E. Barclay for Mössbauer spectroscopy and discussions; L. Hill for ESMS; and R. R. Eady and R. A. Dixon for discussions and comments on the manuscript. Research done at Washington State University was supported by NIH and performed at EMSL, a national scientific user facility sponsored by the US DOE's Office of Biological and Environmental Research and located at PNNL, which is operated for DOE by Battelle.

Competing interests statement The authors declare that they have no competing financial interests.

Correspondence and requests for materials should be addressed to C.J.P. (chris.pickett@bbsrc.ac.uk). Crystal structure data for **B** have been deposited at the Cambridge Crystallographic Data Centre, and allocated the deposition number CCDC 256735.

Highly variable Northern Hemisphere temperatures reconstructed from low- and high-resolution proxy data

Anders Moberg[1], Dmitry M. Sonechkin[2], Karin Holmgren[3], Nina M. Datsenko[2] & Wibjörn Karlén[3]

[1]*Department of Meteorology, Stockholm University, SE-106 91 Stockholm, Sweden*
[2]*Dynamical-Stochastical Laboratory, Hydrometeorological Research Centre of Russia, Bolshoy Predtechensky Lane 11/13, Moscow 123 242, Russia*
[3]*Department of Physical Geography and Quaternary Geology, Stockholm University, SE-106 91 Stockholm, Sweden*

A number of reconstructions of millennial-scale climate variability have been carried out in order to understand patterns of natural climate variability, on decade to century timescales, and the role of anthropogenic forcing[1–8]. These reconstructions have mainly used tree-ring data and other data sets of annual to decadal resolution. Lake and ocean sediments have a lower time resolution, but provide climate information at multicentennial timescales that may not be captured by tree-ring data[9,10]. Here we reconstruct Northern Hemisphere temperatures for the past 2,000 years by combining low-resolution proxies with

J|A|C|S
ARTICLES
Published on Web 08/18/2007

Modeling [Fe−Fe] Hydrogenase: Evidence for Bridging Carbonyl and Distal Iron Coordination Vacancy in an Electrocatalytically Competent Proton Reduction by an Iron Thiolate Assembly That Operates through Fe(0)−Fe(II) Levels

Mun Hon Cheah,[†] Cédric Tard,[‡] Stacey J. Borg,[†] Xiaoming Liu,[‡] Saad K. Ibrahim,[‡] Christopher J. Pickett,*[,‡] and Stephen P. Best*[,†]

Contribution from the School of Chemistry, University of Melbourne, Victoria, Australia, 3010, and School of Chemical Sciences & Pharmacy, University of East Anglia, Norwich, NR4 7TJ

Received February 25, 2007; E-mail: spbest@unimelb.edu.au; c.pickett@uea.ac.uk

Abstract: IR spectroelectrochemistry of $Fe_4\{Me(CH_2S)_3\}_2(CO)_8$ (**4Fe6S**) in the ν(CO) region shows that the neutral and anion forms have all their CO groups terminally bound to the Fe atoms; however, for the dianion there is a switch of the coordination mode of at least one of the CO groups. The available structural and ν(CO) spectra are closely reproduced by density-functional theory calculations. The calculated structure of **4Fe6S**$^{2-}$ closely mirrors that of the diiron subsite of the [Fe−Fe] hydrogenase H cluster with a bridging CO group and an open coordination site on the outer Fe atom of pairs of dithiolate-bridged Fe^0Fe^{II} subunits connected by two bridging thiolates. Geometry optimization based on the all-terminal CO isomer of **4Fe6S**$^{2-}$ does not give a stable structure but reveals a second-order saddle point ca. 11.53 kcal mol^{-1} higher in energy than the CO-bridged form. Spectroelectrochemical studies of electrocatalytic proton reduction by **4Fe6S** show that slow turnover from the primary reduction process ($E_{1/2}' = -0.71$ V vs Ag/AgCl) involves rate-limiting protonation of **4Fe6S**$^-$ followed by reduction to H:**4Fe6S**$^-$. Rapid electrocatalytic proton reduction is obtained at potentials sufficient to access **4Fe6S**$^{2-}$, where the rate of dihydrogen elimination from the $Fe^{II}Fe^{II}$ core of **4Fe6S** is ca. 500 times faster than that from the $Fe^{I}Fe^{I}$ core of $Fe_2(\mu\text{-}S(CH_2)_3S)(CO)_6$. The dramatically increased rate of electrocatalysis obtained from **4Fe6S** over all previously identified model compounds appears to be related to the features uniquely common between it and the H-cluster, namely, that turnover involves the same formal redox states of the diiron unit ($Fe^{I}Fe^{II}$ and Fe^0Fe^{II}), the presence of an open site on the outer Fe atom of the Fe^0Fe^{II} unit, and the thiolate-bridge to a second one-electron redox unit.

Introduction

Notwithstanding the uncertainty remaining over the exact identity of the central light atom of the dithiolate bridge and the CO/CN arrangement, the structure of the catalytic center of the [Fe−Fe] hydrogenase enzyme is well-established by X-ray crystallographic[1−3] and spectroscopic[3−5] investigations. These results provide a framework for the development and evaluation of computational methods for describing the system. In this regard, density functional theory (DFT) has been shown to be extremely effective in terms of reproducing both the structure and spectroscopic details of closely related diiron compounds.[6−9] Importantly, these approaches offer the possibility of charting the reaction path or, more properly, providing a quantitative basis for excluding alternative reaction schemes.

Deliberation on the reaction path for dihydrogen oxidation has focused on the open coordination site of Fe_d (Scheme 1), the site of CO binding in the CO inhibited form of the enzyme.[12] Both $[2Fe]_{H_{ox}}$ and its one-electron-reduced analogue, $[2Fe]_{H_{red}}$, have similar structures, although in the latter case there is a weak interaction between Fe_p and the bridging CO group to give an up:down edge-shared bi-square pyramidal geometry.[1,3,13] Activation of dihydrogen may proceed by dihydrogen binding

[†] University of Melbourne.
[‡] University of East Anglia.

(1) Nicolet, Y.; Piras, C.; Legrand, P.; Hatchikian, C. E.; Fontecilla-Camps, J. C. *Structure* **1999**, *7*, 13−23.
(2) Peters, J. W.; Lanzilotta, W. N.; Lemon, B. J.; Seefeldt, L. C. *Science* **1998**, *282*, 1853−8.
(3) Nicolet, Y.; de Lacey, A. L.; Vernede, X.; Fernandez, V. M.; Hatchikian, E. C.; Fontecilla-Camps, J. C. *J. Am. Chem. Soc.* **2001**, *123*, 1596−601.
(4) Pierik, A. J.; Hulstein, M.; Hagen, W. R.; Albracht, S. P. J. *Eur. J. Biochem.* **1998**, *258*, 572−8. Chen, Z.; Lemon, B. J.; Huang, S.; Swartz, D. J.; Peters, J. W.; Bagley, K. A. *Biochemistry* **2002**, *41*, 2036−43.
(5) de Lacey, A. L.; Stadler, C.; Cavazza, C.; Hatchikian, E. C.; Fernandez, V. M. *J. Am. Chem. Soc.* **2000**, *122*, 11232−3.
(6) Fiedler, A. T.; Brunold, T. C. *Inorg. Chem.* **2005**, *44*, 9322−34. Zilberman, S.; Stiefel, E. I.; Cohen, M. H.; Car, R. *J. Phys. Chem. B* **2006**, *110*, 7049−57. Tye, J. W.; Darensbourg, M. Y.; Hall, M. B. *J. Comput. Chem.* **2006**, *27*, 1454−62. Bruschi, M.; Zampella, G.; Fantucci, P.; De Gioia, L. *Coord. Chem. Rev.* **2005**, *249*, 1620−40. Zilberman, S.; Stiefel, E. I.; Cohen, M. H.; Car, R. *Inorg. Chem.* **2006**, *45*, 5715−7.
(7) Fiedler, A. T.; Brunold, T. C. *Inorg. Chem.* **2005**, *44*, 1794−809.
(8) Bruschi, M.; Fantucci, P.; De Gioia, L. *Inorg. Chem.* **2002**, *41*, 1421−9.
(9) Borg, S. J.; Tye, J. W.; Hall, M. B.; Best, S. P. *Inorg. Chem.* **2007**, *46*, 384−94.
(10) Cao, Z.; Hall, M. B. *J. Am. Chem. Soc.* **2001**, *123*, 3734−42. Fan, H.-J.; Hall, M. B. *J. Am. Chem. Soc.* **2001**, *123*, 3828−9. Liu, Z.-P.; Hu, P. *J. Chem. Phys.* **2002**, *117*, 8177−80. Liu, Z.-P.; Hu, P. *J. Am. Chem. Soc.* **2002**, *124*, 5175−82.
(11) Zhou, T.; Mo, Y.; Liu, A.; Zhou, Z.; Tsai, K. R. *Inorg. Chem.* **2004**, *43*, 923−30.
(12) Lemon, B. J.; Peters, J. W. *Biochemistry* **1999**, *38*, 12969−73.

10.1021/ja071331f CCC: $37.00

Scheme 1. Schematic Representation of $\mathbf{H_{ox}}$, the Catalytic Center of the Oxidized Form of [Fe−Fe] Hydrogenase, the Diiron Subsite, $[2Fe]_{H_{ox}}$, and Structures of Intermediates Associated with the Pathways for Dihydrogen Activation That Involve Dihydrogen Binding to (a) Fe_d[10] or (b) to Both Metal Atoms of the Diiron Subsite[8,11]

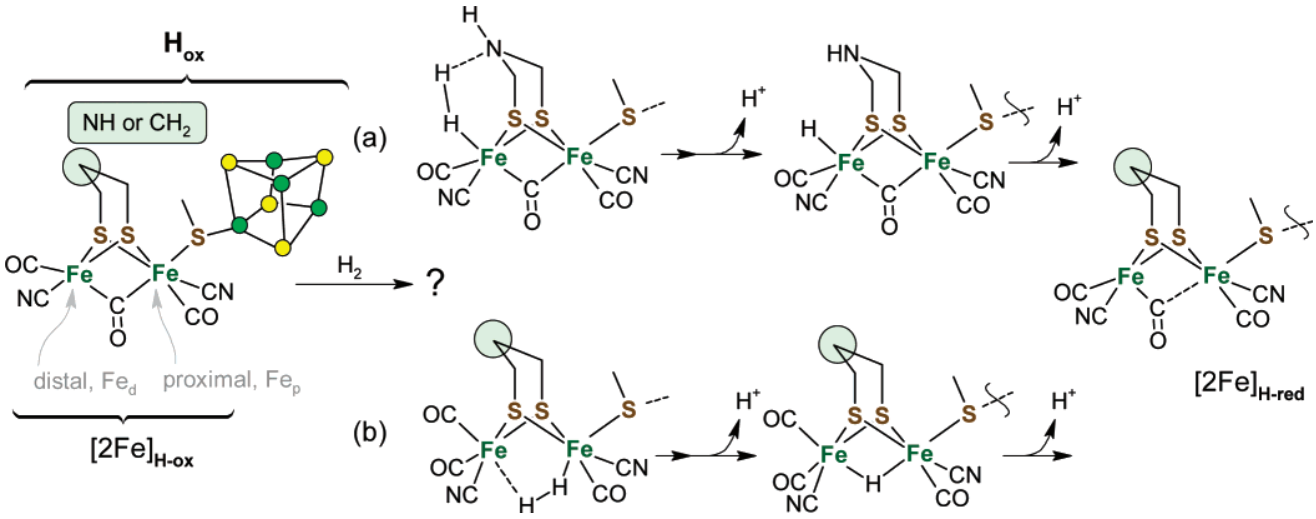

to this site (Scheme 1a). Heterolytic cleavage of bound dihydrogen would be assisted by interaction with the lone pair of the nitrogen atom of a di(thiomethyl)amine (dta) bridging ligand. DFT calculations suggest that such a path is energetically feasible,[10] and there is independent support for the assignment of the dta bridge based on analysis of the hydrogen-bonding interactions in the crystal.[5] An alternate reaction path may be proposed that involves dihydrogen binding to Fe_p where Fe_d interacts with the nonbonded hydrogen atom. In this case, dihydrogen binding is coupled with the bridging CO group adopting a terminal mode of coordination to Fe_d (Scheme 1b). DFT calculations suggest that this reaction path is also energetically feasible,[8,11] and a recent comparative study of the alternative proposals suggests that the energy differences are not sufficiently large for the DFT methods to allow exclusion of either alternative.[14]

There are excellent structural and functional models of the H-cluster, and progress in these areas has recently been reviewed.[15] For the most part, the focus has concentrated on $[2Fe]_{\mathbf{H}}$, where the most simple example, $Fe_2(\mu\text{-}S(CH_2)_3S)(CO)_6$ (**3S**), has been shown also to exhibit hydrogenase activity—at least in terms of electrocatalytic proton reduction.[16,17] Further elaboration by incorporation of a dta bridge,[18,19] regiospecific cyanation,[20] and site differentiation by incorporation of a pendant thioether or thiolate to the bridging ligand[19,21] yields close compositional analogues of the CO inhibited form of $[2Fe]_{\mathbf{H}}$ and an all-CO analog that incorporates both the **2Fe3S** and **4Fe4S** domains of $\mathbf{H_{ox}}$.[22] Spectroscopic and computational studies of ligand substitution reactions of diiron compounds related to $[2Fe]_{\mathbf{H}}$ suggest that a change in the mode of CO coordination facilitates ligand association/dissociation.[23,24] Simply, this allows the higher coordination intermediate to be accommodated by homolytic cleavage of the Fe−Fe bond while an 18-electron count is retained at both metal centers. However, these considerations do not provide a basis for distinction between the alternate pathways shown in Scheme 1. While a higher reactivity for terminally bound over bridging hydrides is suggested by studies of the isomers of $[HFe_2(\mu\text{-}S(CH_2)_2S)(CO)_2(PMe_3)_4]^+$ recently reported by Rauchfuss and co-workers,[25] the protonated forms of $[H_nFe_2(\mu\text{-}PPh_2)_2(CO)_6]^{n-2}$, n = 1 or 2, have terminally bound hydrides, and these are unreactive with protons.[26,27] Moreover, $Fe_2(\mu\text{-}PPh_2(CH_2)_3PPh_2)(CO)_6$ (**3P**) and **3S** undergo electrocatalytic proton reduction at similar rates, where the reaction path appears to involve a bridging hydride (i.e., the reverse of Scheme 1b).[28] This conclusion is supported by an independent DFT study of the reaction path for **3S**.[29] Central to the current investigation is the relative importance of bridging and terminally bound hydrides in the reaction path and, consequently, the role of the two iron atoms of $[2Fe]_{\mathbf{H}}$ in

(13) Nicolet, Y.; Lemon, B. J.; Fontecilla-Camps, J. C.; Peters, J. W. *Trends Biochem. Sci.* **2000**, *25*, 138−43.
(14) Zampella, G.; Greco, C.; Fantucci, P.; De Gioia, L. *Inorg. Chem.* **2006**, *45*, 4109−18.
(15) Liu, X.; Ibrahim, S. K.; Tard, C.; Pickett, C. J. *Coord. Chem. Rev.* **2005**, *249*, 1641−52. Capon, J.-F.; Gloaguen, F.; Schollhammer, P.; Talarmin, J. *Coord. Chem. Rev.* **2005**, *249*, 1664−76.
(16) Borg, S. J.; Behrsing, T.; Best, S. P.; Razavet, M.; Liu, X.; Pickett, C. J. *J. Am. Chem. Soc.* **2004**, *126*, 16988−99.
(17) Chong, D.; Georgakaki, I. P.; Mejia-Rodriguez, R.; Sanabria-Chinchilla, J.; Soriaga, M. P.; Darensbourg, M. Y. *Dalton Trans.* **2003**, 4158−63.
(18) Lawrence, J. D.; Li, H.; Rauchfuss, T. B.; Benard, M.; Rohmer, M.-M. *Angew. Chem., Int. Ed.* **2001**, *40*, 1768−71. Li, H.; Rauchfuss, T. B. *J. Am. Chem. Soc.* **2002**, *124*, 726−7.
(19) Lawrence, J. D.; Li, H.; Rauchfuss, T. B. *Chem. Commun.* **2001**, 1482−3.
(20) Lyon, E. J.; Georgakaki, I. P.; Reibenspies, J. H.; Darensbourg, M. Y. *Angew. Chem., Int. Ed.* **1999**, *38*, 3178−80. Cloirec, A. L.; Davies, S. C.; Evans, D. J.; Hughes, D. L.; Pickett, C. J.; Best, S. P.; Borg, S. *Chem. Commun.* **1999**, 2285−6. Schmidt, M.; Contakes, S. M.; Rauchfuss, T. B. *J. Am. Chem. Soc.* **1999**, *121*, 9736−7.
(21) Razavet, M.; Davies, S. C.; Hughes, D. L.; Pickett, C. J. *Chem. Commun.* **2001**, 847−8. Razavet, M.; Davies, S. C.; Hughes, D. L.; Barclay, J. E.; Evans, D. J.; Fairhurst, S. A.; Liu, X.; Pickett, C. J. *Dalton Trans.* **2003**, 586−95.
(22) Tard, C.; Liu, X.; Ibrahim Saad, K.; Bruschi, M.; De Gioia, L.; Davies, S. C.; Yang, X.; Wang, L.-S.; Sawers, G.; Pickett, C., J. *Nature* **2005**, *433*, 610−3.
(23) George, S. J.; Cui, Z.; Razavet, M.; Pickett, C. J. *Chem.—Eur. J.* **2002**, *8*, 4037−46.
(24) Boyke, C. A.; Rauchfuss, T. B.; Wilson, S. R.; Rohmer, M.-M.; Benard, M. *J. Am. Chem. Soc.* **2004**, *126*, 15151−60. Darensbourg, M. Y.; Lyon, E. J.; Zhao, X.; Georgakaki, I. P. *Proc. Natl. Acad. Sci. U.S.A.* **2003**, *100*, 3683−8. Zampella, G.; Bruschi, M.; Fantucci, P.; Razavet, M.; Pickett, C. J.; De Gioia, L. *Chem.—Eur. J.* **2005**, *11*, 509−20.
(25) van der Vlugt, J. I.; Rauchfuss, T. B.; Whaley, C. M.; Wilson, S. R. *J. Am. Chem. Soc.* **2005**, *127*, 16012−3.
(26) Cheah, M. H.; Borg, S. J.; Bondin, M. I.; Best, S. P. *Inorg. Chem.* **2004**, *43*, 5635−44.
(27) Dobbie, R. C.; Whittaker, D. *Chem. Commun.* **1970**, 796−7.
(28) Cheah, M. H.; Borg, S. J.; Best, S. P. *Inorg. Chem.* **2007**, *46*, 1741−50.
(29) Greco, C.; Zampella, G.; Bertini, L.; Bruschi, M.; Fantucci, P.; Gioia, L. D. *Inorg. Chem.* **2007**, *47*, 108−16.

dihydrogen activation (Scheme 1). Since the choreography of the reaction involves either CO or H bridging of the diiron centers, the reaction path may be considered from the perspective of either the H or CO groups.

The compound $Fe_4[MeC(SCH_2)_3]_2(CO)_8$ (**4Fe6S**), which is formed in the reaction of Bosnich's trithiol and $[Fe_3(CO)_{12}]$,[30] presents pairs of dithiolate-bridged diiron centers that feature markedly different coordination environments for the Fe atoms and promotes electrocatalytic proton reduction at relatively mild potentials and at a higher formal oxidation state for the Fe centers than for previously identified structural or functional models of $[2Fe]_{\mathbf{H}}$. The present investigation seeks to delineate the reduction chemistry of **4Fe6S** and to establish the relationships between this chemistry and that of $[2Fe]_{\mathbf{H}}$.

Experimental Section

Unless otherwise stated chemicals (Aldrich) and high-purity gases (BOC) were obtained from commercial sources and used without further purification. The ^{13}CO (99.2 atom %) was obtained from Trace Sciences International Corp., Ontario, Canada. Elemental analyses were performed by Medac Ltd, Egham, UK. Solvents were purified using standard procedures[31] and were distilled under a dinitrogen atmosphere immediately prior to use or transfer to a glove box (Vacuum Atmospheres). Tetra-n-butylammonium hexafluorophosphate (TBA-$[PF_6]$) was synthesized and purified using standard procedures[32] and lutidinium *p*-toluenesulfonate, LutH[OTs], was prepared by reaction of 2,6-dimethylpyridine (Lut) with the appropriate acid.

Synthesis of $Fe_4(CO)_8(CH_3C(CH_2S)_2)_2 \cdot {}^1/_2(CH_2Cl_2)$, 4Fe6S·$^1/_2(CH_2Cl_2)$. $Fe_3(CO)_{12}$ (3.0 g, 5.9 mmol) was dissolved in toluene (50 cm^3) and stirred. 1,1,1-Tris(mercaptomethyl)ethane (1.0 g, 5.9 mmol) was added and the solution was heated at 80 °C for 2 h. After solvent removal, the solid was purified by flash chromatography (diethyl ether and then dichloromethane) to give a dark brown solid (0.27 g, 0.3 mmol, 10%). This solid was recrystallized from dichloromethane to afford a shiny, microcrystalline brown-black material. ν_{max}/cm^{-1} (CO): 2046, 1988 and 1947 cm^{-1} (dichloromethane). NMR δ_H (400 MHz; solvent $CDCl_3$; standard $SiMe_4$): 0.94 (s, 6H, 2×CH_3), 1.16 (2H, d, *J* 14.2 Hz, 2×C*H*SFe), 1.59 (2H, d, *J* 14.2 Hz, 2×C*H*SFe), 1.97 (2H, d, *J* 13.9 Hz, 2×C*H*SFe), 2.13 (2H, d, *J* 13.2 Hz, 2×C*H*SFe), 2.77 (2H, d, *J* 13.7 Hz, 2×C*H*SFe), 3.54 (2H, d, *J* 13.7 Hz, 2×C*H*SFe), 5.32 (1H, 0.5 CH_2Cl_2). MS-FAB (NOBA matrix, *m*/*z*): M + H^+ 779. MS-ES+ (cone potential 50 V, solvent carrier $MeCN/CH_2Cl_2$ + ammonium acetate): M + H^+ 779, M + NH_4^+ 796. Anal. Calcd for $C_{18}H_{18}O_8S_6Fe_4 \cdot 1/2(CH_2Cl_2)$: C 27.08; H 2.33; S 23.4; Fe 27.2. Found: C 27.27; H 2.27; S 22.5; Fe 26.6.

Notes: The presence of 0.5 mol of dichloromethane per complex in the recrystallized material was confirmed by comparison of the integrated proton resonances for the complex with that for the solvate molecule in $CDCl_3$; experimental Fe and S analyses are somewhat low compared with theory, but this is not exceptional for this class of iron−sulfur compound,[33] where formation of metal sulfides can interfere in the analysis. Importantly, solution spectroscopic (FTIR, NMR) and electrochemical data reported above for the material used in this study is identical with that of structurally characterized **4Fe6S** prepared by the same method but isolated as homogeneous dark red needles from ethyl acetate/diethyl ether.[30]

Spectroelectrochemical (SEC) experiments were conducted using a purpose built cell previously described.[34] All experiments employed a 3 mm diameter vitreous carbon working electrode, silver pseudo-reference electrode, and platinum foil counter electrode. The potential of the reference electrode was estimated from the voltammetry of the solution under investigation and, by comparison with experiments conducted in the presence of ferrocene (Fc), all potentials are quoted relative to the Ag^+/AgCl reference electrode. Against this reference the Fc^+/Fc couple occurs at +0.51 V in CH_2Cl_2.[35] Solutions for SEC analysis were prepared under strictly anaerobic conditions either through the agency of a Vacuum Atmospheres glove box or using standard Schlenk techniques. The applied potential was controlled using a PAR model 362 potentiostat. A Powerlab 4/20 interface (ADInstruments) using EChem V1.5.2 or Chart V4.12 provided a means of setting the applied potential and monitoring the potential and current response during SEC experiments. IR spectra were obtained using a Bio-Rad FT175C FTIR equipped with a Ge/KBr beamsplitter and narrow band MCT detector. Spectral subtraction and curve fitting were performed using Grams/32 AI software (Galactic), and multicomponent analysis was conducted using routines available within Igor Pro (version 5.04B, Wavemetrics).

DFT calculations were carried out within the *Gaussion 03* (revision B.04)[36] suite using the exchange-correlation functional BP86[37] and LanL2DZ[38] (Fe and the C and H atoms of the bridge) and LanL2DZdp[39] (remaining atoms) basis sets obtained from Extensible Computational Chemistry Environment Basis Set Database, Version 02/25/04 (Molecular Science Computing Facility, Pacific Northwest Laboratory, Richland, WA). All geometries are fully optimized and confirmed as minima by an analytical frequency calculation at the same level of theory. DFT-optimized structures are indicated when parentheses enclose the formula used to designate the different species. The validity of the calculated gas-phase geometry may be established by comparison of the calculated and observed IR spectra in the ν(CO) region. Geometry optimization of **4Fe6S** using B3LYP and basis sets described above give structural parameters and ν(CO) band profiles in similarly good agreement with those observed; however the wavenumber offsets for these compounds were found to be smaller when using the BP86 functional. The inclusion of solvation effects provides more accurate estimates of the relative energies of the calculated structures, although a far smaller effect is evident for the calculated geometries and IR spectra. In view of the computational overhead for a problem as complex as that posed by the tetrairon compounds, all calculations reported are for gas-phase species. The crystal structure of **4Fe6S** was used as input for the DFT-based geometry optimization, where the suitability of the approach is demonstrated by the close agreement obtained between the observed and calculated geometry and ν(CO) bands. Geometry optimization of **4Fe6S**$^-$ proceeded from {**4Fe6S**} with the addition of a single electron. The procedure was repeated to give the calculated structure of **4Fe6S**$^{2-}$. In the crystalline form, **4Fe6S** has C_i symmetry[30] and geometry optimization of **4Fe6S**$^{0/-/2-}$ will also give structures with C_i symmetry. Calculations based on a starting geometry with C_1 symmetry refined to give structures indistinguishable from those calculated as described above. Starting geometries for H:**4Fe6S**$^-$ proceeded from {**4Fe6S**$^{2-}$} with placement of the hydrogen atom either at the open coordination site of one of the outer Fe atoms or between an outer and inner pair of Fe atoms. In the latter case, the bridging CO group was placed in the open coordination site of the outer Fe atom.

(30) Tard, C.; Liu, X.; Hughes, D. L.; Pickett, C. J. *Chem. Commun.* **2005**, 133−5.
(31) Armarego, W. L. F.; Perrin, D. D. *Purification of Laboratory Chemicals*, 4th ed.; Butterworth-Heinemann: Oxford, 1996.
(32) Sawyer, D. T.; Sobkowiak, A.; Roberts, J. J. L. *Electrochemistry for Chemists*, 2nd ed.; Wiley-Interscience: New York, 1995.
(33) Nehring, J. L.; Heinekey, D. M. *Inorg. Chem.* **2003**, *42*, 4288−92.
(34) Borg, S. J.; Best, S. P. *J. Electroanal. Chem.* **2002**, *535*, 57−64.
(35) Connelly, N. G.; Geiger, W. E. *Chem. Rev.* **1996**, *96*, 877−910.
(36) Frisch, M. J.; et al. *Gaussian 03*, revision B.04; Gaussian, Inc.: Wallingford, CT, 2004.
(37) Becke, A. D. *Phys. Rev. A* **1988**, *38*, 3098−100. Perdew, J. P. *Phys. Rev. B* **1986**, *33*, 8822−4.
(38) Dunning, T. H., Jr.; Hay, P. J. *Modern Theor. Chem.* **1977**, *3*, 1−27. Hay, P. J.; Wadt, W. R. *J. Chem. Phys.* **1985**, *82*, 270−83. Hay, P. J.; Wadt, W. R. *J. Chem. Phys.* **1985**, *82*, 299−310. Wadt, W. R.; Hay, P. J. *J. Chem. Phys.* **1985**, *82*, 284−98.
(39) Check, C. E.; Faust, T. O.; Bailey, J. M.; Wright, B. J.; Gilbert, T. M.; Sunderlin, L. S. *J. Phys. Chem. A* **2001**, *105*, 8111−6.

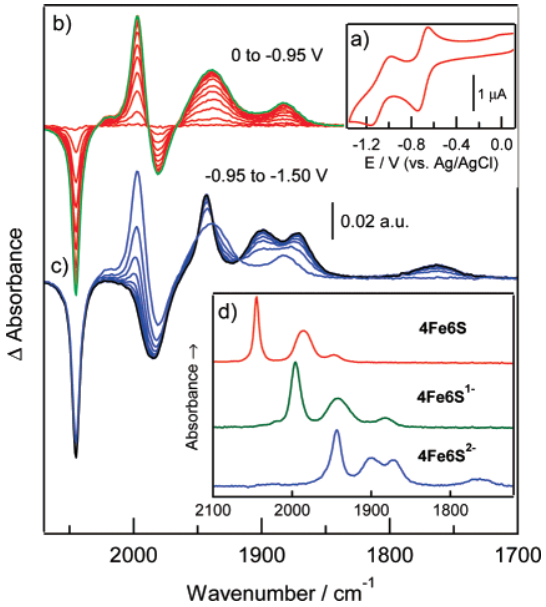

Figure 1. (a) Electrochemistry of **4Fe6S** (1 mM CH_2Cl_2/0.2 M TBA[PF_6]) and IR−SEC spectra after application of a potential of (b) −0.95 V and (c) −1.50 V. The time between spectra is ca. 2 s. (d) The absorbance spectra of the parent compound and the one- and two-electron reduction products, in the latter two cases by spectral subtraction using the SEC spectra.

Results and Discussion

Spectroelectrochemistry. The cyclic voltammetry of **4Fe6S** in CH_2Cl_2 reveals successive reversible and quasi-reversible single-electron reduction steps (Figure 1a).[30] Reversible interconversion between the neutral and anionic forms of **4Fe6S** is well-demonstrated in IR−SEC experiments, where the extent of recovery of the neutral species is near quantitative and not dependent on the reduction time (Figures 1b and S1 of the Supporting Information). Experiments conducted using more reducing potentials show that the dianion of **4Fe6S** is moderately stable at room temperature (Figure 1c), where ca. 95% of the anion can be recovered provided the duration of the reduction step is less than 10 s (Figure S2, Supporting Information). Reduction at longer times results in a more complex band profile consistent with the formation of several as yet undefined decomposition products. The IR spectra of **4Fe6S**$^-$ and **4Fe6S**$^{2-}$ have been extracted from the SEC results by spectral subtraction and these together with the spectrum of the parent compound are shown Figure 1d. Analogous experiments carried out under elevated pressures of CO (0.4 MPa) show that while **4Fe6S**$^-$ is unaffected by additional CO, **4Fe6S**$^{2-}$ undergoes further reaction, leading to a mixture of products (Figure S3, Supporting Information).

The general shift of the ν(CO) band profile lower by ca. 50 cm^{-1} with the addition of each electron is approximately half of that obtained for one-electron reduction of the related diiron compound, **3S**.[16] Further, since there is not a marked increase in the difference between the lowest and highest energy ν(CO) bands for either the anion or dianion, the additional charge is distributed over the four Fe atoms. This conclusion is supported by the magnitude of the shift of the highest energy ν(CO) bands. Furthermore, experiments carried out in the presence of elevated pressures of ^{13}CO show that reduction to the anion results in CO/^{13}CO exchange that continues over a period of ca. 30 s, presumably until the isotopic composition of CO bound to the

Table 1. Experimental (**4Fe6S**) and Predicted Bond Lengths for the Redox Series **4Fe6S**$^{0/-/2-}$ and the Terminal Hydride Form of **4Fe6S**$^{2-}$

					{H$_t$:**4Fe6S**$^{2-}$}^{b}	
	4Fe6S^a	{**4Fe6S**}^{b}	{**4Fe6S**$^-$}^{b}	{**4Fe6S**$^{2-}$}^{b}	H:**2Fe**^{c}	**2Fe**^{d}
$Fe_{outer}-Fe_{inner}$/Å	2.543	2.544	2.582	2.538	2.534	2.535
$Fe_{outer}-S_{outer}$/Å	2.264	2.297	2.305	2.351	2.318	2.350
$Fe_{inner}-Fe_{inner}$/Å	2.651	2.628	2.900	3.467	3.451	
$Fe_{inner}-S_{inner}$/Å	2.236	2.240	2.278	2.333	2.357	2.302
Fe−CO^e/Å	1.791	1.764	1.754	1.728	1.747	1.733
C−O^e/Å		1.173	1.180	1.189	1.176	1.184
$Fe_{inner}-CO_{bridge}$/Å				2.028	1.868	2.078
$Fe_{outer}-CO_{bridge}$/Å				1.855	2.132	1.825
$C-O_{bridge}$/Å				1.203	1.188	1.202

^{a} X-ray distances from ref 30. ^{b} DFT calculated distances. ^{c} Protonated diiron subunit of {H$_t$:**4Fe6S**$^{2-}$}, Fe−H = 1.490 Å. ^{d} Nonprotonated diiron subunit of {H$_t$:**4Fe6S**$^{2-}$}. ^{e} Averaged value.

complex matches that in the thin film of solution (Figure S4, Supporting Information). The lability of the complex to ligand exchange is consistent with its formulation as an odd-electron metal carbonyl species.[40] In addition to supporting the odd-electron assignment of **4Fe6S**$^-$ the isotopic substitution experiments also confirm assignment of the bands in this spectral region to metal carbonyl vibrations.

Similar ν(CO) band profiles are obtained for **4Fe6S** and **4Fe6S**$^-$; however, these differ markedly from that of the dianion (Figure 1d). The appearance of a ν(CO) band at 1780 cm^{-1} for **4Fe6S**$^{2-}$ suggests a rearrangement of the CO groups about the iron−sulfur core with the formation of a product having at least one bridging CO group. The substantial structural change indicated by the IR spectra is fully consistent with the slow heterogeneous electron-transfer kinetics suggested by the quasi-reversible nature of the second reduction wave (Figure 1a).[30]

DFT Studies of the 4Fe6S Redox Series. DFT calculations of the neutral compound yield structural parameters (Table 1) and IR spectrum (Figure 2a) in excellent agreement with that observed. The LUMO is calculated to be Fe−Fe antibonding with respect to the central Fe atoms, and on this basis, reduction would be expected to result in an increase in electron density distributed over both diiron fragments of the molecule. The shift of the entire band profile is consistent with such an analysis. The structure of {**4Fe6S**$^-$} has an elongated central Fe−Fe bond, and the calculated IR spectrum of the anion has a band profile and wavenumber in remarkably good agreement with those observed (Figure 2b). Whereas a further lengthening of the central Fe−Fe contact is expected following formation of {**4Fe6S**$^{2-}$}, it is surprising that this is also accompanied by a rearrangement of the CO groups. One of the terminal CO groups on both outer-Fe atoms is calculated to adopt a position bridging the outer and inner Fe atoms and this leaves an open coordination site on the outer-Fe atoms (Figure 3b). To ascertain the possibility for formation of the all-terminal CO isomer of **4Fe6S**$^{2-}$, geometry optimization was conducted starting from a model with a Fe/S core based on {**4Fe6S**$^{2-}$} and an arrangement of CO groups analogous to that of {**4Fe6S**$^-$}. While no local minimum with an all-terminal CO geometry is obtained, a second-order saddle point, 11.53 kcal mol^{-1} higher in energy than the CO-bridged form, is identified. In this case,

(40) Cotton, F. A.; Wilkinson, G. *Advanced Inorganic Chemistry*, 5th ed.; Wiley-Interscience: New York, 1988.

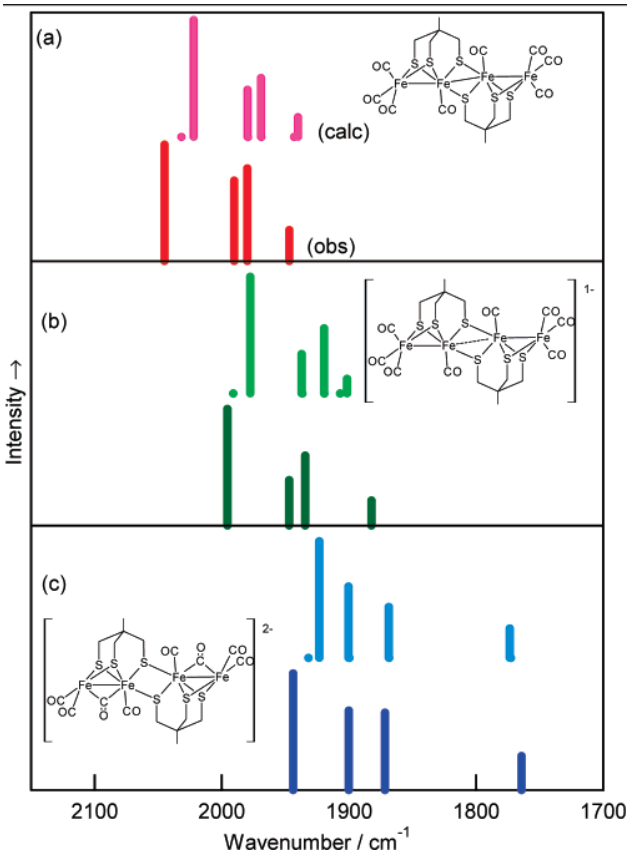

Figure 2. Comparison between the calculated (top) and observed (bottom) ν(CO) bands of (a) **4Fe6S**, (b) **4Fe6S**$^-$, and (c) **4Fe6S**$^{2-}$. The experimental intensities were obtained by curve fitting the ν(CO) band profile. The structures of **4Fe6S**$^-$ and **Fe6S**$^{2-}$ are based on those obtained by DFT calculation.

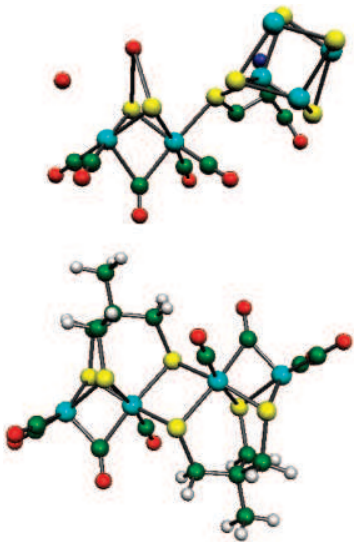

Figure 3. (top) Structure of $\mathbf{H_{ox}}$ as determined by X-ray crystallography of the oxidized form of the [Fe−Fe] hydrogenase from *C. pasteurianum* (PDB ID 1C4A).[2] Note in this published structure the atoms forming the dithiolate bridge were not refined nor assignment of the diatomic ligands as either CO or cyanide made (see Scheme 1). (bottom) DFT-calculated structure of **Fe4S6**$^{2-}$.

the two imaginary frequencies correspond to displacement coordinates that involve a rotation of the $Fe(CO)_3$ fragments and lead, ultimately, to the CO-bridged structure. These calculations suggest that the energy difference between the isomeric forms of {**4Fe6S**$^{2-}$} is significantly larger than the uncertainty in the relative energies introduced by the use of gas-phase calculations (up to 3 kcal mol^{-1}), this being estimated from studies of related diiron compounds.[9] The conclusion that the CO-bridged structure of {**4Fe6S**$^{2-}$} is significantly more stable than the all-terminal CO form is supported by the excellent agreement between the calculated and observed IR spectra (Figure 2c).

The high reactivity of **4Fe6S**$^{2-}$ is readily understood in terms of a CO-bridged structure with open coordination site on the outer Fe atoms, since a similar rearrangement of the all-terminal CO form has previously been invoked to explain the associative character of the substitution reactions. Pickett and co-workers have shown that cyanation of $Fe_2(\mu,\mu\text{-}(SCH_2)_2C(CH_3)(CH_2SR))(CN)(CO)_4$ proceeds through a long-lived CO-bridged intermediate, where transfer of the bridging CO group is coupled to dissociation of the pendant thioether to give the final product.[23]

The striking resemblance between the geometry of the diiron units of {**4Fe6S**$^{2-}$} and the X-ray structure of $\mathbf{H_{ox}}$ from *Clostridium pasteurianum*, CpI,[2] is shown in Figure 3. Both $[2Fe]_{\mathbf{H_{red}}}$ and the inner and outer pair of Fe atoms of {**4Fe6S**$^{2-}$} may have formal oxidation states of either Fe^IFe^I or $Fe^{II}Fe^0$. In both cases, a change in the mode of coordination of one of the CO groups between terminal and bridging will switch the oxidation state assignment from one alternative to the other. For **4Fe6S**$^{2-}$, the presence of two additional bridging thiolates bound to Fe_{inner} appears to push the equilibrium in favor of the $Fe^{II}Fe^0$ form. IR spectroscopy indicates that for $[2Fe]_{\mathbf{H_{red}}}$ all the CO groups adopt a terminal mode of coordination,[5] although the crystallographic structure indicates a hemibridging interaction between CO and Fe_p. DFT calculations indicate that this interaction mixes a significant $Fe^{II}Fe^0$ contribution into the ground state.[7] Thus, **4Fe6S**$^{2-}$ presents a close structural and electronic analogue of $\mathbf{H_{red}}$.

Spectroelectrochemistry in the Presence of 2,6-Dimethylpyridinium, LutH$^+$. IR−SEC spectra recorded during the reduction of **4Fe6S** at mild potentials in the presence of 20 equiv of LutH$^+$ are shown in Figure 4. The spectral changes closely mirror those obtained for reduction of **4Fe6S** in the absence of acid (Figure 1b), although the rate of depletion of the starting material is lower and weak features due to the conversion of LutH$^+$ to Lut become apparent in the spectrum between 1550 and 1700 cm^{-1}. The possibility that proton reduction involves either direct reduction at the electrode surface or is the result of the formation of low concentrations of the dianion was examined in experiments where the potentiostat was switched to open circuit at a time when both LutH$^+$ and **4Fe6S**$^-$ are present in the thin layer (Figure 4b). Over a period of ca. 50 s there is conversion of all the **4Fe6S**$^-$ to **4Fe6S**. The interpretation that the spectral changes observed during this period are due to chemical reaction, as opposed to mixing between the bulk solution and that of the thin layer, is based on the comparatively rapid time scale over which the spectral changes develop. Further, immediately after switching the cell to open circuit, the differential absorption features associated with the conversion of LutH$^+$ into its conjugate base, Lut, continue to develop while there is a significant concentration of **4Fe6S**$^-$ in the thin layer (Figure 4c). Analogous experiments conducted

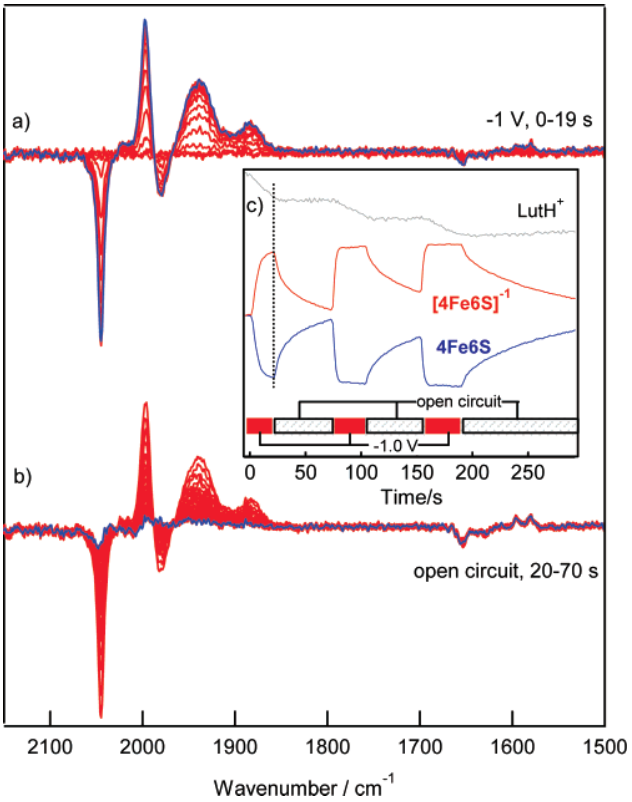

Figure 4. IR−SEC recorded of **4Fe6S** (1.7 mM, CH_2Cl_2/0.2 M TBA-[PF_6]) in the presence of $LutH^+$ (34 mM) (a) during the reduction at potentials sufficient to generate the monoanion, (b) the spectral changes obtained after switching the potentiostat to open circuit, and (c) the time dependence of the relative concentrations of $LutH^+$, **4Fe6S**, and **4Fe6S**$^-$ obtained by multicomponent fitting of the individual spectra. The last spectrum of each set shown in a and b is highlighted.

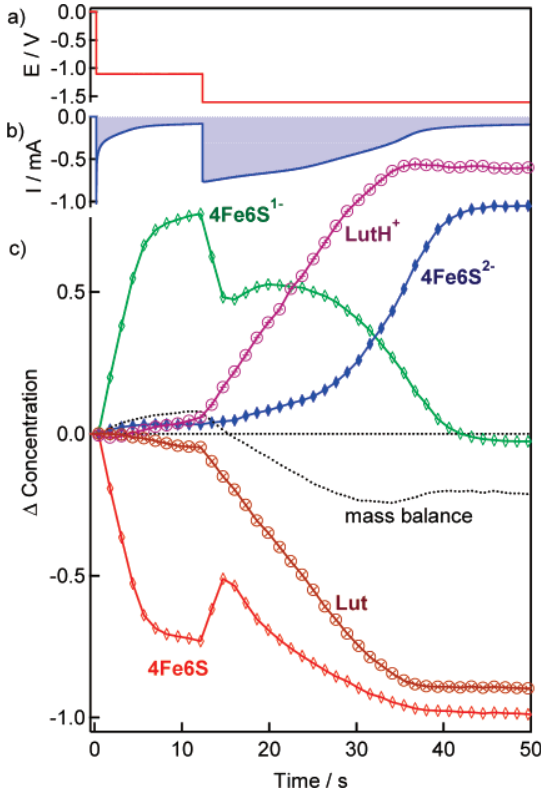

Figure 5. The time dependence of (a) the applied potential, (b) current response, and (c) the time dependence of the concentration changes of **4Fe6S**, **4Fe6S**$^-$, **4Fe6S**$^{2-}$, Lut, and $LutH^+$ during thin-layer SEC of **4Fe6S** (1.1 mM) and $LutH^+$ (38 mM) in CH_2Cl_2 (0.2 M TBA[PF_6]). The concentration changes of Lut and $LutH^+$ have been divided by a factor of 40. The mass balance of **4Fe6S**$''^-$ species corresponds to the sum of the concentration changes for **4Fe6S**, **4Fe6S**$^-$, and **4Fe6S**$^{2-}$.

in the absence of acid show that **4Fe6S**$^-$ is stable over the time scale of several minutes and there is no significant spectral change following the switching of the potentiostat to open circuit. The changes in concentration of **4Fe6S**, **4Fe6S**$^-$, and $LutH^+$ during an experiment including three successive reduction/open circuit cycles is shown in **Figure 4c**. With each reduction cycle there is a faster rate of depletion of the starting material and slower rate of its recovery. Both observations may be explained in terms of a lowering of the concentration of $LutH^+$ due to proton reduction in the thin layer of solution. It is important to note that the loss of **4Fe6S**$^-$ through formation of the dianion by disproportionation followed by reaction with acid may be ruled out by the small value of K_{disp} (ca. 10^{-6}). Since in this case formation of the dianion would be rate-limiting, the rate of reaction would be expected to be independent of acid concentration. This analysis is supported by electrochemical simulation of the voltammetry of **4Fe6S** in the presence of acid.[30]

These results show unequivocally that the reduction of protons by **4Fe6S**$^-$ is a kinetically significant process. The absence of additional spectral features during the reaction indicates that there is no buildup of significant concentrations of additional products; consequently, dihydrogen elimination by a bimolecular reaction involving two equivalents of H:**4Fe6S** can be ruled out. A reaction path involving rate-limiting formation of H:**4Fe6S**, reduction by **4Fe6S**$^-$, and rapid reaction of H:**4Fe6S**$^-$ with protons would account for the overall reaction and apparent absence of additional products. On the basis of the equilibrium constants and reduction potentials deduced from modeling the electrochemistry,[30] the equilibrium constant for the protonation of **4Fe6S**$^-$ is estimated to have a value of ca. 10. Complete removal of **4Fe6S**$^-$, as is evident in the SEC experiments, results from removal of the reaction product by irreversible protonation and dihydrogen elimination.

Since dihydrogen evolution following one-electron reduction is limited by the rate of protonation of **4Fe6S**$^-$, the time dependence of the spectral changes obtained after switching the potentiostat to open circuit provides a means of estimating the rate constant for the protonation reaction. For the first cycle an observed rate constant (k_{obs}) of 0.25 ± 0.01 s^{-1} is obtained from fitting the spectral changes for depletion of **4Fe6S**$^-$ and recovery of **4Fe6S** over the first half-life after switching the potentiostat to open circuit. For rate-limited protonation, k_{obs} will equal the product of the second-order rate constant for the protonation of **4Fe6S**$^-$ (k_1) and the concentration of $LutH^+$. The estimated value of k_1 of 9 ± 2 M^{-1} s^{-1} is in satisfactory agreement with that previously deduced from digital simulation of the electrochemistry (25 M^{-1} s^{-1}).[30]

The relative rates of electrocatalysis for the two reduction processes is apparent from the time and potential dependence of the spectral changes during thin layer SEC experiments of **4Fe6S** with 35 equiv of $LutH^+$. Reduction at mild potentials leads to a modest current response, and this is associated with conversion of a significant fraction of the neutral compound

Scheme 2. Possible Structures of H:**4Fe6S**$^-$

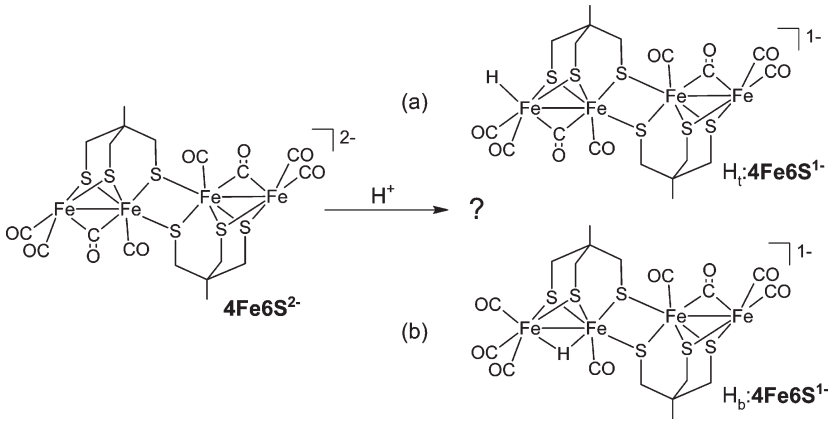

into the one-electron reduced form (Figure 5). Since the turnover on protons is slow, the predominant species in solution is **4Fe6S**$^-$. In the second stage of the reaction the potential is stepped to a value sufficiently reducing to access the dianion, and this is associated with a marked increase in the rate of depletion of $LutH^+$ together with an *increase* in the concentration of the neutral compound and concomitant decrease in concentration of **4Fe6S**$^-$ (Figure 5). This surprising situation may be explained in terms of the relative rates of recovery of **4Fe6S** by reaction of **4Fe6S^{2-}** and **4Fe6S**$^-$ with $LutH^+$. Analogous experiments conducted with differing acid concentrations and for different periods of reduction at -1.1 V suggest that the extent of transient recovery of **4Fe6S** after switching the potential to -1.6 V depends on the residual acid concentration. Despite the rapid turnover on protons following two-electron reduction, comproportionation of **4Fe6S^{2-}** and **4Fe6S** in the thin layer provides a means of generating significant concentrations of **4Fe6S**$^-$. Only when the concentration of **4Fe6S** is small does **4Fe6S^{2-}** become the predominant product (Figure 5). Following the application of more strongly reducing potentials, the mass balance of **4Fe6S^{n-}** species (Figure 5) indicates the formation of low concentrations of other metal-based species. It is clear that these species do not play a significant role in the catalytic reaction, since there is no delay in the onset of the full catalytic current following the step in potential. Rearrangement of protonated reduced compounds has previously been found to accompany the electrocatalytic reaction, and this is responsible for the loss of catalyst from the system.[16] It has not proved possible to obtain well-defined spectra of these products.

Digital simulation of the respective electrocatalytic proton reduction reactions suggests that the rate of dihydrogen elimination following two-electron, two-proton addition is substantially higher for **4Fe6S** (2000 s^{-1})[41] than either **3P** (2.4 s^{-1})[28] or **3S** (5 s^{-1}).[16] This order of reactivity is surprising, since the hydridic character of the species may be expected to be enhanced as the complex is reduced and the formal oxidation states of the iron atoms is higher for **4Fe6S** than for **3S** or **3P**. This suggests a different reaction path for electrocatalytic proton reduction by **4Fe6S**. Since the reaction path for rapid proton reduction by **4Fe6S** involves net two-electron reduction prior to protonation, it is likely that the structural rearrangement accompanying formation of **4Fe6S^{2-}** is central to the increased reactivity. Both the opening of a coordination site on the outer iron atom and the development of Fe^0Fe^{II} centers would promote the proton basicity and hydridic character needed to facilitate such a reaction.

A possible reaction path available to **4Fe6S^{2-}** and not the diiron compounds is for protonation to occur on the inner iron atoms and for both diiron fragments of H_2:**4Fe6S** to be directly involved in dihydrogen elimination. However, this reaction path may be excluded on the basis of the calculated Fe−Fe distance (Table 1). Recent theoretical[29] and experimental[28] studies of **3S** and **3P** suggest that electrocatalytic proton reduction proceeds via dihydrogen elimination from a Fe_A:Fe_B dihydride, where the rate of dihydrogen elimination is related to the H−H distance, this being related to the Fe_A−Fe_B separation.[28] The calculated structure of the H_2:**4Fe6S** isomer having the inner Fe atoms protonated has a Fe_{inner}−Fe_{inner} distance (3.447 Å) little changed from that of {**4Fe6S^{2-}**} (Table 1) and an H−H distance of 4.273 Å. A similar Fe−Fe distance is obtained for **DP^{2-}**, and in that case, the dihydride does not eliminate dihydrogen at a significant rate.[26]

Therefore, dihydrogen elimination from H_2:**4Fe6S** is centered on one of the Fe_{outer}−Fe_{inner} fragments with the remaining diiron fragment available to provide an additional reducing equivalent. Protonation of **4Fe6S^{2-}** may occur at the open coordination site of one of the outer iron atoms or, alternatively, at the inner iron atom, where this is coupled with a rearrangement of the bridging CO group (Scheme 2). These alternatives mirror the latter stages of the paths of dihydrogen oxidation proposed for the H-cluster (Scheme 1).

Dihydrogen elimination from a dihydride obtained by protonation of a species such as H_b:**4Fe6S**$^-$ may, in view of the shorter Fe_{outer}−Fe_{inner} separation, be expected to support a faster rate of dihydrogen elimination than the corresponding species of **3S** and **3P**; however, the oxidation states of the iron atoms is higher and this may be expected to lower the basicity of the H-bridged species. Crystallographically characterized hydride-bridged $Fe^{II}Fe^{II}$ species have been obtained by protonation of the disubstituted Fe^IFe^I phosphines[25] to give $[Fe_2(\mu\text{-pdt})(\mu\text{-H})(PR_3)_2(CO)_4]^+$ and by hydride addition to the $Fe^{II}Fe^{II}$ precursor of **2SH$_b$**$^+$.[42] In neither case is there any indication of significant

(41) The value of the rate constant for dihydrogen elimination was not given explicitly in ref 30. The value reported is obtained by fitting the voltammetry to a model consistent with those used in refs 28 and 16.

(42) Zhao, X.; Georgakaki, I. P.; Miller, M. L.; Mejia-Rodriguez, R.; Chiang, C.-Y.; Darensbourg, M. Y. *Inorg. Chem.* **2002**, *41*, 3917−28.

proton basicity, even in the presence of acids significantly stronger than $LutH^+$.

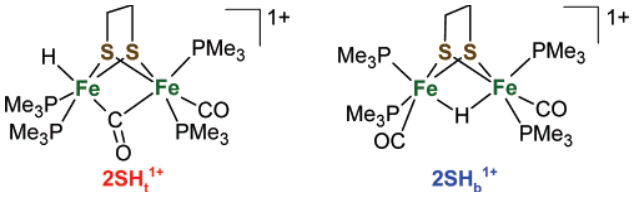

Terminally bound hydrides are known for thiolate- and phosphido-bridged diiron compounds, although the hydridic character of these diiron species is markedly different. Whereas $\mathbf{2SH_t}^+$ reacts with acid to eliminate dihydrogen, $[Fe_2(\mu\text{-}PPh_2)_2H(CO)_6]^-$ is unreactive. In the latter case, the IR spectra indicate that the two iron centers are weakly interacting and the hydride formulation would imply binding to an Fe^{II} center.[26] The difference in ligand set and stronger electronic interaction between the Fe^{II} centers of $\mathbf{2SH_t}^+$ would appear to promote the hydridic character of the terminally bound hydride. Similar considerations apply for H_t:**4Fe6S**$^-$, where the outer and inner iron atoms are bridged both by a dithiolate and a CO group as for $\mathbf{2SH_t}^+$ and, notably, $\mathbf{H_{ox}}$. The hydridic character of the tetrairon complex may be further enhanced by redistribution of charge from the remote pair of iron centers. Geometry optimization of H:**4Fe6S**$^-$ starting from the protonated form of **4Fe6S**$^{2-}$ corresponding to H_t:**4Fe6S**$^-$ (Scheme 2a) proceeds to a well-defined energy minimum, as judged by the calculated vibrational frequencies. The structure retains a terminal hydride and bridging CO group. These calculations suggest that the bridging CO group moves from a position closer to Fe_{outer} for the dianion to one closer to Fe_{inner} for {H_t:**4Fe6S**$^-$}, while there is a smaller shift of the bridging CO toward Fe_{outer} for the nonprotonated subunit (Table 1).

DFT-based geometry optimization of H_b:**4Fe6S**$^-$ (Scheme 2b) gives a similarly well-behaved minimum with a calculated gas-phase free energy 0.75 kcal mol^{-1} lower than that of {H_t:**4Fe6S**$^-$}, well within the uncertainty of the calculation. Further work is needed to establish whether there is a sufficiently large difference in the calculated activation energies to provide an unequivocal basis for distinguishing between the two reaction paths. These calculations would have clear parallels with those conducted on the enzyme.[14]

Conclusion

The application of SEC approaches has allowed identification of the IR spectra of the **4Fe6S**, **4Fe6S**$^-$, and **4Fe6S**$^{2-}$ redox series. Whereas the ν(CO) band pattern is largely retained following one-electron reduction, there are significant changes associated with formation of **4Fe6S**$^{2-}$, most notably the appearance of a ν(CO) band at 1764 cm^{-1} indicative of the presence of at least one CO group adopting a bridging mode of coordination.

DFT-based geometry optimization of **4Fe6S** gives structural parameters and IR spectra in excellent agreement with those observed. The LUMO is calculated to be antibonding with respect to the inner Fe atoms, and one-electron reduction is manifested by a lengthening of this bond. Addition of a second electron is calculated to give a further lengthening of the Fe_{inner}−Fe_{inner} distance and, unexpectantly, a rearrangement of the CO groups about the **4Fe6S** core. The calculated geometry consists of two identical diiron units with an open coordination site on Fe_{outer} and a bridging CO group on Fe_{outer} and Fe_{inner}. These features of the structure are unprecedented in dithiolate-bridged diiron chemistry outside the [Fe−Fe] hydrogenase enzyme.

Electrocatalytic proton reduction proceeds slowly at mild potentials by one-electron reduction of **4Fe6S**, rate-limiting protonation, further one-electron reduction, and dihydrogen elimination. A dramatic increase in the rate of electrocatalysis occurs if two-electron reduction precedes protonation. The structural rearrangement associated with formation of **4Fe6S**$^{2-}$ provides a diiron unit, which is closely related to $\mathbf{H_{red}}$ sharing (i) an accessible Fe^0Fe^{II} redox level with an open coordination site on the Fe^0 center and (ii) a thiolate bridge to a second redox center able to provide a second electron during proton reduction to give a final oxidized Fe^IFe^{II} form. These features of the chemistry clearly require differentiation of the coordination environments of the Fe centers of the diiron unit.

While further calculations are needed to establish unequivocally that an alternate reaction path of **4Fe6S** can be dismissed, consideration of the structures of the compounds, their relation to electrocatalytic proton reduction by **3S** and **3P**, and the difference in rate of dihydrogen elimination following protonation of $\mathbf{2SH_t}^+$ and $\mathbf{2SH_b}^+$ suggest formation of a terminal hydride (H_t:**4Fe6S**, Scheme 2a) and a reaction path analogous to the reverse of Scheme 1a. While lacking the CO/CN^- substitution pattern and including two, instead of one, bridging thiolate sulfur atoms to a second redox center, **4Fe6S** nevertheless provides important insights into the reaction path of the H cluster and for the design of new electrocatalysts.

Note Added in Proof. A paper published after submission of the manuscript (Ezzaher, S.; Capon, J.-F.; Gloaguen, F.; Pétillon, F. Y.; Schollhammer, P.; Talarmin, J.; Pichon, R.; Kervarec, N. *Inorg. Chem.* **2007**, *46*, 3426−8) shows that protonation of the asymmetrically substituted diiron(I) compound $Fe(\mu\text{-}S(CH_2)_3S)CO_4(dppe)$, dppe = $Ph_2PP(CH_2)_2PPh_2$, proceeds through a terminally bound hydride en route to the more stable hydride-bridged form. This observation provides further support for a reaction path for **4Fe6S** that involves a terminally bound hydride (Scheme 2a).

Acknowledgment. The work was supported by grants from the Australian Research Council (S.P.B. and C.J.P.), BBSRC (C.J.P.), the John Innes Centre (where the earlier work was initiated), and the EPSRC (Supergen 5, C.J.P.). M.H.C. and C.T. acknowledge the University of Melbourne and the John Innes Foundation, respectively, for the award of scholarships. Support of the Victorian Institute for Chemical Sciences High Performance Computing Facility is gratefully acknowledged.

Supporting Information Available: Full ref 36, IR−SEC showing recovery of **4Fe6S** from **4Fe6S**$^-$ and **4Fe6S**$^{2-}$, IR−SEC of **4Fe6S**$^{2-}$ under 0.4 MPa CO and **4Fe6S**$^-$ under 0.4 MPa ^{13}CO, Cartesian coordinates from DFT calculations, and frequencies and intensities of DFT-calculated species. This material is available free of charge via the Internet at http://pubs.acs.org.

JA071331F

Thermochromic Luminescence of Sol−Gel Films Based on Copper Iodide Clusters

Cédric Tard,[†] Sandrine Perruchas,*[,†] Sébastien Maron,[†] Xavier F. Le Goff,[‡] François Guillen,[§] Alain Garcia,[§] Jacky Vigneron,[||] Arnaud Etcheberry,[||] Thierry Gacoin,[†] and Jean-Pierre Boilot*[,†]

Laboratoire de Physique de la Matière Condensée (PMC) and Laboratoire Hétéroéléments et Coordination (DCPH), CNRS, Ecole Polytechnique, 91128 Palaiseau Cedex, France, Institut de Chimie de la Matière Condensée de Bordeaux (ICMCB), CNRS, 87 Avenue du Docteur A. Schweitzer, 33608 Pessac Cedex, France, and Institut Lavoisier de Versailles (ILV), UMR CNRS 8180, Université de Versailles Saint Quentin, 45 Avenue des Etats-Unis, 78035 Versailles Cedex, France

Received June 30, 2008. Revised Manuscript Received September 5, 2008

The incorporation of copper iodide clusters in sol−gel silica has been investigated to prepare materials with original luminescent properties. The synthesis, structural characterizations, and optical properties of sol−gel films containing $[Cu_4I_4L_4]$ clusters, L = phosphine-based ligands, are reported. Clusters studied are $[Cu_4I_4(PPh_2(CH_2)_2Si(OCH_2CH_3)_3)_4]$ (**C1**), able to copolymerize with the silica matrix, and $[Cu_4I_4(PPh_2(CH_2)_2CH_3)_4]$ (**C2**) used as a reference for the characterizations. The luminescent films exhibit the optical properties of these clusters in accordance with XPS and NMR studies demonstrating their integrity in the gel matrix. The temperature dependence of light emission properties of clusters and films shows, for the first time for phosphine-based $[Cu_4X_4L_4]$ clusters, thermochromic luminescence with bright yellow luminescence at room temperature and purple emission at 77 K. As a result of weak Cu−Cu interactions, the two emissive states appear as highly coupled with a low energy barrier (2 $kJ \cdot mol^{-1}$), leading to a controlled thermochromism in a large temperature range.

Introduction

Research on luminescent materials has been actively pursued in the last two decades due to their numerous applications in light emitting devices (fluorescent tubes, lasers, cathode X-ray, projection television, OLED, flat panel display, etc.). Silica- and/or siloxane-based hybrid organic−inorganic matrices present several advantages to design materials for optical applications such as mild synthesis conditions, versatile chemistry, easy shaping, good mechanical properties, and excellent optical quality.[1−3] For applications in solid-state lasers[4] or electroluminescent devices,[5] numerous luminescent transparent composite materials (films or monoliths) have been prepared by dispersing or grafting luminescent species in sol−gel silica matrices.[6] Organic dyes,[7] nanoparticles, such as semiconductor quantum dots,[8] and rare-earth doped oxides,[9] and also coordination complexes of lanthanide ions[10−13] generally constitute the active luminescent species trapped in these sol−gel materials. In the near future, luminescent transition metal clusters could represent another class of phosphors for the synthesis of light-emitting materials (silica-based materials or not). These molecular clusters are promising photoactive species since they combine inorganic nature of nanoparticles with monodisperse size distribution and easy functionalization of organic molecules.

Photoluminescent d^{10} coinage metal compounds have been studied for many years due to their various photophysical luminescent properties.[14−16] Among them, the formulated

* Corresponding authors. Fax: (+33) (0)1 69 33 47 99. Phone: (+33) (0)1 69 33 46 51. E-mail: sandrine.perruchas@polytechnique.edu (S.P.); jean-pierre.boilot@polytechnique.fr (J.-P.B.).
[†] Laboratoire de Physique de la Matière Condensée (PMC).
[‡] Laboratoire Hétéroéléments et Coordination (DCPH).
[§] Institut de Chimie de la Matière Condensée de Bordeaux (ICMCB).
[||] Université de Versailles Saint Quentin.

(1) (a) Brinker, C. J.; Scherrer, G. W. *Sol-Gel Science The Physics and Chemistry of Sol-Gel Processing*; Academic Press: San Diego, CA, 1990. (b) Avnir, D.; Levy, D.; Reisfeld, R. *J. Phys. Chem.* **1984**, *88*, 5956.
(2) (a) Sanchez, C.; Ribot, F. *New J. Chem.* **1994**, *18*, 1007. (b) Schubert, U.; Hüsing, N.; Lorenz, A. *Chem. Mater.* **1995**, *7*, 2010. (c) Loy, D. A.; Schea, K. J. *Chem. Rev.* **1995**, *95*, 1431.
(3) Pénard, A.-L.; Gacoin, T.; Boilot, J.-P. *Acc. Chem. Res.* **2007**, *40*, 895.
(4) Faloss, M.; Canva, M.; Georges, P.; Brun, A.; Chaput, F.; Boilot, J.-P. *Appl. Opt.* **1997**, *36*, 6760.
(5) de Morais, T. D.; Chaput, F.; Boilot, J.-P.; Lahlil, K.; Darracq, B.; Lévy, Y. *Adv. Mater. Opt. Electron.* **2000**, *10*, 69.
(6) Sanchez, C.; Lebeau, B.; Chaput, F.; Boilot, J.-P. *Adv. Mater.* **2003**, *15*, 1969.
(7) Avnir, D.; Braun, S.; Lev, O.; Levy, D.; Ottolenghi, M. *Sol-Gel Optics, Processing and Applications*; Klein, L. C., Ed.; Kluwer Academic Publishers: Dordrecht, 1994; p 539.
(8) (a) Epifani, M.; Leo, G.; Lomascolo, M.; Vasanelli, L.; Manna, L. *J. Sol-Gel Sci. Technol.* **2003**, *26*, 441. (b) Lifshitz, E.; Dag, I.; Litvin, I.; Hodes, G.; Gorer, S.; Reisfeld, R.; Zelner, M.; Minti, H. *Chem. Phys. Lett.* **1998**, *288*, 188.
(9) Buissette, V.; Giaume, D.; Gacoin, T.; Boilot, J.-P. *J. Mater. Chem.* **2006**, *16*, 529.
(10) Armelao, L.; Bottaro, G.; Quici, S.; Cavazzini, M.; Raffo, M. C.; Barigelletti, F.; Accorsi, G. *Chem. Commun.* **2007**, 2911.
(11) Qi, W.; Li, H.; Wu, L. *Adv. Mater.* **2007**, *19*, 1983.
(12) Lenaerts, P.; Storms, A.; Mullens, J.; D'Haen, J.; Görller-Walrand, C.; Binnemas, K.; Driesen, K. *Chem. Mater.* **2005**, *17*, 5194.
(13) Raehm, L.; Mehdi, A.; Wickleder, C.; Reyé, C.; Corriu, J. P. *Chem. Mater.* **2007**, *129*, 12636.
(14) Barbieri, A.; Accorsi, G.; Armaroli, N. *Chem. Commun.* **2008**, 2185.

10.1021/cm801780g CCC: $40.75
Published on Web 10/08/2008

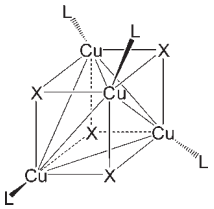

Figure 1. General representation of $[Cu_4X_4L_4]$ clusters (X = Cl, Br, I; L = pyridine or amine-based derivatives).

tretracopper(I) clusters $[Cu_4X_4L_4]$ (X = Cl, Br, I; L = pyridine or amine-based derivatives) are known to be highly luminescent at room temperature.[15,17] The molecular structure of these cubane type clusters is represented Figure 1. These compounds are easily synthesized in solution and can be obtained with different types of ligands (L) allowing their functionalization. Besides, these copper clusters display emission spectra that are strikingly sensitive to their environment, the temperature, and the rigidity of the medium. For example, the thermochromic luminescence[18] originates from two emission bands whose relative intensities vary in temperature.[19] At room temperature, the luminescence is dominated by a low energy band (LE) which has been attributed, based on experimental data[15] and recent DFT calculations,[20] to a combination of a halide-to-metal charge transfer (XMCT) and copper-centered d → s, p transitions. This emission is called "cluster centered" (^{3}CC) as it involves a $[Cu_4I_4]$ cluster centered triplet excited state, which is essentially independent of the nature of the ligand. At low temperature, this band is extremely weak, and the emission is dominated by a higher energy band (HE) which has been attributed to a triplet halide-to-pyridine ligand charge-transfer (^{3}XLCT) excited state. As the π^* orbitals of the ligands are involved in this XLCT band, the emission at low temperature is only observed for clusters incorporating π-unsaturated ligands. All these properties make these copper clusters particularly attractive for their incorporation in organic or inorganic polymeric matrices, to synthesize materials with original optical applications. To our knowledge no such cluster-based materials have been already reported.

There have been considerably less photophysical investigations of $[Cu_4X_4L_4]$ clusters with L = phosphine derivatives compared to pyridines or amines ones. The only luminescence studies reported for clusters with the $[Cu_4I_4]$ core have concerned the emission at 654 nm of $[Cu_4I_4(P^nBu_3)_4]$[15] at room temperature in toluene and of $[Cu_4I_4(dmpp)_4]$ (dmpp = 1-phenyl-3,4-dimethylphosphole)[21,22] at 15 K in the solid state at 664 nm. By analogy with $[Cu_4I_4L_4]$ (L = pyridine or amine derivatives) clusters, this emission observed for $[Cu_4I_4(P^nBu_3)_4]$ was attributed to the LE band previously cited (XMCT/d-s). The absence of the HE band was explained by the saturated aliphatic character of the P^nBu_3 ligand. For $[Cu_4I_4(dmpp)_4]$, the emission was assigned to a metal−ligand charge-transfer transition (MLCT) based on vibronic structure analyses. No luminescence properties at low temperature have been reported for these two compounds.

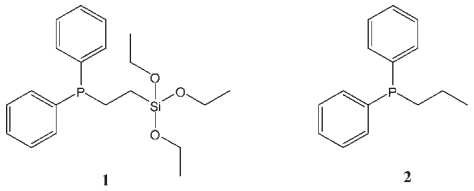

Figure 2. Phosphine ligands studied: **1** = $PPh_2(CH_2)_2Si(OCH_2CH_3)_3$, **2** = $PPh_2(CH_2)_2CH_3$.

Herein, we report on the synthesis, structural characterizations, and optical properties of sol−gel films containing $[Cu_4I_4L_4]$ clusters. Iodide cluster derivatives were selected because of their known higher luminescence quantum yield and stability compared to the chloride and bromide analogues.[15] An original copper iodide cluster with phosphine ligands bearing alcoxysilane groups is synthesized allowing a covalent grafting of clusters to the silica matrix. Since luminescence properties of $[Cu_4I_4L_4]$ clusters having phosphine ligands are not well-known, a reference cluster without polymerizable groups is also prepared to facilitate the characterization of films. Thus, the cluster integrity in sol−gel films is demonstrated from XPS and NMR studies. Light emission properties of clusters and films are studied in detail as a function of the temperature. The thermochromic luminescence is observed for the first time in sol−gel films. Under UV excitation, clusters and films exhibit a bright yellow luminescence at room temperature, while the emission becomes purple after immersion in liquid nitrogen. Moreover, we clearly display the high coupling between excited states (^{3}XLCT and ^{3}CC) with the appearance of two thermally equilibrated emissions in the 10−120 K range.

Experimental Section

Synthesis. All manipulations were performed with standard air-free techniques using Schlenk equipment, unless otherwise noted. Solvents were distilled from appropriate drying agents and degassed prior to use. Diphenyl-ethyltriethoxysilane-phosphine (**1**) was synthesized by the method reported in the literature.[23] Copper(I) iodide, diphenyl-propyl-phosphine (**2**), and methyltriethoxysilane (MTEOS) were purchased from Aldrich and used as received.

C1-2. To a suspension of CuI in dichloromethane (20 mL) was added the corresponding ligand (**1** or **2**) (Figure 2). The solution was stirred for 2 h at room temperature. The mixture was filtrated, and after evaporation of the solvent the product was recovered as colorless oil for **C1**. **C2** was purified by flash chromatography (silica gel, cyclohexane/ethylacetate 4:1), and colorless crystals were obtained by slowly cooling the cyclohexane/ethylacetate solution from room temperature to 4 °C. **C1**: CuI (1.0 g, 5.3 mmol), **1** (2.0 g, 5.3 mmol), yield = 72% (2.2 g, 0.95 mmol). **C2**: CuI (840 mg, 4.4 mmol), **2** (1 g, 4.4 mmol), yield = 76% (1.4 g, 3.3 mmol). Elemental analyses and NMR characterization are reported in Supporting Information.

(15) Ford, P. C.; Cariati, E.; Bourasssa, J. *Chem. Rev.* **1999**, *99*, 3625.
(16) Yam, V. W.-W.; Lo, K. K.-W. *Chem. Soc. Rev.* **1999**, *28*, 323.
(17) Vitale, M.; Ford, P. C. *Coord. Chem. Rev.* **2001**, *219*, 3.
(18) Hardt, H. D.; Pierre, A. *Z. Anorg. Allg. Chem.* **1973**, *402*, 107.
(19) Kyle, K. R.; Ryu, C. K.; DiBenedetto, J. A.; Ford, P. C. *J. Am. Chem. Soc.* **1991**, *113*, 2954.
(20) De Angelis, F.; Fantacci, S.; Sgamellotti, A.; Cariati, E.; Ugo, R.; Ford, P. C. *Inorg. Chem.* **2006**, *45*, 10576.
(21) Lai, D. C.; Zink, J. I. *Inorg. Chem.* **1993**, *32*, 2594.
(22) Attar, S.; Bowmaker, G. A.; Alcock, N. W.; Frye, J. S.; Bearden, W. H.; Nelson, J. H. *Inorg. Chem.* **1991**, *30*, 4743.
(23) Bunlaksananusorn, T.; Knochel, P. *Tetrahedron Lett.* **2002**, *43*, 5817.

C1 *Films.* The sol was prepared by mixing **C1** cluster, methyltriethoxysilane (MTEOS), *N*,*N*-dimethylformamide, and HCl aqueous solution (pH = 2.5) with a molar ratio of 1.5×10^{-3}:1:3:3. The mixture was stirred at room temperature overnight. The solvents were evaporated until the volume of the solution was reduced by 80% and a viscous liquid was obtained. After filtration a colorless and transparent liquid was obtained which was diluted by a factor of 2 with tetrahydrofuran and spin-coated on substrates at room temperature (3000 rpm, 2 min). Films obtained were colorless with thickness typically of 500 nm to 1 μm. The substrates (glass, silica, silicon) were previously soaked in a piranha solution, washed with water and ethanol, and dried.

Characterizations. ^{1}H and ^{31}P liquid-state NMR spectra were recorded on Bruker AvanceII300 or Tecmag Apollo360 spectrometers, respectively, using Bruker probes at room temperature, operating at the radio frequency of 300 MHz (for ^{1}H) and 145 MHz (for ^{31}P). ^{1}H spectra were internally referenced from peaks of residual protons in deuterated solvents or from tetramethylsilane (TMS). A solution of 85 wt % H_3PO_4 was used as an external standard for ^{31}P spectra. Elemental analyses (C, H) were performed by the Service Central d'Analyses, CNRS of Vernaison. UV−visible absorption and transmittance spectra were recorded with a Varian Cary 50 spectrophotometer on films deposited on quartz substrates.

Luminescence spectra were recorded on a SPEX Fluorolog FL 212 spectrofluorimeter (HORIBA JOBIN YVON). The excitation source is a 450 W xenon lamp; excitation spectra were corrected for the variation of the incident lamp flux, as well as emission spectra for the transmission of the monochromator and the response of the photomultiplier (Peltier cooled Hamamatsu R928P photomultiplier). Low temperature measurements have been done with two different setups: a liquid nitrogen cryostat Meric TR S1900 or a liquid helium circulation cryostat SMC TBT Air Liquid model C102084. Determinations of the quantum luminescence yield for clusters and films are described in Supporting Information.

XPS spectra were recorded on a Thermo Electron VG-ESCALAB 220 iXL spectrometer. Films were coated on p^+ silicon wafer. X-ray excitation was performed with a twin anode using its Al Kα line. This excitation mode was preferred to a monochromatic one to minimize the charging effect. So spectra were recorded without any charge compensation by an electron flood gun. Presented data were recorded in a constant energy analyzer mode with pass energy of 20 eV. The photoelectrons were detected perpendicularly to the surface. The samples were stable under long time experiments. Spectrometer calibration was performed using the manufacturer procedure and was completed by a self-consistent check, on sputtered copper, silver, and gold samples, based on the ASTM E902-94 recommendation. Binding energy values of Au $4f_{7/2}$ and Cu $2p_{3/2}$ were 84 and 932.65 eV, respectively. The atomic % compositions are obtained using the peak areas of the levels corrected by the respective sensitivity factors. A global correction of the binding energy (BE) positions was performed assuming a pure Cu(I) contribution and shifting Cu $2p_{3/2}$ lines to 933 eV, the value reported for the $[Cu_4Cl_4(PPh_3)_4]$ cluster.[24]

Single crystals suitable for X-ray structure determination were obtained for **C2** as described in the synthesis section. Crystals were mounted on fiberglass using paraton oil and immediately cooled to 150 K in a cold stream of nitrogen. All data were collected on a Nonius Kappa CCD diffractometer at 150(1) K using Mo Kα (λ = 0.71073 Å) X-ray source and a graphite monochromator. The cell parameters were initially determined using more than 50 reflections. Experimental details are described in Table S1 (Supporting Information). The crystal structures were solved in SIR 97[25] and refined in SHELXL-97[26] by full-matrix least-squares using anisotropic thermal displacement parameters for all non-carbon and non-hydrogen atoms. All the hydrogen atoms were placed in geometrically calculated positions.

Results and Discussion

Synthesis and Structural Characterization of Clusters and Films. $[Cu_4I_4L_4]$ clusters coordinated by pyridine or amine-based ligands have been extensively studied compared to other ligands. However, the synthesis of sol−gel silica films requires the use of an aqueous solution of HCl as catalyst, and pyridine and amine-based complexes are known to be unstable in acidic conditions. Therefore, iodide clusters are functionalized with phosphine derivatives, which are known to be more stable.

The functional cluster (**C1**) is synthesized with the $[Cu_4I_4]$ moiety coordinated by a diphenyl-phosphine ligand bearing a trialcoxysilane group formulated $PPh_2(CH_2)_2Si(OCH_2CH_3)_3$ (**1**) and represented in Figure 2. Ligands bearing alcoxysilane groups are used to copolymerize with silica precursors of the matrix during the sol−gel reactions. This leads to a covalent grafting of clusters to the silica network and to high concentration and homogeneous distribution of clusters within the matrix (see XPS measurements). Cluster **C1** is prepared as colorless oil. The ^{1}H NMR spectrum shows that a small portion of alcoxysilane groups are hydrolyzed, probably explaining negative attempts of crystallization for this cluster.

Compounds based on transition metals with d^{10} electronic configuration are known to present a variety of structural forms. Although the most commonly observed structure for 1:1:1 Cu:X:L stoichiometry is the tetranuclear motif $[Cu_4X_4L_4]$, it is important to verify the molecular structure of **C1** to correctly analyze the optical properties of the corresponding materials. Thus, to ascertain the cubane molecular structure of cluster **C1**, a "reference" cluster was synthesized. This reference cluster **C2** was obtained by using the ligand $PPh_2(CH_2)_2CH_3$ (ligand **2** in Figure 2) which differs from **1** by the absence of alcoxysilane group. As for **C1** and in the same conditions, the reaction of **2** with CuI leads to the corresponding clusters $[Cu_4I_4(\mathbf{2})_4]$ (**C2**). **C2** was crystallized, and its structure was solved by single crystal X-ray diffraction analysis at 150 K. The molecular structure of **C2** is depicted in Figure 3.

As expected, **C2** presents the cubane structure formed by four copper atoms and four iodine atoms which occupy alternatively the corners of a distorted cube. More precisely, the $[Cu_4I_4]$ core consists in a copper tetrahedron embedded within a somewhat larger iodine tetrahedron. The phosphine ligands (**2**) are bonded to each copper atom by the phosphorus atom. **C2** is thus formulated $[Cu_4I_4(PPh_2(CH_2)_2CH_3)_4]$ in agreement with NMR and elemental analysis. The values

(24) Battistoni, C.; Mattogno, G.; Paparazzo, E. *Inorg. Chim. Acta* **1985**, *102*, 1.

(25) Altomare, A.; Burla, M. C.; Camalli, M.; Cascarano, G.; Giacovazzo, C.; Guagliardi, A.; Moliterni, A. G. G.; Polidori, G.; Spagna, R. *J. Appl. Crystallogr.* **1999**, *32*, 115.

(26) Sheldrick, G. M. *SHELXL-97*; Universität Göttingen: Göttingen, Germany, 1997.

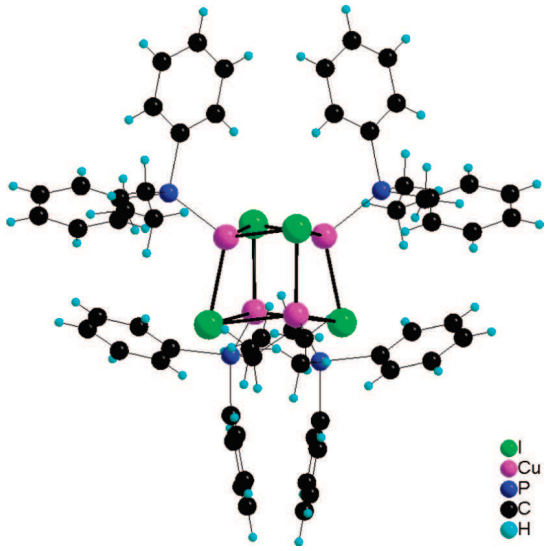

Figure 3. Molecular structure of **C2** $[Cu_4I_4(PPh_2(CH_2)_2CH_3)_4]$.

for the Cu−I (2.668 and 2.701 Å) and Cu−P (2.254 Å) distances are within the range of reported values for this type of cluster with phosphine ligands such as PPh_3[27] and PPh_2CH_3.[28] In **C2**, the Cu−Cu bonds lengths are 3.079 and 3.265 Å. These values are slightly longer compared to those found in similar clusters $[Cu_4I_4(PPh_3)_4]$ (average 2.968 Å, range 2.839−3.165 Å at 295 K) and $[Cu_4I_4(PPh_2CH_3)_4]$ (average 2.930 Å, range 2.840−3.010 Å at 295 K). The Cu−Cu bonds in $[Cu_4I_4L_4]$ clusters based on pyridine or amine ligands are significantly shorter compared to phosphine derivatives.[29] For example, in $[Cu_4I_4py_4]$ Cu−Cu bond distances are in the range 2.619−2.721 Å (average 2.690 Å),[30] that is, shorter than the sum of the van der Waals radii of copper(I) (2.80 Å),[31] implying high metal−metal bonding interactions.

By comparing the different analyses of clusters **C1** and **C2** (NMR, luminescence vide infra), it can be assumed that the structure of **C1** has a cubane form as expected for the stoichiometry employed. Moreover, as already mentioned, poor literature data are available concerning the optical properties of $[Cu_4X_4L_4]$ clusters with L = phosphine ligands. The **C2** cluster obtained as a colorless solid has helped the characterization of the luminescent properties of **C1** and the corresponding sol−gel films.

C1 was incorporated within a sol−gel silica matrix by using MTEOS (methyltriethoxysilane) as silica precursor. The copolymerization was performed by classical sol−gel process in acidic conditions. The gel obtained was spin-coated on substrates leading to transparent and colorless films (**C1** film).

To know whether all the clusters are conserved after the sol−gel process, we have performed NMR and X-ray photoelectron spectroscopy (XPS) experiments. ^{31}P liquid NMR spectra of the sol before spin coating show a singlet centered at −24.9 ppm and a less intense one at +36.8 ppm (Figure S3, Supporting Information). The major peak at −24.9 ppm corresponds to the phosphorus atom coordinated to copper atoms of the cluster. The second peak at +36.8 ppm corresponds to oxidized phosphorus, so to the ligand $OPPh_2(CH_2)_2Si(OC_2H_5)_3$. On the basis of several experiments, the proportion of the two species $[CuI(PPh_2(CH_2)_2Si(OC_2H_5)_3)]$:$OPPh_2(CH_2)_2Si(OC_2H_5)_3$ deduced from the peak area values is around 10:1. The reactions were also performed under inert atmosphere (nitrogen), but the proportion of oxidized ligands did not decrease. The oxidation of the ligand can be explained by the use of HCl to generate the acidic conditions required to the catalysis of the sol−gel reactions. Similar observations have been previously reported when this ligand is bound to silicon.[32]

XPS measurements were performed on the **C2** cluster and **C1** films, and the corresponding data are reported in Table 1. Survey spectra detect only the expected atomic elements: Cu, I, P, O, Si, and C, supporting a very clean and reproducible coating procedure. As expected, a 1:1:1 Cu:I:P stoichiometry is observed for the cluster **C2**. In contrast with NMR results, the **C1** film appears as slightly substoichiometric in phosphorus (vide infra). Measurements on several samples gave similar atomic Si/Cu ratios confirming homogeneous distribution of clusters in the silica matrix. This Si/Cu ratio is low compared to the starting composition (15 instead of 170). This is probably due to the filtration of the sol before deposition, which eliminates some silica aggregates. As clearly suggested by the direct binding energy (BE) data (Table 1), the spectra are slightly shifted toward positive BE, indicating a slight charging effect. This charging effect is evidenced through the asymmetric shape of the XPS peaks as shown for the Cu 2p ones in Figure 4. In accordance with XPS report concerning the $[Cu_4Cl_4(PPh_3)_4]$ cluster giving Cu $2p_{3/2}$ binding energy at 933 eV,[24] a global BE correction has been performed (see Table 1 and Experimental Section).

The I 3d signals present only one contribution in agreement with only one chemical environment. They are similar in shape and position for **C2** cluster and **C1** film (Figures S5-6, Supporting Information). If we consider the correction of the charging effect describe in Table 1, the BE positions become very close for **C2** and **C1** samples (619.72 and 619.63 eV, respectively) consistent with I(-I) species.[33] The P 2p signals are also similar for **C2** cluster and **C1** film (Figures S5-6, Supporting Information). After correction, their BEs have very specific positions around 131.3−131.5 eV. These typical values are consistent with one phosphorus species corresponding to the phosphine ligand coordinated to copper atoms. Our values are in perfect agreement with the XPS data reported for the $[Cu_4Cl_4(PPh_3)_4]$ cluster (131.5 eV).[24] Phosphorus oxide observed by NMR was not detected by XPS analysis (a phosphorus oxide must appear at 133 eV without the charging effect). This shows a problem on the phosphorus measurement which is probably related to the substoichiometry found and could be due to a change of

(27) Dyason, J. C.; Healy, P. C.; Engelhardt, L. M.; Pakawatchai, C.; Patrick, V. A.; Raston, C. L.; White, A. H. *J. Chem. Soc., Dalton Trans.* **1985**, 831.
(28) Churchill, M. R.; Rotella, F. J. *Inorg. Chem.* **1977**, *16*, 3267.
(29) Vega, A.; Saillard, J.-Y. *Inorg. Chem.* **2004**, *43*, 4012.
(30) Raston, C. L.; White, A. H. *J. Chem. Soc., Dalton Trans.* **1976**, 2153.
(31) Bondi, A. *J. Phys. Chem.* **1964**, *68*, 441.
(32) Komoroski, R. A.; Magistro, A. J.; Nicholas, P. P. *Inorg. Chem.* **1986**, *25*, 3917.
(33) *X-ray Photoelectron Spectroscopy Database 20*, Version 3.0; National Institute of Standards and Technology: Gaithersburg, MD (http://srdata.nist.gov/XPS).

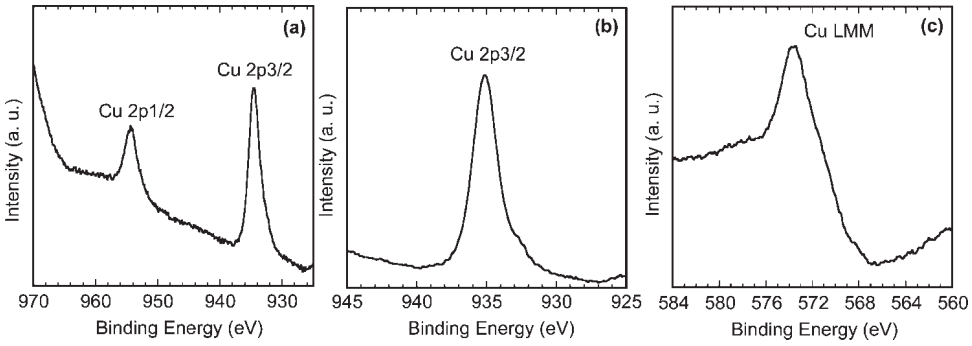

Figure 4. XPS spectra not corrected for charging effect of Cu 2p lines of (a) **C2** and (b) **C1** film and (c) Auger Cu_{LMM} spectra of **C1** film.

Table 1. XPS Data for C2 **and the** C1 **Film**

	C2					**C1** film				
	BE values (eV)	BE Cu $2p_{3/2}$ corrected	correction	BE Values corrected (eV)	atomic %	BE values (eV)	BE Cu $2p_{3/2}$ corrected	correction	BE Values corrected (eV)	atomic %
Cu $2p_{3/2}$	934.52	933	1.52	933	2.20	935.12	933	2.12	933	1.76
I $3d_{5/2}$	621.24			619.72	2.56	621.75			619.63	1.78
P 2p	133.05			131.53	2.82	133.47			131.35	1.36
Si 2p	−					105.2			103.08	25.71
O 1s	532.14			530.62	30.76	534.9			532.78	27.23
C 1s	286.06			284.54	61.66	287.04			284.92	42.17

the film surface during the analysis or its transfer toward an UHV chamber. The Si 2p BE value of 103 eV for **C1** film is typical of SiO_2 sol−gel configuration with Si(IV) species. For the C 1s signal, the maximum BE values are slightly below 285 eV in agreement with the dominant phenyl contribution. The important result concerns the Cu $2p_{3/2}$ lines observed for the **C1** film with the total lack of shakeup satellite peaks characteristic of Cu(II) paramagnetic compounds (Figure 4), so the Cu(II) environment can be totally excluded. Even if the lack of Cu(0) is evident for synthesis consideration, the Cu(I) presence is totally confirmed by the Auger Cu_{LMM} line that is typical of a pure Cu(I) response, as expected for the studied clusters (Figure 4c). Note that a shoulder is observable in the Cu $2p_{3/2}$ line. This can be attributed to another Cu(I) specie. As the iodine signal is similar to the one observed for **C2** and because no Cu(II) species are present, we can suggest that the other Cu(I) species are structurally close to the cubane form $[Cu_4I_4L_4]$. A possible explanation is the distortion of the cubane form in the matrix. The cubane is four coordinated by phosphine bearing alcoxysilane groups. If all these groups are connected to the sol−gel silica matrix in the four directions, this generates constraints on the cluster and slightly changes the coordination environment of the copper. This phenomenon could explain the shoulder observed but needs to be confirmed by further investigations.

Optical Properties. At room temperature, clusters **C1** and **C2** emit intense yellow-green light under UV irradiation. Solid-state emission and excitation spectra of powder of **C2** are shown in Figure 5. At 295 K, the maximum of the emission band is observed at 570 nm (λ_{ex} = 300 nm). The external quantum yield of **C2** at room temperature is determined by using the standard luminophore Zn_2SiO_4:Mn as reference (Supporting Information). The quantum yield of **C2** is 64% under excitation at 260 nm. By lowering the temperature, a new emission band appears at higher energy, and at 87 K the two emission bands are clearly observed with maxima at 425 and 572 nm. The excitation profiles are similar for the two emission bands.

Only qualitative luminescence study of **C1** cluster was done due to the difficulty of handling viscous oil. At room temperature, under UV excitation (λ_{ex} = 300 nm), **C1** exhibits a yellow luminescence centered at 585 nm. The thermochromic luminescence of **C1** is verified by a qualitative test. When the sample is immerged into liquid nitrogen, the luminescence becomes purple by irradiation at 312 nm. From previous studies on $[Cu_4I_4L_4]$ (L = pyridine or amine derivatives) clusters, this thermochromism property appears to be specific to the cubane form. Thus, this luminescence behavior observed both for **C1** and for **C2** clusters also confirms their tetranuclear molecular structure. Moreover, the thermochromic luminescence property observed for **C1** and **C2** seems to be comparable to the one reported for $[Cu_4I_4L_4]$ (L = pyridine or amine derivatives) clusters. In a first approximation, the similarity of the emission bands of **C2** suggests the same band assignment. The LE band at 572 nm could be assigned to a combination of an iodide-to-copper charge transfer transition (XMCT) and of a copper-centered d → s, p transition. The HE band at 425 nm could be attributed to iodide-to-phosphine ligand charge-transfer transition (XLCT). The presence of this band is in accordance

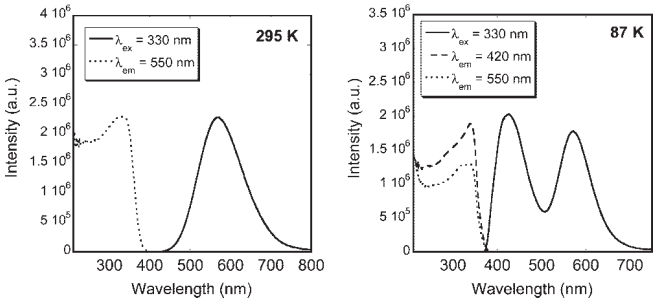

Figure 5. Solid-state excitation (dotted and dashed lines) and emission (solid lines) spectra at 295 and 87 K of **C2** powder.

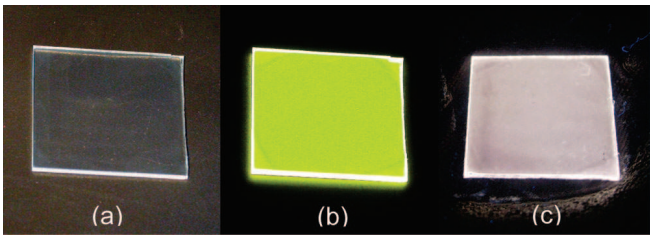

Figure 6. Photographs of **C1** film deposited on glass substrates (1.5 × 1.5 cm^2) (a) under ambient light and (b) under UV irradiation at 312 nm (UV lamp) at room temperature and (c) under UV irradiation at 312 nm (UV lamp) in liquid nitrogen.

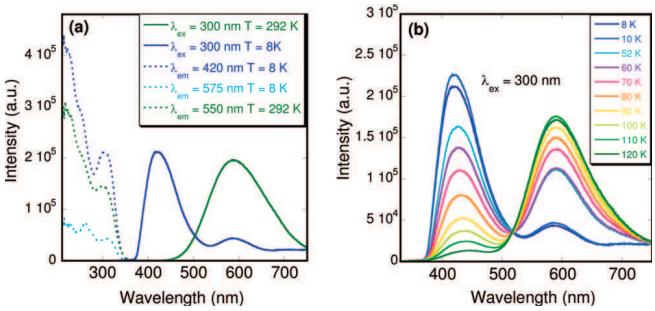

Figure 7. Temperature dependence of luminescence spectra for **C1** film on glass substrate (a) emission (solid lines) at 292 and 8 K with corresponding excitation spectra (dotted lines) and (b) emission spectra from 120 to 8 K with $\lambda_{ex} = 300$ nm.

with the unsaturated character of the $P(C_6H_5)_2C_3H_7$ (**2**) and $P(C_6H_5)_2Si(OC_2H_5)_3$ (**1**) involved ligands.

Figure 6 shows the strong yellow emission of the hybrid colorless silica films obtained (**C1** film), under irradiation at 312 nm at room temperature. The internal quantum yield (Q) of **C1** film under excitation at 280 nm was evaluated to 31% by using a film of YVO_4:Eu nanoparticles[34] as a reference (Supporting Information). This value is quite high and interesting for applications as light emitting devices, but it is worth noting that the wave-guiding effect of the light emission for the samples is not considered. As previously shown for **C1** clusters, thermochromic luminescence of films is revealed by immersion in liquid nitrogen. Under the same UV excitation, the yellow emission disappears and becomes purple (Figure 6c). It is clear that the observation of similar optical properties for clusters embedded in the sol−gel matrix also proves that a large part of them conserves their integrity in silica films.

The luminescence spectra of the films are recorded between 292 and 8 K and are shown in Figure 7. At 292 K, the emission spectrum of the **C1** film displays a single emission band centered at $\lambda_{max} = 589$ nm. The emission wavelength is thus similar to the one observed for **C1** before its introduction in the sol−gel matrix ($\lambda_{max} = 585$ nm) and is slightly shifted (19 nm) compared to **C2** ($\lambda_{max} = 570$ nm). This band could be assigned to the LE band previously mentioned. As expected, at about 120 K, a new emission band appeared at 425 nm. By lowering the temperature down to 10 K, this band progressively increases in intensity with the concomitant extinction of the band at 589 nm. At 70 K, intensities of the two bands are similar and the addition of blue and yellow light gives the purple emission observed for the film in liquid nitrogen (Figure 6c). This band could be assigned to the HE band discussed above attributed to a halide-to-ligand charge transfer emission (XLCT). Note that this band appears at a similar wavelength compared to the one observed for cluster **C2** ($\lambda_{max} = 425$ nm) which has similar ligands. Moreover, the excitation spectra recorded for the LE emission at 292 K and for the HE emission at 8 K are quite similar with a maximum at $\lambda_{max} = 310$ nm (Figure 7a). When the sample is progressively warmed up to room temperature the yellow emission of the LE band is recovered, indicating a completely reversible thermochromism.

An important point is that in the 10−120 K range, all the emission curves present an isobestic point at 520 nm. This is characteristic of equilibrium of two thermally induced processes, which are in our case the light emission from the two LE and HE excited states. After integration of peaks, an Arrhenius plot leads to activation energy of 1760 J (150 cm^{-1}), corresponding to the difference between the energies of the two emission states in thermal equilibrium (Figure S4 in Supporting Information). In a comparable study, a higher value of 1000 cm^{-1} has been reported for the $[Cu_4Br_4(dpmp)_4]$ (dpmp = 2-diphenylmethylpyridine) cluster.[35] This indicates a very high coupling of the two emissions states in our films.

Photophysical studies of the $[Cu_4I_4L_4]$ (L = pyridine or amine derivatives) clusters demonstrate marked environment sensitivity of the LE band with temperature but also with the rigidity of the medium.[15] This rigidochromism behavior has been attributed to molecular distortions of the clusters.[36,37] More recently, the position of the LE band has been reported to be directly related to the Cu−Cu distances in the cluster core $[Cu_4I_4]$.[38] According to theoretical works, the Cu−Cu bonds in the excited state (LUMO) are of bonding character. As the temperature decreases, the Cu−Cu distances become shorter, the bonding character increases, the energy level is lowered, and thus the LE emission band shifts to longer wavelength (from 580 nm at 298 K to 619 nm at 77 K for the $[Cu_4I_4py_4]$ cluster). In contrast, as observed for **C2**, no displacement of the LE emission band of **C1** film occurs by lowering the temperature from 295 to 8 K. This suggests no rigidochromism effect for sol−gel films and implies that Cu−Cu interactions are not involved in the LE emission band, which could be assigned to a pure XMCT transition without participation of copper transitions. In fact, the presence of the LE emission in our clusters and films could appear surprising because it has been previously suggested that only complexes with Cu−Cu distances less than twice the Van der Waals radius of Cu(I) (1.4 Å) show the LE emission.[15] This is clearly not the case for **C2** with Cu−Cu bond length average of 3.15 Å. However, ab initio calculations at the Hartree−Fock level have clearly demonstrate a relationship between the Cu−Cu distances in the cubane type clusters and the energies and distortions (from the ground

(34) Huignard, A.; Gacoin, T.; Boilot, J.-P. *Chem. Mater.* **2000**, *12*, 1090.
(35) Ryu, C. K.; Vitale, M.; Ford, P. C. *Inorg. Chem.* **1993**, *32*, 869.
(36) Vogler, A.; Kunkely, H. *J. Am. Chem. Soc.* **1986**, *108*, 7211.
(37) Tran, D.; Bourassa, J. L.; Ford, P. C. *Inorg. Chem.* **1997**, *36*, 439.
(38) Kim, T. H.; Shin, Y. W.; Jung, J. H.; Kim, J. S.; Kim, J. *Angew. Chem., Int. Ed.* **2008**, *47*, 685.

state) expected for the cluster centered (CC) excited states.[39] The reduced Cu−Cu interaction leads to less distortion in the CC state relative to the ground state. The lesser distortion leads to great communication with the XLCT state. While for the $[Cu_4I_4(py)_4]$ pyridine cluster ($d_{Cu-Cu} = 2.69$ Å) the lowest energy excited state is such a CC state, the lowest excited state in the $[Cu_4I_4(dpmp)_4]$ cluster (dpmp = 2-diphenylmethylpyridine, $d_{Cu-Cu} = 2.90$ Å) is a XLCT state. It seems that our clusters are likely to be a borderline case where the CC state is slightly separated from the XLCT state to be thermally populated from it. This leads to a high coupling between the two emissions at low temperature and a perfectly controlled thermochromic luminescence. Nevertheless, to verify the LE band assignment for **C2** and to elucidate the influence of the Cu−Cu interaction on this band, theoretical works and structure determinations are required for other phosphine-based clusters in relation with their luminescent properties. This will be the subject of further investigations.

Conclusion

Bright luminescent films under UV excitation based on copper-iodide clusters $[Cu_4I_4L_4]$ have been synthesized using the sol−gel process. The incorporation of these new photoactive entities into the silica matrix was performed from their functionalization with phosphine ligands bearing alcoxysilane groups able to copolymerize with the MTEOS sol−gel precursor. By this way, the optical properties of these clusters are successfully preserved in the matrix. NMR and XPS analyses show that a great majority of the clusters remain intact in the film. Only some oxidized phosphine ligands are detected in the film whose presence is inherent to the acidic sol−gel conditions. The use of other sol−gel matrixes involving different catalysis conditions could prevent this ligand oxidation.

To our knowledge, the clusters studied here are the first example of $[Cu_4I_4L_4]$ clusters with L as phosphine ligand, which displays the thermochromic luminescence behavior. As a result of weak Cu−Cu interactions, the emissive states of $[Cu_4I_4L_4]$ clusters with phosphine ligands appear as highly coupled with a low energy barrier (2 kJ·mol^{-1}). This leads to thermochromism in a large temperature range and contrasts with the prototypical $[Cu_4I_4py_4]$ cluster for which the two excited states are weakly coupled with a higher energy barrier (about 10 kJ·mol^{-1}).[15] Photophysical studies of these phosphine-based clusters and especially correlation between structural and optical data should be investigated in the near future.

The luminescence properties of the sol−gel films display striking change in the color emission in temperature due to the cluster integrity. These films are the first exhibiting thermochromic luminescence, and they could be useful as sensors for numerous applications. They have the advantage of the relatively low cost and easy synthesis of the Cu(I) compounds. More generally, it appears that luminescent transition metal clusters constitute an interesting family of phosphors to investigate opening the way to original emissive materials.

Acknowledgment. The authors thank the CNRS for financial support and for the postdoctoral fellowship of C.T.

Supporting Information Available: The X-ray crystallographic file (CIF) and other characterization data (PDF). This material is available free of charge via the Internet at http://pubs.acs.org.

CM801780G

(39) Vitale, M.; Ryu, C. K.; Palke, W. E.; Ford, P. C. *Inorg. Chem.* **1994**, *33*, 561.

VIP Concerted Proton–Electron Transfer

DOI: 10.1002/anie.200907192

Inserting a Hydrogen-Bond Relay between Proton Exchanging Sites in Proton-Coupled Electron Transfers**

Cyrille Costentin, Marc Robert, Jean-Michel Savéant, and Cédric Tard*

Long-distance electron[1] and proton transfer (or transport)[2] are key processes in a considerable number of natural systems. When electron- and proton-transfer processes are coupled and involve different sites (proton-coupled electron transfer (PCET) reactions),[3] the occurrence of concerted proton–electron transfer (CPET) reactions usually require the presence of a hydrogen bond between the proton borne by the group being oxidized and the proton acceptor (and vice versa for a reduction process), as is appears to be the case in emblematic systems such as photosystem II[4] and ribonucleotide reductase.[5] The distances over which the proton may travel as the result of a CPET reaction are limited to values that usually induce the formation of a hydrogen bond in the starting molecule.

Herein we explore the idea according to which this distance might be substantially increased by inserting a hydrogen-bond relay between the group being oxidized and the distant proton acceptor as represented in Scheme 1.[6a,b] The relay is a group bearing a hydrogen atom, able to accept a hydrogen bond from the moiety being oxidized and, at the same time, able to form a hydrogen bond with the proton accepting group without going through a protonated state in the course of the reaction.

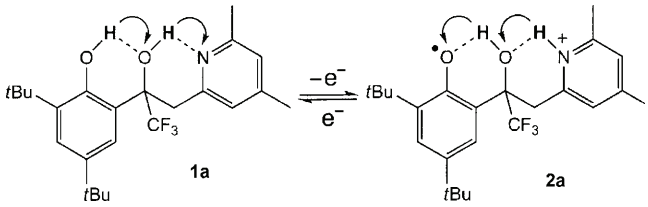

Scheme 1.

Although other moieties could play a similar function, we have selected an OH group for this purpose—having in mind the role sometimes invoked of water molecules in PCET reactions.[7] The molecule in Scheme 1 does not retain the properties of chains of water molecules engaged in a Grotthuss-type transport of a proton,[8] however the OH group possesses the basic property of water molecules in that it is both a hydrogen-bond acceptor and donor.

To test the occurrence of the reaction depicted in Scheme 1 we chose to use the electrochemical approach for the PCET reactions[3b,9] rather than the homogeneous approach. The main reason for this choice of nondestructive electrochemical techniques, such as cyclic voltammetry measurements,[10] is the quick investigation of a continuous range of driving forces that leads to the determination of a standard rate constant (rate constant at zero driving force). The main features of the typical cyclic voltammogram shown in Figure 1a are a one-electron stoichiometry (determined from the peak height) and chemical reversibility, thus indicating that the cation radical **2a** resulting from oxidation is stable on the cyclic voltammetric time scale. Species **2a** is actually stable for longer periods of time as revealed by preparative-scale electrolysis[6c] at 1.34 V vs. NHE. These results confirmed the one-electron stoichiometry and the formation of the expected radical cation **2a**, which is characterized by a typical UV/Vis spectrum for a phenoxyl radical species[11] (λ: 389, 407, 645 nm; ε: 1507, 1549, 164 $L\,cm^{-1}\,mol^{-1}$). The infrared spectrum of **2a** shows the depletion of a band at 1631 cm^{-1} corresponding to a C=C vibration of the pyridine moiety (the second pyridine C=C band is hidden by the supporting electrolyte). The same evolution was observed upon protonation of 2,4,6-trimethyl pyridine (band at 1633 cm^{-1}), thus confirming that the pyridine moiety is protonated upon generation of the phenoxyl radical species.

The reversibility and one-electron stoichiometry of the cyclic voltammetric response shown in Figure 1a contrasts with the irreversibility and two-electron stoichiometry observed when neither the pyridine acceptor, nor the OH relay are present as with 2,4,6-tri-*tert*-butyl phenol (**1c**; Figure 1c). For **1c**,[12] the cation radical that was initially generated rapidly and irreversibly deprotonates, and the resulting phenoxyl radical is oxidized more easily than the starting phenol according to an ECE mechanism,[10] thus resulting in a two-electron stoichiometry. The same behavior is also observed in the presence of the OH relay and in the absence of the pyridine moiety (Figure 1d; the synthesis of **1d** is described in the Supporting Information). It also follows that the reversible oxidation of **1a** does not proceed through the intermediacy of the cation radical bearing a positive charge on the central OH group.

[*] Prof. Dr. C. Costentin, Prof. Dr. M. Robert, Prof. Dr. J.-M. Savéant, Dr. C. Tard
Laboratoire d'Electrochimie Moléculaire, Unité Mixte de Recherche Université – CNRS No 7591, Université Paris Diderot, Bâtiment Lavoisier
15 rue Jean de Baïf, 75205 Paris Cedex 13 (France)
E-mail: saveant@univ-paris-diderot.fr

[**] Financial support from the Agence Nationale de la Recherche (Programme blanc PROTOCOLE) is gratefully acknowledged.

Supporting information for this article is available on the WWW under http://dx.doi.org/10.1002/anie.200907192.

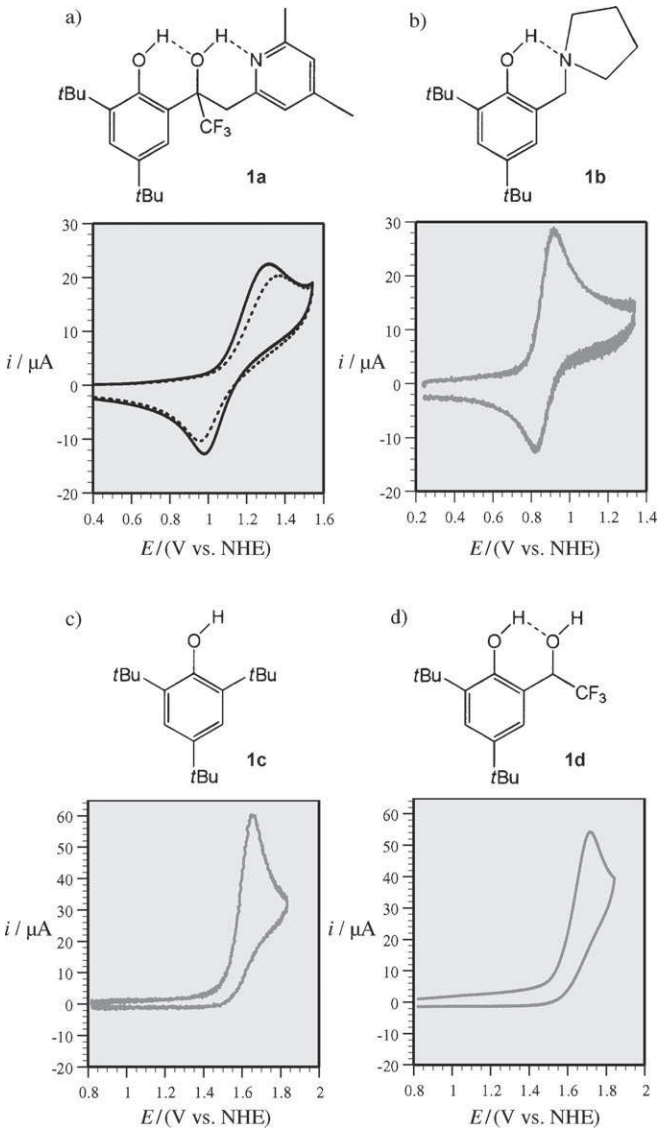

Figure 1. Cyclic voltammetry measurements in acetonitrile + 0.1 M nBu_4NBF_4 for 1 mM of compound at a glassy carbon electrode and at a scan rate of 0.2 Vs^{-1}. In the scan of **1a**, the solid and dashed traces were recorded in the presence of 1% CH_3OH or CD_3OD, respectively.

The cyclic voltammetric response of **1a** (Figure 1a) resembles more that of the aminophenol **1b** (Figure 1b) in terms of both electron stoichiometry and chemical reversibility, although the anodic-to-cathodic potential separation is larger in the first case than in the second. As shown earlier,[13,14] with **1b**, the proton generated upon one-electron oxidation of the phenol moiety is transferred to the amine group concertedly with electron transfer thanks to a six-membered ring configuration, which is favorable to the formation of a hydrogen bond between the phenol and amine group in the starting molecule. In the case of **1a**, proof that the alcoholic OH group effectively serves as a hydrogen-bond relay between the phenol and pyridine groups requires that the molecule is not folded so as to put these two groups at a sufficiently short distance from one another to bring about the direct formation of a hydrogen bond between them. The X-ray structure of **1a**[6b] (Figure 2) shows that this is indeed the case—the distance between the phenolic oxygen atom and

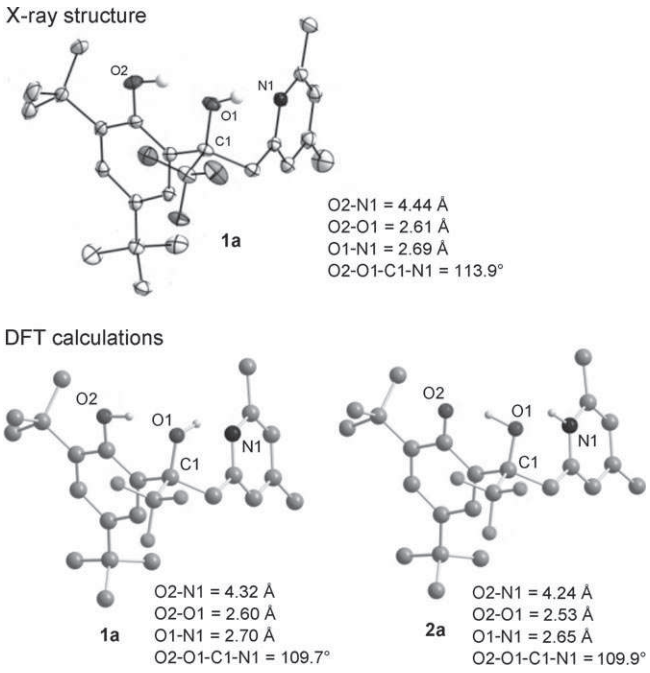

Figure 2. X-ray structure[6] of **1a** and DFT calculations[10] for **1a** and **2a**.

the nitrogen atom of pyridine is indeed 4.44 Å and the O2-O1-C1-N1 dihedral angle is 113.9°. The DFT calculations[6c] led to a very similar result in the case of **1a** (Figure 2) and also showed that substantial folding does not take place in cation radical **2a**.

Another interesting observation is that of the existence of an H/D kinetic isotope effect (KIE) for **1a**—similar to what was observed with **1b** (see Table 1)—thus pointing to the occurrence of a concerted pathway indicating that the equilibrium shown in Scheme 1 is not merely the expression of a global process but should be viewed as an elementary CPET step. This conclusion also falls in line with the implausibility of a mechanism that would proceed through oxidation of the zwitterionic form (**1az**) of **1a**, owing to the small equilibrium ratio $[\mathbf{1az}]/[\mathbf{1a}] \approx 10^{-9}$.[15] Also, the fact that the reaction does not proceed via an intermediate in which the central OH group is protonated is in agreement with the pK_a values of phenol ($pK_a = 27$)[15a] and protonated alcohol ($pK_a < 2$)[15d] in acetonitrile.

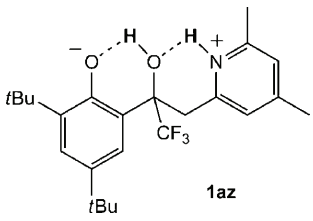

In the framework of the CPET mechanism, we derive the standard rate constant of the reaction (k_S) from the peak separation in Figure 1a, after linearization of the Marcus–Hush–Levich activation-driving force law, thus leading to the Butler–Volmer rate law[6c,13b] with a transfer coefficient equal to 0.5 [Eq. (1)]; where i: current, S: electrode surface area, []: concentrations at the electrode surface, E: electrode potential, E^0: CPET standard potential. The standard rate constant of the reaction (k_S), that is, the rate constant at zero driving force, is a measure of the intrinsic characteristics of the reaction.

$$\frac{i}{FS} = k_S \exp\left[\frac{F}{2RT}(E-E^0)\right]\left\{[\mathbf{1}] - \exp\left[\frac{-F}{RT}(E-E^0)\right][\mathbf{2}]\right\} \quad (1)$$

It is immediately clear that with **1a**, a scan rate of only 0.2 $V\,s^{-1}$ is sufficient for the peak separation to be controlled by the CPET kinetics (Figure 1a). Whereas at this scan rate, the oxidation of **1b** is still controlled by diffusion (Figure 1b). For **1b**, one has to operate at a scan rate of 5 $V\,s^{-1}$ to reach the CPET kinetic control to achieve good peak separation.[13] Table 1 summarizes the values of k_S obtained by using, as the diffusion coefficient the value derived from the peak heights ($10^{-5}\,cm^2\,s^{-1}$), together with the values of the standard potential. Comparison between the values of k_S in the presence of 1% of CH_3OH or CD_3OD allowed the determination of the H/D kinetic isotope effects reported in Table 1 (upon introduction of 1% of CD_3OD, the NMR proton signals for phenol and alcohol disappeared therefore indicating complete deuteration).

Table 1: Characteristics of the CPET oxidation of **1a** and **1b**.

Compound	E^0 [V NHE^{-1}]	$k_{S,H}$ [cm s^{-1}]	KIE	λ [eV]	λ_0 [eV]	λ_i [eV]
1a	1.10	5×10^{-4}	2.4	1.36	0.78	0.58
1b[13]	0.85	8×10^{-3}	1.7	1.06	0.78	0.28

With such a small KIE and assuming that electron transfer is adiabatic,[13b] the preexponential factor (Z) in the expression of the standard rate constant (as illustrated experimentally by the temperature dependent kinetics of the oxidation of **1b**[13b]) [Eq. (2)][10,13c] can be approximated by the collision

$$k_S = Z\sqrt{\frac{RT}{4\pi\lambda}}\int_{-\infty}^{\infty}\frac{\exp\left[-\frac{RT}{4\lambda}\left(\frac{\lambda}{RT}-\varsigma\right)^2\right]}{1+\exp(\varsigma)}d\varsigma \quad (2)$$

frequency, $Z = \sqrt{RT/2\pi M}$ (M: molar mass, $M = 423\,g\,mol^{-1}$), thus leading to a numerical estimation of the experimental reorganization energy, $\lambda = 1.36$ eV for **1a**, to be compared with $\lambda = 1.06$ eV for **1b**. The solvent reorganization energy (λ_0) has been estimated to be 0.78 eV for **1b**, and is likely to be the same for **1a**. It follows that the internal reorganization energy varies from 0.28 to 0.58 eV from **1b** to **1a**. With a more rigid structure, in which the movements of the heavy atoms would be minimized, the standard rate constant for **1a** should therefore be marginally slower than for **1b**.

We may thus conclude that the introduction of a hydrogen bonding group between the electron and proton exchanging sites may offer an efficient route for proton movement over distances as large as 4.3 Å, by means of the translocation of two protons in a concerted manner with electron transfer. This Grotthuss-type proton transfer is as efficient as the travel a proton accomplishes over distances of the order of 2.5 Å in systems where hydrogen bonding between the phenol moiety and the proton acceptor benefits from the formation of a six-membered ring. The key feature of this efficient proton movement is a "hydrogen-bond swing" as the one shown in Scheme 1, which avoids going through a high-energy intermediate in which the relay would be protonated. The ability of the trifluoro-substituted alcohol group to serve as an efficient relay is presumably the result of a good balance between its hydrogen-bond-accepting and -donating capabilities.

Work is in progress to further investigate the mechanism of the hydrogen-bond relay and to uncover the parameters that constitute a good relay.

Received: December 21, 2009
Published online: April 20, 2010

Keywords: electrochemistry · electron transfer · hydrogen bonds · phenols · proton transfer

[1] a) H. B. Gray, J. R. Winkler, *Q. Rev. Biophys.* **2003**, *36*, 341–372; b) C. C. Page, C. C. Moser, P. L. Dutton, *Curr. Opin. Chem. Biol.* **2003**, *7*, 551–556.
[2] C. A. Wraight, *Biochim. Biophys. Acta Bioenerg.* **2006**, *1757*, 886–912.
[3] a) S. Y. Reece, D. G. Nocera, *Annu. Rev. Biochem.* **2009**, *78*, 673–699; b) C. Costentin, *Chem. Rev.* **2008**, *108*, 2145–2179.
[4] A. W. Rutherford, A. Boussac, *Science* **2004**, *303*, 1782–1784.
[5] J. Stubbe, D. G. Nocera, C. S. Yee, M. C. Y. Chang, *Chem. Rev.* **2003**, *103*, 2167–2202.
[6] a) The synthesis of **1a** is described in the Supporting Information; b) CCDC 746981 (**1a**) contains the supplementary crystallographic data for this paper. These data can be obtained free of charge from The Cambridge Crystallographic Data Centre via www.ccdc.cam.ac.uk/data_request/cif; c) see Supporting Information.
[7] M. Wang, J. Gao, P. Müller, B. Giese, *Angew. Chem.* **2009**, *121*, 4296–4298; *Angew. Chem. Int. Ed.* **2009**, *48*, 4232–4234.
[8] a) J. T. Hynes, *Nature* **2007**, *446*, 270–273; b) D. Marx, *ChemPhysChem* **2006**, *7*, 1848–1870.
[9] a) S. Wang, P. S. Singh, D. H. Evans, *J. Phys. Chem. C* **2009**, *113*, 16686–16693; b) C. Costentin, C. Louault, M. Robert, J.-M. Savéant, *Proc. Natl. Acad. Sci. USA* **2009**, *106*, 18143–18148.
[10] J.-M. Savéant, *Elements of Molecular and Biomolecular Electrochemistry*, Wiley-Interscience, New York, **2006**.
[11] a) E. R. Altwicker, *Chem. Rev.* **1967**, *67*, 475–531; b) T. Maki, Y. Araki, Y. Ishida, O. Onomura, Y. Matsumura, *J. Am. Chem. Soc.* **2001**, *123*, 3371–3372.
[12] J. A. Richards, P. E. Whitson, D. H. Evans, *J. Electroanal. Chem.* **1975**, *63*, 311–327.
[13] a) C. Costentin, M. Robert, J.-M. Savéant, *J. Am. Chem. Soc.* **2006**, *128*, 4552–4553; b) C. Costentin, M. Robert, J. M. Savéant, *J. Am. Chem. Soc.* **2007**, *129*, 9953–9963.

[14] a) homogenous oxidation of similar aminophenols has also been reported, see reference [14c]; b) I. J. Rhile, J. M. Mayer, *J. Am. Chem. Soc.* **2004**, *126*, 12718 – 12719; c) I. J. Rhile, T. F. Markle, H. Nagao, A. G. DiPasquale, O. P. Lam, M. A. Lockwood, K. Rotter, J. M. Mayer, *J. Am. Chem. Soc.* **2006**, *128*, 6075 – 6088.

[15] a) $\frac{[\mathbf{1az}]}{[\mathbf{1a}]} \approx 10^{-\left(\frac{pK_{PhOH} - pK_{2,4,6-timethylpyridine} + pK_{2,4-dimethylpyridine}}{2}\right)} \approx 10^{-9}$, approximated by extrapolation and interpolation from the pK_a values of pyridine and phenol in acetonitrile (12.3 and 27, respectively)[15b] and in water (5.2 and 10, respectively),[15c] and the pK_a values for 2,4,6-trimethylpyridine and 2,4-dimethylpyridine in water (7.43 and 6.99, respectively).[15c] The pK_a value used for the pyridine in **1a** was the average value for 2,4,6-trimethylpyridine and 2,4-dimethylpyridine.[15b] b) K. Izutzu in *Acid-Base Dissociation Constants in Dipolar Aprotic Solvents*, Blackwell, Boston, **1990**, pp. 17 – 35; c) *Handbook of Chemistry and Physics*, *82nd ed.* (Ed.: D. R. Lide), CRC, Boca Raton, **2001–2002**, pp. **8**-48 – **8**-56; d) I. M. Kolthoff, M. K. Chantooni, *J. Am. Chem. Soc.* **1968**, *90*, 3320 – 3326.

[16] Other approaches are possible, see for example: S. Hammes-Schiffer, A. V. Soudackov, *J. Phys. Chem. B* **2008**, *112*, 14108 – 14123.

ACS Catalysis

Research Article

pubs.acs.org/acscatalysis

Bioinspired Iron Sulfide Nanoparticles for Cheap and Long-Lived Electrocatalytic Molecular Hydrogen Evolution in Neutral Water

Carlo Di Giovanni,[†] Wei-An Wang,[‡] Sophie Nowak,[‡] Jean-Marc Grenèche,[§] Hélène Lecoq,[‡] Ludovic Mouton,[‡] Marion Giraud,*[,‡] and Cédric Tard*[,†]

[†]Laboratoire d'Électrochimie Moléculaire, UMR 7591 CNRS, Université Paris Diderot, Sorbonne Paris Cité, 15 rue Jean-Antoine de Baïf, F-75205 Paris Cedex 13, France

[‡]Laboratoire ITODYS, UMR 7086 CNRS, Université Paris Diderot, Sorbonne Paris Cité, 15 rue Jean-Antoine de Baïf, F-75205 Paris Cedex 13, France

[§]Institut des Molécules et Matériaux du Mans, IMMM, UMR 6283 CNRS, Université du Maine, Avenue Olivier Messiaen, F-72085 Le Mans Cedex 9, France

Supporting Information

ABSTRACT: Alternative materials to platinum-based catalysts are required to produce molecular hydrogen from water at low overpotentials. Transition-metal chalcogenide catalysts have attracted significant interest over the past few years because of their activity toward proton reduction and their relative abundance compared with platinum. We report the synthesis and characterization of a new type of iron sulfide (FeS, pyrrhotite) nanoparticles prepared via a solvothermal route. This material can achieve electrocatalysis for molecular hydrogen evolution with no structural decomposition or activity decrease for at least 6 days at a mild overpotential in neutral water at room temperature.

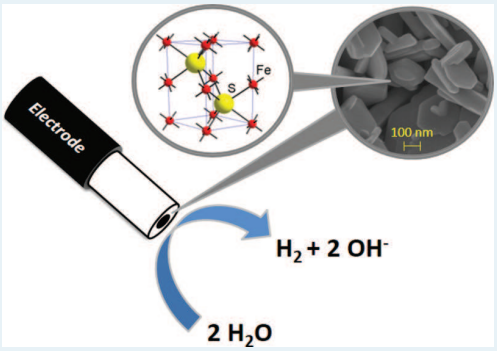

KEYWORDS: *hydrogen evolution reaction, iron sulfide nanoparticles, electrocatalysis, nanoparticle Mössbauer spectroscopy, electrode modification*

1. INTRODUCTION

Environmental and economic factors require a drastic change in energy production. Replacing fossil fuels by renewable and sustainable energy sources is an absolute necessity in order to face contemporary energy challenges. Molecular hydrogen is currently at the forefront for the prospect of new energy vectors as a way to store energy in chemical bonds. Its clean, cold combustion in fuel cells[1] or its production in water electrolyzers will require the replacement of noble-metal catalysts such as platinum and its alloys by earth-abundant catalysts for proton reduction into dihydrogen if worldwide use of hydrogen is considered.

Inspiration can be found in microorganisms and algae, where hydrogenase metalloenzymes are capable of reversibly converting protons into molecular hydrogen.[2] The active sites of these enzymes are made of Fe/S or Fe/Ni/S core clusters, and molecular hydrogen can be evolved at turnover frequencies as high as 9000 moles of H_2 per mole of hydrogenase per second in water at pH 7 and 30 °C.[3] Attempts to implement these enzymes onto electrodes have been made, but major practical drawbacks of these natural systems arise from their high oxygen sensitivity, their bulkiness (which limits the number of catalysts per unit of surface area), and the difficulty of producing high amounts of material for industrial purposes.[4] Despite numerous examples and attractive properties, such as their oxygen stability and solubility in different media, hydrogenase biomimetic synthetic molecular electrocatalysts, in solution or grafted onto an electrode, present poor to moderate activity toward molecular hydrogen evolution or uptake reactions.[5,6] Interestingly, it has been demonstrated that cubane-type Fe_4S_4 clusters can reduce protons into dihydrogen from weak organic acids,[7] but the poor stability of such molecules toward water and dioxygen is still problematic when considering these systems as potential efficient catalysts. It is worth noting that these molecular Fe_4S_4 clusters can be stabilized within porous chalcogenide frameworks and that such systems show activity for homogeneous electrocatalysis and photocatalysis for dihydrogen evolution and carbon dioxide reduction.[8−10]

Non-precious-metal catalysts operating at low overpotentials and high current densities under mild conditions (ca. pH 7, 1 atm, room temperature) that would compete with natural enzymes or platinum itself are scarce. Recently, long-lived and cheap coordination complexes that can homogenously reduce protons to molecular hydrogen in neutral aqueous media have

Received: December 9, 2013
Revised: January 14, 2014

   dx.doi.org/10.1021/cs4011698 | ACS Catal. 2014, 4, 681−687

been prepared[11] using molybdenum,[12] cobalt,[13−15] or nickel[16,17] as metal centers. Furthermore, molybdenum sulfide electrocatalysts, in the form of nanocrystals,[18] amorphous electropolymerized films,[19,20] molecular complexes,[21] or amorphous particles,[22] or transition-metal alloys of nickel−molybdenum,[23,24] cobalt sulfide,[25] and iron[26] or nickel[27] phosphides have also been reported for their high activity toward molecular hydrogen evolution in acidic or neutral water at relatively low overpotentials and represent a very promising way to replace noble-metal catalysts. Therefore, we can think that stabilization of other types of transition-metal chalcogenide moieties within nanosystem assemblies could allow the preparation of cheap and sustainable bioinspired catalysts.

Given the ubiquity of iron sulfide minerals in nature, such as pyrite FeS_2, which is the most abundant mineral on the Earth's surface,[28] we decided to study the electrocatalytic properties of iron sulfide nanoparticles that can be synthesized easily and rapidly on a gram scale from an abundant and cheap precursor. Herein we report the preparation of air-stable pyrrhotite-type FeS nanoparticles dispersed in Nafion films, which exhibit molecular hydrogen evolution in neutral water at room temperature with catalytic stability exceeding 6 days of electrolysis.

2. RESULTS AND DISCUSSION

2.1. Synthesis and Characterization of Nanoparticles. The synthesis of pyrrhotite FeS nanoparticles was performed using a single precursor source, $Fe_2S_2(CO)_6$,[29,30] which decomposes in octylamine under solvothermal conditions at 230 °C. This simple and rapid method allows us to prepare nanoparticles in >80% yield. The chemical composition of the prepared powder was evaluated by energy-dispersive X-ray (EDX) measurements, which indicated that the powder mainly contained Fe and S atoms and corresponded to a 1:1 Fe/S stoichiometry (Figure S3 and Table S1 in the Supporting Information). The organic content of the powder, estimated via thermogravimetric analysis (TGA) measurements under air, was found to be negligible.

As displayed in Figure 1, the X-ray diffraction (XRD) pattern, which can be fully indexed in a pure pyrrhotite phase ($P6_3/mmc$ space group), reveals that the particles are crystalline. Refinement of the lattice parameters led to the values a = 3.450 Å and c = 5.770 Å, in good agreement with the values obtained for another synthetic pyrrhotite, $Fe_{1-0.125x}S$ ($0 \le x \le 1$), which has the NiAs structure.[31] They are rather close to those of $Fe_{0.921}S$ (ICSD 98-016-8077) in that study,[31] but since atomic positions and occupancies were not refined (only strain was refined through the "arbitrary texture" option of the MAUD software), one cannot conclude at this stage that this sample is exactly the same and possesses this refined stoichiometry. The mean crystallite size was estimated to be about 100 nm, but the refinement showed that the crystallites are anisotropic (Figure S6 and Table S2 in the Supporting Information).

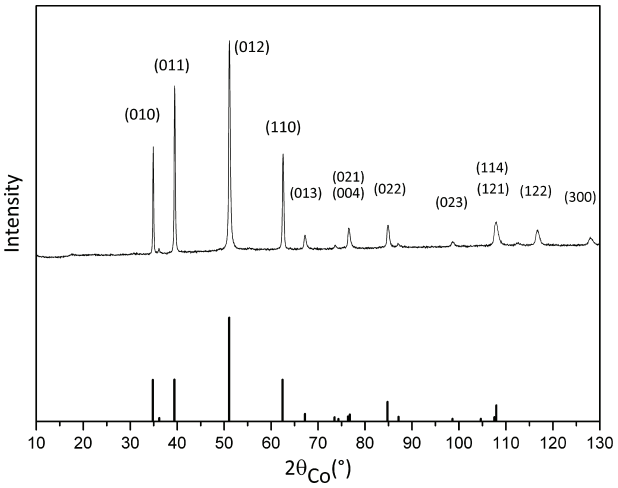

Figure 1. XRD pattern of FeS nanoparticles. The vertical bars represent the theoretical pattern for pyrrhotite $Fe_{0.921}S$ (ICSD 98-016-8077).[31]

The transmission electron microscopy (TEM) image (Figure 2 left) provides a 2D representation of the nanoparticles. The black powder recovered by centrifugation consists of hexagonally shaped nanoparticles that are polydispersed with sizes ranging from 50 to 500 nm. The size range values are close to the average coherent diffraction domain obtained by XRD (using the Debye−Scherrer law), suggesting that the particles are mostly single crystals. The selective-area electron diffraction (SAED) pattern on a single particle (Figure 3) shows a monocrystalline-particle diffraction pattern with sixfold symmetry, which is expected for a crystalline hexagonal array observed along the ⟨001⟩ zone axis. The scanning electron microscopy (SEM) image (Figure 2 right) reveals that the particles have a faceted platelet morphology with aspect ratios as low as 1/10 and confirms both the size range and the polydispersity of the sample observed by TEM. It also supports the very low content of organic matter in the sample.

In order to improve the structural characterization of our sample, we decided to use ^{57}Fe Mössbauer spectrometry, which is a sensitive tool for probing the local chemical environment, to bring information complementary to that of XRD. Indeed, the Mössbauer spectra recorded at both 300 and 77 K clearly exhibit a magnetic hyperfine structure with broadened lines (Figure 4).

The modeling procedure involved a discrete series of magnetic sextets with isomer shift values ranging from 0.68 to 0.78 mm/s and from 0.78 to 0.88 mm/s and hyperfine field values ranging from 23 to 31 T and from 25 to 35 T at 300 and 77 K, respectively, with rather low values of the quadrupole shift. As it was established above by X-ray diffraction that the sample is well-crystalline, the broadened lines should result from local chemical disorder in the environment of the Fe nuclei and a lack of stoichiometry. The mean values listed in Table 1 can be compared with those in the literature;[32] the present results allow us a priori to conclude that the Fe species belong to $Fe_{1-x}S$ sulfides, close to a S-deficient disordered pyrrhotite.

2.2. Electrochemical Studies and Stability of the Coated Electrode. Catalyst ink was prepared using a Nafion dispersion and FeS nanoparticles to evaluate the catalytic activity toward molecular hydrogen evolution. Vitreous carbon rotating disk electrodes (RDEs) were coated with FeS nanoparticles dispersed in Nafion and aged for 12 h at 100 °C in an oven. Analysis of a coated electrode film by SEM showed a rather dense and uniform film with a thickness estimated to be around 40 nm (Figure 5).

Under an argon atmosphere, cyclic voltammetry in 0.1 mol/L potassium phosphate (pH 7.0) exhibited a sharp rise in current from ca. −0.8 vs NHE (Figure 6). Some small bubbles evolved from the surface of the coated electrode, and from gas

dx.doi.org/10.1021/cs4011698 | ACS Catal. 2014, 4, 681−687

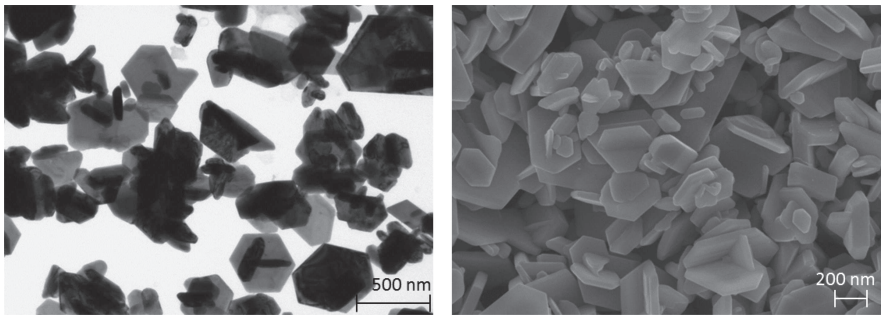

Figure 2. (left) TEM and (right) SEM images of FeS nanoparticles.

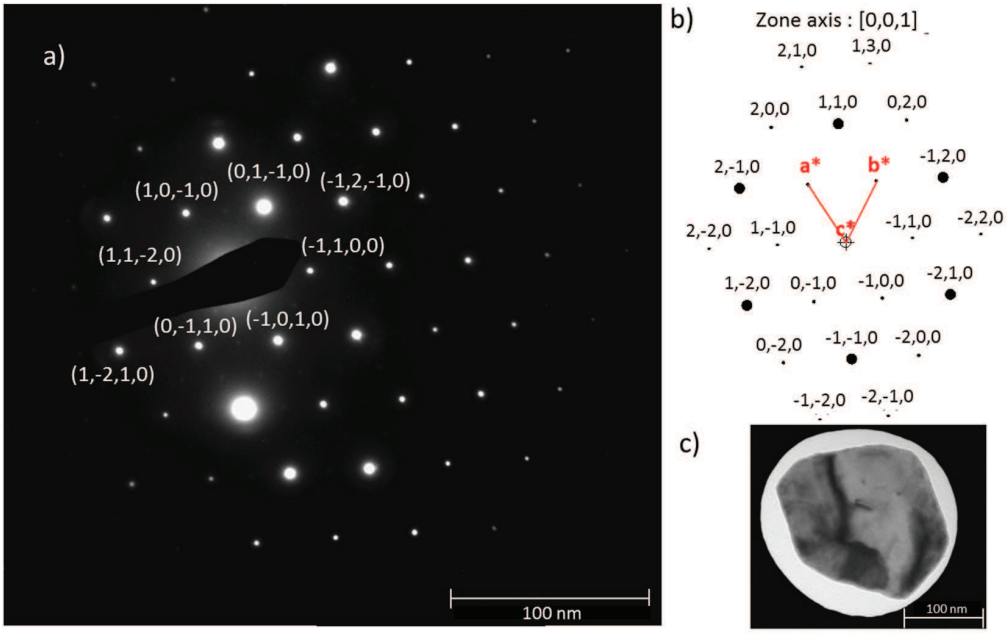

Figure 3. (a) SAED pattern along the ⟨001⟩ axis on the single particle shown in (c). (b) Theoretical pattern along this axis obtained with the Carine software.

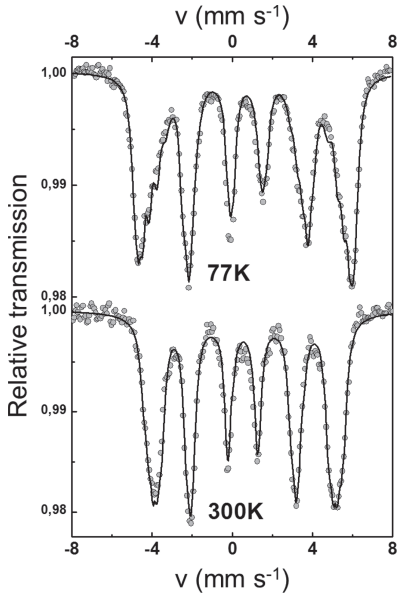

Figure 4. Mössbauer spectra recorded at 300 and 77 K.

Table 1. Mean Values of the Hyperfine Parameters Characteristic of the Prepared $Fe_{1-x}S$ Nanoparticles and Other Iron Sulfide Materials from the Literature

formula	T (K)	δ (mm/s)[a]	2ε (mm/s)[a]	B_{hf} (T)[b]	ref
$Fe_{1-x}S$	300	0.74	0.08	23.5	this work
FeS	300	0.7−0.9	−0.3	30−32	32
$Fe_{11}S_{12}$	300	0.55	0.05	22.0−23.5	32
$Fe_{10}S_{11}$	300	0.55	0.05	25.5−26.5	32
Fe_9S_{10}	300	0.55	0.10	27.5−31.5	32
Fe_7S_8	300	0.77	0.08	22.9	32
		0.79	0.03	26.7	
		0.79	0.15	31.1	
		0.81	−0.09	34.5	
$Fe_{1-x}S$	77	0.84	−0.02	30.7	this work

[a]Uncertainty = ±0.02 mm/s. [b]Uncertainty = ±0.5 T.

chromatography analysis we determined that this current enhancement was due to molecular hydrogen evolution. On the reverse scan we observed two oxidation peaks at −0.50 and −0.42 vs NHE, probably due to oxidation of hydride or dihydrogen species trapped at the surface of the catalytic film, but no further characterizations were performed. The coated

dx.doi.org/10.1021/cs4011698 | ACS Catal. 2014, 4, 681−687

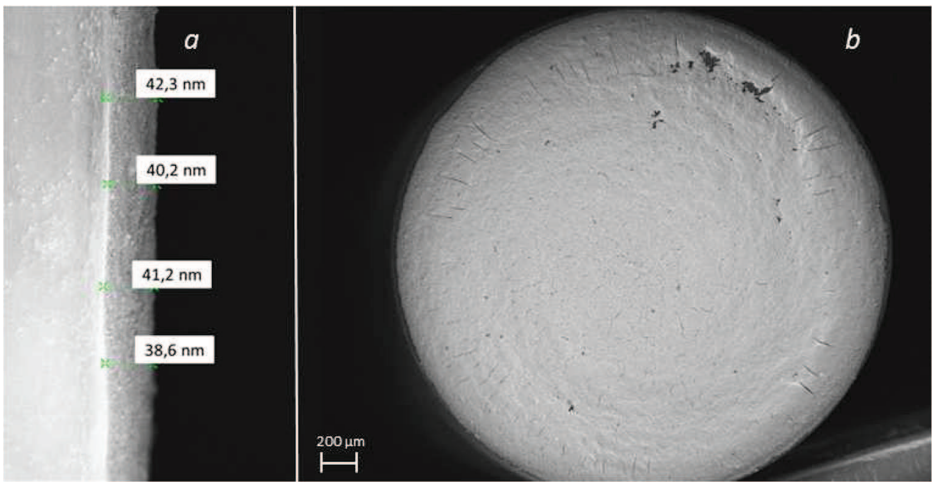

Figure 5. SEM images of an FeS nanoparticle/Nafion-coated rotating disk electrode: (a) side view; (b) top view.

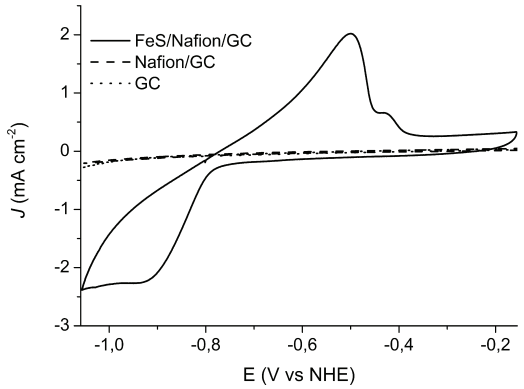

Figure 6. Cyclic voltammograms of FeS nanoparticles dispersed in Nafion on a rotating disk electrode (solid line), a Nafion-coated electrode (dashed line), and a bare electrode (dotted line). Voltammograms were recorded in 0.1 mol/L potassium phosphate buffer at pH 7.0 and 20 °C (scan rate 0.1 V/s; rotation rate 4000 rpm; scan number 10).

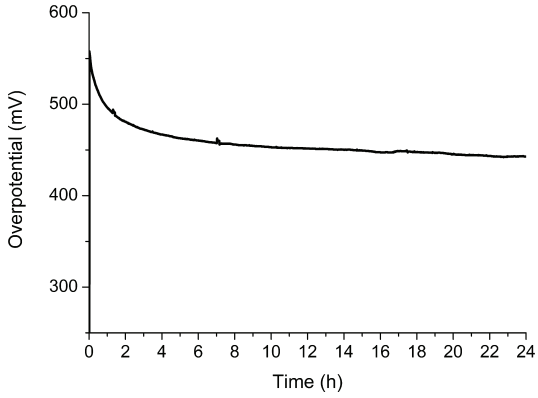

Figure 7. Galvanostatic control experiment on an electrode functionalized with FeS nanoparticles dispersed in Nafion (overpotential = | applied potential + 0.059 × pH| vs NHE). The experiment was performed on a rotating disk electrode in 0.1 mol/L potassium phosphate buffer at pH 7.0 and 20 °C (I = 50 μA; rotation rate 4000 rpm). No quantifiable pH variation during the experiment was observed.

electrodes were found to be stable for electrochemical studies for more than 6 months with no particular storage care.

The stability of the modified electrode was investigated over 24 h by a galvanostatic experiment at a current density of J = 0.7 mA cm^{-2} (I = 50 μA) at pH 7.0 (Figure 7). The decrease in overpotential observed during the first 24 h indicates a rise in the activity of the film toward H_2 generation, likely due to some modifications of the surface state of the catalyst. The overpotential then decreases slightly over the course of the experiment. The small spikes detected on the curve are due to the formation of small H_2 bubbles at the surface of the coated electrode.

To determine the dependence of the catalytic activity and film stability on pH, small amounts of concentrated HCl or NaOH were added under an argon atmosphere to a 0.1 mol/L buffered solution at pH 7.0 in order to vary the pH from 6.0 to 8.0. Higher catalytic activity (in terms of current density) was noted at lower pH. On the contrary, under basic conditions a strong decrease in the current was observed. It is worth mentioning that the pH changes did not produce irreversible alterations of the film, as the initial current density was fully recovered by restoring the initial pH 7.0 conditions (Figure 8).

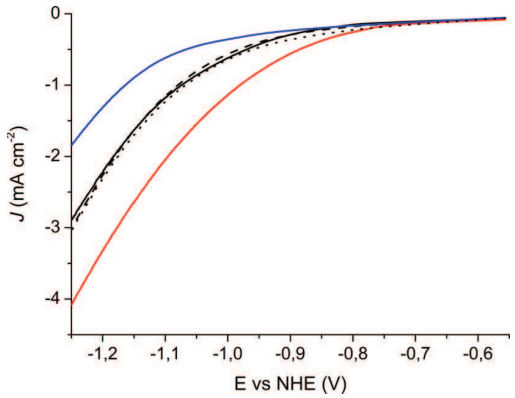

Figure 8. Linear sweep voltammetry of FeS nanoparticles dispersed in Nafion. Voltammograms were recorded on a rotating disk electrode in 0.1 mol/L potassium phosphate buffer at pH 6.0, 7.0, and 8.0 at 20 °C (scan rate 0.01 V/s; rotation rate 4000 rpm). Initial pH 7.0 conditions (solid black line); pH 6.0 (red line); pH 7.0 restored conditions from pH 6.0 (dashed line); pH 8.0 (blue line); pH 7.0 restored conditions from pH 8.0 (dotted line).

dx.doi.org/10.1021/cs4011698 | ACS Catal. 2014, 4, 681−687

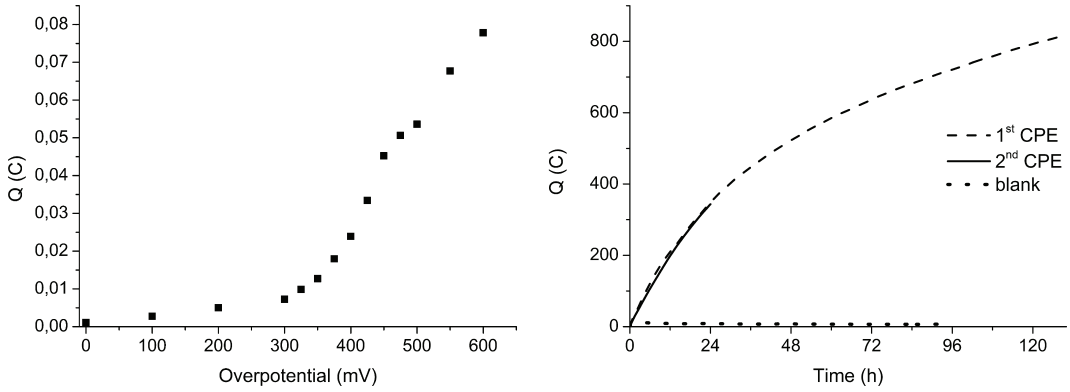

Figure 9. (left) Controlled-potential electrolysis of FeS nanoparticles in 0.1 mol/L potassium phosphate buffer at pH 7.0. (right) First (dashed line) and second (solid line) bulk electrolyses at an overpotential of 350 mV (−0.763 V vs NHE) in 1 mol/L potassium phosphate buffer at pH 7.0, showing a buildup of charge (Q) vs time [$Q = f(t)$] for the cell with and without (dotted line) FeS nanoparticles.

2.3. Controlled-Potential Electrolysis. Long-duration controlled-potential electrolysis (CPE) was performed to assess the durability and robustness of the FeS nanoparticle-coated electrode. Figure 9 (left) shows the amount of charge measured at different overpotentials (η = |applied potential + 0.059 × pH| vs NHE) at pH 7.0 after subtraction of the contribution from the blank solution. Low current densities were observed at low overpotentials, and a sharp increase arises from 325 mV. To estimate the Faradaic efficiency for the H_2 production, CPE was performed in a 1 mol/L phosphate buffer solution at pH 7.0 over 5 days at η = 350 mV (−0.763 V vs NHE) (Figure 9 right, dashed line). Quantitative (≥0.99) Faradaic yield for molecular hydrogen evolution was confirmed by gas chromatography analysis as well as by volumetric measurements (Figure S8 in the Supporting Information). The slight decrease in the slope of the Q versus time curve is due to the pH increase of 0.3 unit caused by proton consumption. To further investigate this point, the crucible coated with the FeS nanoparticles was refilled with a fresh solution of 1 mol/L phosphate buffer at pH 7.0, and an identical Q versus time profile was obtained over a 1 day CPE under the same experimental conditions (Figure 9 right, solid line). Again, an almost quantitative Faradaic yield (≥0.98) was obtained for H_2 generation, outlining the remarkable stability of such nanoparticles over the course of catalysis. No particular care in storage of the catalyst or pre-degassing of the phosphate buffer solution was required, demonstrating the long-term stability of this material. After these 6 days of electrolysis, no major structural changes in the electrolyzed catalyst were observed by XRD (Figures S5–S7 in the Supporting Information), and the morphology of the FeS nanoparticles was also found to be unchanged (Figure S2 in the Supporting Information).

Comparison of different solid-state catalysts is a challenging task because of differences in the electrode preparation (coating vs electrodeposition) and the amount of material loaded onto the electrode. A rough comparison can be envisaged by measuring polarization curves and extracting the current density at an overpotential of 0 V (J_0) and the slope of this curve.[25] A measure of the catalytic activity of FeS nanoparticles was extrapolated from polarization curves in neutral water and compared with those of related solid-state catalysts for hydrogen evolution (Figure 10 and Table 2). A linear increase in log J was found in the overpotential range from 350 to 450 mV. At a given current density of J = 0.18 mA cm^{-2} (log J = −3.75), the overpotential of our material is shifted positively

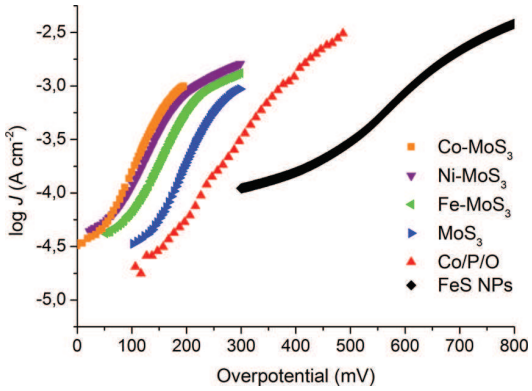

Figure 10. Tafel plots of electrodeposited catalysts (from literature data) and FeS nanoparticles (from this work) in water at pH 7.0. The Co/P/O curve (red) was recorded in a 0.5 mol/L phosphate buffer at 5 mV/s.[33] The curves for MoS_3 (blue), Fe−MoS_3 (green), Ni−MoS_3 (purple), and Co−MoS_3 (orange) were recorded in a phosphate buffer (unknown concentration) at 1 mV/s.[19] The curve for FeS nanoparticles (black) was recorded in a 0.1 mol/L phosphate buffer at 1 mV/s.

Table 2. Exchange Current Densities (J_0) of Different Electrocatalysts in Water at pH 7.0[a]

material	J_0 (mA cm^{-2})	slope (mV/dec)	η range (mV)	ref
Co−MoS_3	1.1 × 10^{-2}	87	87–122	19
Ni−MoS_3	1.0 × 10^{-2}	96	110–144	19
Fe−MoS_3	4.8 × 10^{-3}	95	137–176	19
Co/P/O	1.9 × 10^{-3}	134	200–300	33
MoS_3	8.9 × 10^{-4}	86	171–203	19
FeS	6.6 × 10^{-4}	150	350–450	this work

[a] Data were extracted from the polarization curves in Figure 10.

by about 300 mV relative to Co−MoS_3, the best in the molybdenum sulfide series reported by Hu and co-workers,[19] and by about 100 mV relative to the cobalt phosphate material reported by Artero and co-workers.[33]

3. SUMMARY AND CONCLUSIONS

We have demonstrated that a robust and efficient catalyst for molecular hydrogen evolution from neutral water that operates at a mild overpotential can be made from excessively cheap

dx.doi.org/10.1021/cs4011698 | ACS Catal. 2014, 4, 681–687

Earth-abundant materials and exhibits a catalytic activity exceeding 5 days.

Despite the fact that our FeS nanoparticles compare less favorably with cobalt phosphate or molybdenum sulfide materials at a given overpotential, the remarkable stability and the ease of preparation clearly show that the iron sulfide materials are very promising. If we now compare the abundance and cheapness of the different materials, the iron sulfide nanoparticles are clearly favored over cobalt phosphate or molybdenum sulfide materials. A rough comparison between the different metal prices shows that in 2012, iron ore ($101/ton) was much cheaper than nickel ($22,890/ton), molybdenum ($34,100/ton) or cobalt ($36,100/ton), with the platinum-group metals being much more expensive ($25,000,000/ton).[34] We can therefore envisage that iron sulfide nanoparticles may offer a great advantage in term of cost and availability compared with other transition-metal electrocatalysts for molecular hydrogen evolution, and further investigations on related materials are currently in progress.

4. EXPERIMENTAL SECTION

Methods and Materials. All of the chemicals were of analytical grade and were used without further purification. Octylamine and Nafion (0.05 thick membrane, perfluorosulfonic acid−PTFE copolymer, 5% w/w solution) were purchased from Alfa Aesar. Tetraethylammonium acetate and potassium phosphate were purchased from Sigma-Aldrich. The $Fe_2S_2(CO)_6$ precursor was synthesized according to previously published procedures.[29,30]

Instrumentation. XRD patterns were determined on a PANalytical X'Pert PRO diffractometer equipped with a multichannel X'Celerator detector using Co Kα radiation (λ = 1.7902) in the 2θ range 10−130°. The data were collected at room temperature with a step size of 0.033° and a time by step equal to 100 s. The refinement of the phase was determined using the MAUD software based on the Rietveld method combined with Fourier analysis,[35] which is well-adapted for nano-objects. The size of the coherent diffraction domains (crystallite size) was determined with both MAUD software and Highscore Plus software from PANalytical. Gas chromatography analyses for dihydrogen detection were performed on a Hewlett-Packard 6890 series GC system with a thermal conductivity detector fitted with a 2 m long Agilent Technology 1/8″ Carbosieve S3 60−80 mesh column and calibrated with pure H_2 gas.

Synthesis and Characterization of Nanoparticles. The synthesis of the particles was adapted from a published procedure.[36] In a typical synthesis, $Fe_2S_2(CO)_6$ (143 mg, 0.42 mmol) was dissolved in 35 mL of octylamine in a stainless steel autoclave equipped with a Teflon container at room temperature. The dark-red solution was placed in an oven at 230 °C and kept at this temperature overnight (ca. 16 h). The black precipitate obtained was centrifuged at 22 500 rpm in polypropylene copolymer tubes and washed five times with absolute ethanol, each washing being followed by centrifugation at 22 500 rpm. The collected black powder (62 mg, 0.70 mmol as FeS only, 84% yield), was dried under vacuum for 1 h at room temperature and then characterized as it was by XRD, EDX, TEM, SEM, and Mössbauer spectroscopy.

Microscopy. The particle size and morphology were determined by TEM and SEM. For TEM analysis, the powders were dispersed in chloroform, and a drop was placed on a 200 mesh carbon-coated copper grid. Images were recorded using a JEOL JEM-100CXII microscope operating at 100 kV. SEM images were obtained with a Zeiss Supra 40 scanning electron microscope. The images were taken at different magnifications using an In lens detector at a low voltage (5 kV) and in a small working distance (5 mm). An SEM image of a coated electrode was also taken. The atomic composition of the powder was analyzed using an EDX system with a JEOL 6510 scanning electron microscope. The analyses were performed at 15 kV and a work distance of 10 mm. The results were analyzed using the IRIDIUM Ultra software. The semiquantitative analyses (Table S1 in the Supporting Information) were obtained with a FeS_2 pyrite standard.

Mössbauer Spectroscopy. The ^{57}Fe Mössbauer spectra were recorded at 300 and 77 K with a bath cryostat in a transmission geometry using a ^{57}Co/Rh source mounted on a conventional electromagnetic drive with a triangular velocity form. The sample consisted of a thin powdered layer containing 5 mg of Fe/cm^2. The obtained Mössbauer spectra were analyzed by least-squares fitting to Lorentzian functions. The isomer shift values (δ) were referred to that of α-Fe at 300 K.

Electrochemistry. The potentiostat used for cyclic voltammetry was an Autolab PGSTAT 12. The working electrode was a 3 mm diameter glassy carbon (GC) rotating disk electrode (Tokai) that was carefully polished and ultrasonically rinsed in absolute ethanol before use. The counter electrode was a platinum wire, and the reference electrode was an aqueous SCE electrode. All of the potentials were referred to NHE by adding +0.244 V to the potential vs SCE (a conversion to RHE can be done by adding 0.059 × pH to the potential vs NHE). All of the experiments were carried out under argon at 20 °C at different scan rates and a rotation rate of 4000 rpm. From a mixture of pyrrhotite FeS nanoparticles (10 mg), Nafion (33 μL), and isopropanol (100 μL), 2 μL was deposited on the electrode surface, which was then dried in air and left for 12 h at 100 °C in an oven. A 0.1 mol/L phosphate buffer (pH 7.0) was prepared and used as a supporting electrolyte and degassed under argon. Experimental details for Figures 6, 7, 8, and 9 are detailed in the Supporting Information.

■ ASSOCIATED CONTENT

Supporting Information

Details of electrochemical measurements and additional nanoparticle characterizations. This material is available free of charge via the Internet at http://pubs.acs.org.

■ AUTHOR INFORMATION

Corresponding Authors

*E-mail: marion.giraud@univ-paris-diderot.fr.

*E-mail: cedric.tard@univ-paris-diderot.fr. Phone: +33 (0)157 278 783. Fax: +33 (0)157 278 787.

Notes

The authors declare no competing financial interest.

■ ACKNOWLEDGMENTS

The authors thank P. Beaunier, S. Drouet, M. Duca, M. Fournier, J.-Y Piquemal, and L. Sicard for experimental assistance. We also thank V. Ching, J. Peron, J.-Y. Piquemal, and M. Robert for helpful discussions and suggestions.

■ REFERENCES

(1) Bagotsky, V. S. *Fuel Cells: Problems and Solutions*, 2nd ed.; John Wiley & Sons: Hoboken, NJ, 2012.

(2) Armstrong, F. A.; Belsey, N. A.; Cracknell, J. A.; Goldet, G.; Parkin, A.; Reisner, E.; Vincent, K. A.; Wait, A. F. *Chem. Soc. Rev.* **2009**, *38*, 36−51.
(3) Frey, M. *ChemBioChem* **2002**, *3*, 153−160.
(4) Cracknell, J. A.; Vincent, K. A.; Armstrong, F. A. *Chem. Rev.* **2008**, *108*, 2439−2461.
(5) DuBois, D. L.; Bullock, R. M. *Eur. J. Inorg. Chem.* **2011**, 1017−1027.
(6) Tard, C.; Pickett, C. J. *Chem. Rev.* **2009**, *109*, 2245−2274.
(7) Yamamura, T.; Christou, G.; Holm, R. H. *Inorg. Chem.* **1983**, *22*, 939−949.
(8) Yuhas, B. D.; Smeigh, A. L.; Samuel, A. P. S.; Shim, Y.; Bag, S.; Douvalis, A. P.; Wasielewski, M. R.; Kanatzidis, M. G. *J. Am. Chem. Soc.* **2011**, *133*, 7252−7255.
(9) Yuhas, B. D.; Prasittichai, C.; Hupp, J. T.; Kanatzidis, M. G. *J. Am. Chem. Soc.* **2011**, *133*, 15854−15857.
(10) Yuhas, B. D.; Smeigh, A. L.; Douvalis, A. P.; Wasielewski, M. R.; Kanatzidis, M. G. *J. Am. Chem. Soc.* **2012**, *134*, 10353−10356.
(11) Thoi, V. S.; Sun, Y.; Long, J. R.; Chang, C. J. *Chem. Soc. Rev.* **2013**, *42*, 2388−2400.
(12) Karunadasa, H. I.; Chang, C. J.; Long, J. R. *Nature* **2010**, *464*, 1329−1333.
(13) Bigi, J. P.; Hanna, T. E.; Harman, W. H.; Chang, A.; Chang, C. J. *Chem. Commun.* **2010**, *46*, 958−960.
(14) Sun, Y.; Bigi, J. P.; Piro, N. A.; Tang, M. L.; Long, J. R.; Chang, C. J. *J. Am. Chem. Soc.* **2011**, *133*, 9212−9215.
(15) Andreiadis, E. S.; Jacques, P.-A.; Tran, P. D.; Leyris, A.; Chavarot-Kerlidou, M.; Jousselme, B.; Matheron, M.; Pécaut, J.; Palacin, S.; Fontecave, M.; Artero, V. *Nat. Chem.* **2013**, *5*, 48−53.
(16) Helm, M. L.; Stewart, M. P.; Bullock, R. M.; DuBois, M. R.; DuBois, D. L. *Science* **2011**, *333*, 863−866.
(17) Han, Z.; McNamara, W. R.; Eum, M.-S.; Holland, P. L.; Eisenberg, R. *Angew. Chem., Int. Ed.* **2012**, *51*, 1667−1670.
(18) Jaramillo, T. F.; Jørgensen, K. P.; Bonde, J.; Nielsen, J. H.; Horch, S.; Chorkendorff, I. *Science* **2007**, *317*, 100−102.
(19) Merki, D.; Vrubel, H.; Rovelli, L.; Fierro, S.; Hu, X. *Chem. Sci.* **2012**, *3*, 2515−2525.
(20) Merki, D.; Fierro, S.; Vrubel, H.; Hu, X. *Chem. Sci.* **2011**, *2*, 1262−1267.
(21) Karunadasa, H. I.; Montalvo, E.; Sun, Y.; Majda, M.; Long, J. R.; Chang, C. J. *Science* **2012**, *335*, 698−702.
(22) Vrubel, H.; Merki, D.; Hu, X. *Energy Environ. Sci.* **2012**, *5*, 6136−6144.
(23) McKone, J. R.; Sadtler, B. F.; Werlang, C. A.; Lewis, N. S.; Gray, H. B. *ACS Catal.* **2013**, *3*, 166−169.
(24) Chen, W.-F.; Sasaki, K.; Ma, C.; Frenkel, A. I.; Marinkovic, N.; Muckerman, J. T.; Zhu, Y.; Adzic, R. R. *Angew. Chem., Int. Ed.* **2012**, *51*, 6131−6135.
(25) Sun, Y.; Liu, C.; Grauer, D. C.; Yano, J.; Long, J. R.; Yang, P.; Chang, C. J. *J. Am. Chem. Soc.* **2013**, *135*, 17699−17702.
(26) Xu, Y.; Wu, R.; Zhang, J.; Shi, Y.; Zhang, B. *Chem. Commun.* **2013**, *49*, 6656−6658.
(27) Popczun, E. J.; McKone, J. R.; Read, C. G.; Biacchi, A. J.; Wiltrout, A. M.; Lewis, N. S.; Schaak, R. E. *J. Am. Chem. Soc.* **2013**, *135*, 9267−9270.
(28) Rickard, D.; Luther, G. W. *Chem. Rev.* **2007**, *107*, 514−562.
(29) Seyferth, D.; Henderson, R. S.; Song, L. C. *Organometallics* **1982**, *1*, 125−133.
(30) Stanley, J. L.; Rauchfuss, T. B.; Wilson, S. R. *Organometallics* **2007**, *26*, 1907−1911.
(31) Xu, F.; Navrotsky, A. *Am. Mineral.* **2010**, *95*, 717−723.
(32) Vandenberghe, R. E.; De Grave, E. In *Mössbauer Spectroscopy: Tutorial Book*; Yoshida, Y., Langouche, G., Eds.; Springer-Verlag: Berlin, 2013; pp 91−185.
(33) Cobo, S.; Heidkamp, J.; Jacques, P.-A.; Fize, J.; Fourmond, V.; Guetaz, L.; Jousselme, B.; Ivanova, V.; Dau, H.; Palacin, S.; Fontecave, M.; Artero, V. *Nat. Mater.* **2012**, *11*, 802−807.
(34) Kelly, T. D.; Matos, G. R. *Historical Statistics for Mineral and Material Commodities in the United States, 2012*; U.S. Geological Survey Data Series 140; http://minerals.usgs.gov/ds/2005/140/index.html.
(35) Lutterotti, L.; Matthies, S.; Wenk, H. R. *CPD Newsl.* **1999**, *21*, 14−15.
(36) Vanitha, P. V.; O'Brien, P. *J. Am. Chem. Soc.* **2008**, *130*, 17256−17257.